Torque performance improvement on multi three-phase PMSM based on PWM drives for marine application

Xuchen Wang B.Eng. (Hons.)

Thesis submitted to the University of Nottingham for the degree of

Doctor of Philosophy, August 2019

Abstract

Multiphase drive systems have received a growing interest in recent decades for marine propulsion applications, due to their high power density, high reliability and good torque performance. Among the multiphase drives, the multi three-phase drive with independent neutral points is a popular option for this application, as it allows for the usage of standard control and standard power electronics for the individual three-phase systems. In high power systems the switching frequency of the power semiconductor is usually limited, which results in high frequency current ripple caused by the PWM of the DC/AC converter. The ripple affects the performance of the machine in terms of torque.

This thesis presents a novel mathematical modelling of multi three-phase Permanent Magnet Synchronous Machines (PMSMs) fed by voltage source Pulse Width Modulation (PWM) converters. It is found that, based on the analytical models of the multi three-phase drive, the torque ripple introduced by PWM voltage excitation can be reduced by the shift of carrier phase angles among different three-phase inverters. For the torque ripple analyzed in this thesis, only the interaction between the armature field, resulting from the PWM voltage excitation, and the fundamental component of the permanent magnet field is considered. The proposed carrier phase shift angles are obtained for the case studies of a sectored triple three-phase PMSM and two dual three-phase PMSMs. Numerical and finite element analysis (FEA) and experimental results are presented to validate the analytical models of the multi three-phase drives. Additionally, the torque performance improvement and the effect on current ripple introduced by the proposed carrier phase shifts are presented and validated by means of both simulation and experimental results.

Acknowledgements

I would like to extend my sincere gratitude to my supervisors Dr. Giampaolo Buticchi, Dr. He Zhang, Dr. Chunyang Gu, Prof. Patrick Wheeler, Dr. Lie Xu, and Prof. Chris Gerada for their technical support, expert guidance and continuous encouragement, which mainly contribute to the completion the thesis. Moreover, special thanks should go to Dr. Giacomo Sala, who provided me with the valuable academic support and truly inspired me to fall in love with my research work.

I would like to thank my colleagues in the PEMC groups from the University Of Nottingham and Tsinghua University, who helped me out of the difficulties in the past four years. I owe a special debt of gratitude to Dr. Hao Yao for helping me establish the experimental test rig and his patient guidance.

I would like to thank my friends in UNNC and UNUK for their advice, understanding and encouragement to sustain me through the frustration and depression. Furthermore, I would like to express my special appreciation to Mr. Zhen Huang for his help and support in all aspects.

Last my thanks go to my beloved family for always standing by my side, their love, understanding and patience during the past four years. I would like to express my heartfelt gratitude to all around me during the process to pursuit a PhD degree. Without their company, the life in the past four years is by no means such a happy, colorful and rewarding journey.

Contents

Chapter 1 : Introduction 1

1.1 Motivation for the project 1

1.2 Overview 1

1.3 Aims and objectives 4

1.4 Thesis outline and content 5

Chapter 2 : Literature review and background 7

2.1 Electric marine propulsion 7

2.2 Electrical machines for propulsion applications 9

2.2.1 Overview of electric machines 9

2.2.2 Multiphase machines 10

2.3 Voltage source converters 13

2.3.1 The three-phase full bridge converter 13

2.3.2 Multilevel converters for high power applications 14

2.3.3 Parallel converters 17

2.4 Modulation techniques for voltage source converters 19

2.4.1 Space vector modulation 19

2.4.2 Carrier-based pulse width modulation 19

2.4.3 Double flourier integral analysis method of pulse width modulation 21

2.5 The PWM harmonic effect on the machine performance 24

Chapter 3 : Modelling of multi three-phase machines 27

3.1 Inductance analysis of arbitrary phase PMSM 27

3.1.1 Air-gap MMF produced by single coil current 28

3.1.2 Self-inductance of a single coil 29

3.1.3 Mutual inductance between two coils 30

3.1.4 Self-inductance of two single coils 31

3.2 Analytical matrix torque equations of multi three-phase machines 33

3.2.1 Matrix inductance table of multi three-phase machines 33

3.2.2 The relationship between phase currents and phase voltages in multi three-phase machines 34

3.2.3 Analytical matrix torque equations in multi three-phase machines 40

3.3 Analytical torque equations of multi three-phase machines by voltage and current space vectors 42

3.4 The machines in this thesis 45

3.5 Simulation results 47

3.6 Conclusion 56

Chapter 4 : Analysis of PWM related torque ripple reduction method in multi three-phase drives 57

4.1 Modelling of multi three-phase PWM voltage converters 57

4.2 Analytical PWM related torque equations in multi three-phase drives 65

4.3 Selective torque harmonic elimination method on dual three-phase drives....... 70

4.3.1 Dual three-phase drive system 70

4.3.2 Analysis of PWM Related Torque Ripple Reduction Method...................... 72

4.4 Simulation results.. 82

4.4.1 Analytical, numerical and FEA results of the multi three-phase drive 82

4.4.2 Selective torque harmonic elimination method validation by numerical results ………… 94

4.5 Experimental results... 100

4.5.1 Experimental of results of the triple three-phase drive 100

4.5.2 Selective torque harmonic elimination method validation by experimental results 106

4.6 Conclusion... 110

Chapter 5 Analysis of current ripple introduced by PWM related torque ripple reduction method.. 112

5.1 Analysis of current ripple in sectored triple three-phase drive introduced by PWM related torque ripple reduction method 112

5.2 Analysis of current ripple in distributed dual three-phase drives introduced by PWM related torque ripple reduction method 117

5.3 Simulation results.. 122

5.3.1 Simulation results of phase currents in the sectored triple three-phase drive 122
5.3.2 Simulation results of phase currents in the distributed dual three-phase drive 125
5.4 Experimental results 130
5.4.1 Experimental results of phase currents in the sectored triple three-phase drive 130
5.4.2 Experimental results of phase currents in the distributed dual three-phase drive 134
5.5 Conclusion.. 139
Chapter 6 : Conclusions 141
6.1 Conclusion of the work 141
6.2 Future work 141
Reference 143
Appendix A: MATLAB Code of matrix inductance table...I
Appendix B: MATLAB Code of the dual three-phase drive analytical models.................II
Appendix C: MATLAB Code of the triple three-phase drive analytical models VI
Appendix D: PLECS model of the triple three-phase drive X
Appendix E: Winding layout of a 48-slot 8-pole distributed PM machine XI

List of Figures

Figure 1-1: Multi three-phase drive system 2

Figure 2-1: Integrated Power system for marine propulsion [14] 7

Figure 2-2：Three-phase full bridge converter for high-power applications (with series connected switches) [55] 13

Figure 2-3: Topologies of phase voltage source inverters [55] 14

Figure 2-4: a) Multi single-phase drive with parallel converters b) Multi three-phase drive with parallel converters [76] 18

Figure 2-5: (a) The x-y plane for the sine-triangle modulation (b) The x-y plane for the corresponding PWM output voltage [89] 22

Figure 2-6: The vibration signal waveforms and their corresponding FFT spectra a) without the proposed carrier phase shift b) with the proposed carrier phase shift [10] 25

Figure 3-1: Air-gap MMF produced by the current of stator coil AA' 28

Figure 3-2: Stator coil AA' and stator coil BB' 30

Figure 3-3: Air-gap MMF produced by the current of stator coil A_1A_1' and A_2A_2' 31

Figure 3-4: *N* three-phase drive system without phase displacements among different sub three-phase systems 34

Figure 3-5: *N* three-phase drive system without phase displacements among different sub three-phase systems [102] 42

Figure 3-6: 2MW machine model in Maxwell 47

Figure 3-7: 2MW machine of distributed winding construction 49

Figure 3-8: 2MW machine of sectored winding construction 49

Figure 4-1: Phase leg voltage a) time varying phase leg voltage b) the corresponding FFT spectrum of the phase leg voltage waveform 58

Figure 4-2: Effective two-pole *N* three-phase winding construction 62

Figure 4-3: Total voltage space vector FFT spectra without and with applying CPS-PWM under M=0.9 63

Figure 4-4: Total voltage space vector FFT spectra without and with applying CPS-PWM under M=0.5 64

Figure 4-5: Total voltage space vector FFT spectra without and with applying CPS-PWM under M=0.1 64

Figure 4-6: Cross section of the 18 slots – 6 poles 3 sectored PM machine [102] 67

Figure 4-7: FFT spectrum of the normalized torque a) without applying carrier phase shift method b) with applying the proposed carrier phase shift method [102]. 68

Figure 4-8: Bessel functions $Jn(\xi)$ for $n = 0,1,\dots,6$ [84] 69

Figure 4-9: Dual three-phase drive system 71

Figure 4-10： The FFT spectrums of the real part of the total voltage space vectors a) $\alpha = 0$ and $\theta c2 - \theta c1 = 0$ b) $\alpha = 0$ and $\theta c2 - \theta c1 = \pi$ c) $\alpha = \pi 6$ and $\theta c2 - \theta c1 = 0$ d) $\alpha = \pi 6$ and $\theta c2 - \theta c1 = \pi 2$ e) $\alpha = \pi 6$ and $\theta c2 - \theta c1 = -\pi 2$ 81

Figure 4-11: a) & b) Phase voltage waveform a) analytical result b) numerical result c) & d) Phase voltage spectra c) analytical result d) numerical result 84

Figure 4-12: a) & b) Phase current waveform a) analytical result b) numerical result c) & d) Phase current spectra c) analytical result d) numerical result 85

Figure 4-13: a) & b) Electromagnetic torque waveform a) analytical result b) numerical result c) & d) Electromagnetic torque spectra c) analytical result d) numerical result..... 86

Figure 4-14: Sectored triple three-phase PM machine model in Magnet 88

Figure 4-15: Block diagram of simulation model [102] 89

Figure 4-16 a) & b) Analytical and numerical results of phase A1 current waveform a) without CPS-PWM b) with CPS-PWM c) & d) Analytical and numerical results of phase A1 current FFT spectrum c) without CPS-PWM d) with CPS-PWM [102]. 90

Figure 4-17: a) & b) Analytical, numerical and FEA results of torque waveform a) without CPS-PWM b) with CPS-PWM c) & d) Analytical, numerical and FEA results of torque FFT spectrum c) without CPS-PWM d) with CPS-PWM [102]. 92

Figure 4-18: Connection circuits of dual three-phase PM machines 94

Figure 4-19: Block diagram of simulation model/experimental set-up. 95

Figure 4-20: Peak to peak torque ripple reduction with applying the proposed CPS-PWM under different modulation index of winding configurations $\alpha = 0$ and $\alpha = \pi 6$. 97

Figure 4-21: a) & b) Simulation results of torque waveforms of winding configuration $\alpha = 0$ a) without CPS-PWM, $\theta c2 - \theta c1 = 0$ b) with CPS-PWM, $\theta c2 - \theta c1 = \pi$ c) & d) Simulation results of torque FFT spectrums of winding configuration $\alpha = 0$ c) without CPS-PWM, $\theta c2 - \theta c1 = 0$ d) with CPS-PWM, $\theta c2 - \theta c1 = \pi$................................... 98

Figure 4-22: a) & b) & c) Simulation results of torque waveforms of winding configuration $\alpha = \pi 6$ a) without CPS-PWM, $\theta c2 - \theta c1 = 0$ b) with CPS-PWM, $\theta c2 - \theta c1 = \pi 2$ c) with CPS-PWM, $\theta c2 - \theta c1 = -\pi 2$ d) & e) & f) Simulation results of torque FFT spectrums of winding configuration $\alpha = \pi 6$ d) without CPS-PWM, $\theta c2 - \theta c1 = 0$ d) with CPS-PWM, $\theta c2 - \theta c1 = \pi 2$ f) with CPS-PWM, $\theta c2 - \theta c1 = -\pi 2$................... 99

Figure 4-23: Triple three-phase machine drive system experimental set-up [102]. 101

Figure 4-24: Experimental results of equivalent electromagnetic torque waveform with and without CPS-PWM b) FFT spectrum of equivalent electromagnetic torque waveform with and without CPS- PWM [102]. 103

Figure 4-25: Experimental results (With low-pass filter) of equivalent electromagnetic torque waveform with and without CPS-PWM 103

Figure 4-26: Dual three-phase drive systems (α=0 and α=π6) experimental test rig. ... 106

Figure 4-27: a) & b) Experimental results of equivalent electromagnetic torque waveforms of winding configuration $\alpha = 0$ a) without CPS-PWM, $\theta c2 - \theta c1 = 0$ b) with CPS-PWM, $\theta c2 - \theta c1 = \pi$ c) & d) Experimental results of equivalent electromagnetic torque FFT spectrums of winding configuration $\alpha = 0$ c) without CPS-PWM, $\theta c2 - \theta c1 = 0$ d) with CPS-PWM, $\theta c2 - \theta c1 = \pi$. 108

Figure 4-28: a) & b) & c) Experimental results of equivalent electromagnetic torque waveforms of winding configuration $\alpha = \pi 6$ a) without CPS-PWM, $\theta c2 - \theta c1 = 0$ b) with CPS-PWM, $\theta c2 - \theta c1 = \pi 2$ c) with CPS-PWM, $\theta c2 - \theta c1 = -\pi 2$ d) & e) & f) Experimental results of equivalent electromagnetic torque FFT spectrums of winding configuration $\alpha = \pi 6$ d) without CPS-PWM, $\theta c2 - \theta c1 = 0$ d) with CPS-PWM, $\theta c2 - \theta c1 = \pi 2$ f) with CPS-PWM, $\theta c2 - \theta c1 = -\pi 2$ 109

Figure 5-1: Numerical result of phase current FFT spectrum without and with CPS-PWM a) current phase A with $M = 0.3$ b) current phase A with $M = 0.6$ c) current phase A with $M = 0.9$ d) current phase B&C with $M = 0.3$ e) current phase B&C with $M = 0.6$ f) current phase B&C with $M = 0.9$ [102]. 116

Figure 5-2: a) & b) Numerical results of current waveform of phase A1 A2 & A3 without CPS-PWM a) One period range of fundamental signal b) Two periods range of carrier signal c) & d) Numerical results of current waveform of phase A1 A2 & A3 with CPS-PWM c) One period range of fundamental signal d) Two periods range of carrier signal [102]. 124

Figure 5-3: a) & b) Simulation results of phase current waveforms of winding configuration $\alpha = 0$ a) without CPS-PWM, $\theta c2 - \theta c1 = 0$ b) with CPS-PWM, $\theta c2 - \theta c1 = \pi$ c) & d) Simulation results of phase current FFT spectrums of winding configuration $\alpha = 0$ c) without CPS-PWM, $\theta c2 - \theta c1 = 0$ d) with CPS-PWM, $\theta c2 - \theta c1 = \pi$.. 128

Figure 5-4: a) & b) & c) Simulation results of phase current waveforms of winding configuration $\alpha = \pi 6$ a) without CPS-PWM, $\theta c2 - \theta c1 = 0$ b) with CPS-PWM, $\theta c2 - \theta c1 = \pi 2$ c) with CPS-PWM, $\theta c2 - \theta c1 = -\pi 2$ d) & e) & f) Simulation results of phase current FFT spectrums of winding configuration $\alpha = \pi 6$ d) without CPS-PWM, $\theta c2 - \theta c1 = 0$ d) with CPS-PWM, $\theta c2 - \theta c1 = \pi 2$ f) with CPS-PWM, $\theta c2 - \theta c1 = -\pi 2$129

Figure 5-5: a) & b) Experimental result of current waveform of phase A1 A2 & A3 without CPS-PWM a) One period range of fundamental signal b) Two periods range of carrier signal c) & d) Experimental results of current waveform of phase A1 A2 & A3 with CPS-PWM c) One period range of fundamental signal d) Two periods range of carrier signal e) Experimental result of phase A1 current FFT spectrum without and with CPS-PWM [102]. 133

Figure 5-6: a) & b) Experimental results of phase current waveforms of winding configuration $\alpha = 0$ a) without CPS-PWM, $\theta c2 - \theta c1 = 0$ b) with CPS-PWM, $\theta c2 - \theta c1 = \pi$ c) & d) Experimental results of phase current FFT spectrums of winding configuration $\alpha = 0$ c) without CPS-PWM, $\theta c2 - \theta c1 = 0$ d) with CPS-PWM, $\theta c2 - \theta c1 = \pi$ 137

Figure 5-7: a) & b) & c) Experimental results of phase current waveforms of winding configuration $\alpha = \pi 6$ a) without CPS-PWM, $\theta c2 - \theta c1 = 0$ b) with CPS-PWM, $\theta c2 - \theta c1 = \pi 2$ c) with CPS-PWM, $\theta c2 - \theta c1 = -\pi 2$ d) & e) & f) Experimental results of phase current FFT spectrums of winding configuration $\alpha = \pi 6$ d) without CPS-PWM, $\theta c2 - \theta c1 = 0$ d) with CPS-PWM, $\theta c2 - \theta c1 = \pi 2$ f) with CPS-PWM, $\theta c2 - \theta c1 = -\pi 2$ 138

List of Tables

Table 3-1: Parameters of 2MW PMSM for Marine propulsion....................................... 48

Table 3-2: Inductance (μH) matrix of FEA (Maxwell) result in distributed winding construction.. 52

Table 3-3: Inductance (μH) matrix of analytical result in distributed winding construction 53

Table 3-4: Inductance (μH) matrix of FEA (Maxwell) result in sectored winding construction.. 54

Table 3-5: Inductance (μH) matrix of analytical result in sectored winding construction 55

Table 4-1: PWM harmonic phase angles (In Radian) of the two three-phase subsystem voltage space vectors ($u1, \mathrm{PWM}(0)$ and $u2, \mathrm{PWM}'(0)$) 77

Table 4-2: PWM harmonic voltage space vector phase angle differences (In Radian) between the two three-phase subsystems (the difference between the phase angle of $u1, \mathrm{PWM}$ and the phase angle of $u2, \mathrm{PWM}'$) 80

Table 4-3: Converter and machine parameters 83

Table 4-4: Converter and Machine Parameters [102] 88

Table 4-5: Parameters of the two machines 95

Table 5-1: Amplitudes of phase current harmonic reduction/increase with CPS-PWM of winding configuration α=π6 (simulation results)... 127

Table 5-2: Amplitudes of phase current harmonic reduction/increase with CPS-PWM of winding configuration α=π6 (experimental results).. 136

List of Acronyms

Back-EMF	Back Electromotive Force
CHB	Cascaded H-Bridge
CPS-PWM	Carrier-based Phase Shift Pulse Width Modulation
CPWM	Carrier-based Pulse Width Modulation
FEA	Finite Element Modulation
FFT	Fast Fourier Transformation
MMF	Magneto-motive Force
NPC	Neutral Point Clamped
PM	Permanent Magnet
PMSM	Permeant Magnet Synchronous Machine
PWM	Pulse Width Modulation
SVM	Space Vector Modulation
THD	Total Harmonic Distortion

Chapter 1 : Introduction

1.1 Motivation for the project

The interest in multiphase machines for high power and reliable drives is continuously growing, and many control algorithms have already been proposed to improve the torque performance of multiphase machines. This thesis presents a new approach to the modelling of multi three-phase drives, aiming at the reducing of the torque ripple introduced by PWM voltage excitation, by the shift of carrier phase angles among different three-phase inverters.

1.2 Overview

Multiphase drives are well known for being a suitable solution for high power systems such as ship propulsion, electric vehicles and More Electric Aircraft applications [1]. Multiphase drives have received growing interest in recent decades, due to their high power density, high reliability and good torque performance [2]. The main advantage of a multiphase drive is the significant improvement in terms of flexibility in the design and control of the converters, and the reduced power rating requirement of the power electronic components [3].

Among the multiphase drives, the multi three-phase layout offers the possibility to obtain a multiphase system by means of commercial three-phase inverters. Furthermore, the multi three-phase layout with parallel or independent dc links offers a higher fault tolerance [4]. A scheme of a multi three-phase drive is presented in Figure 1-1.

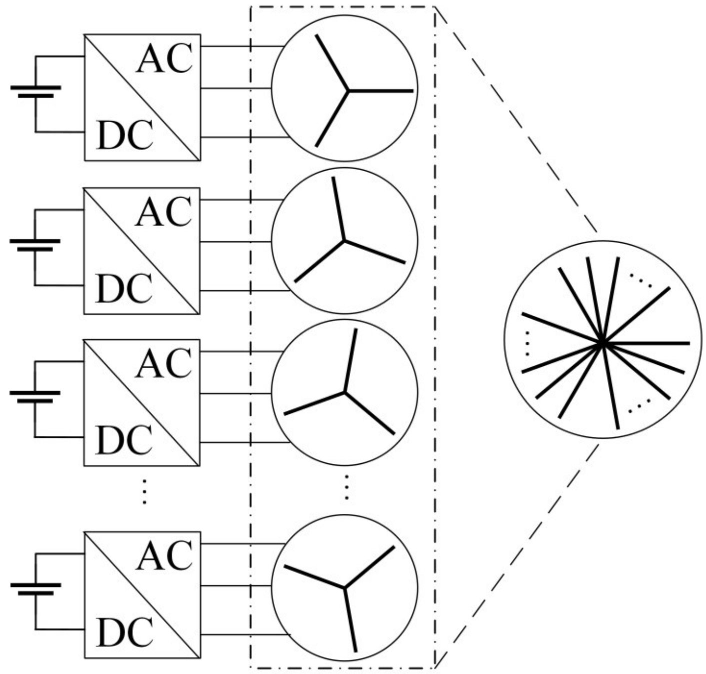

Figure 1-1: Multi three-phase drive system

To achieve high power and high power density drives, one of the main solution is to significantly increase the speed of the machine [5]. However, in high power systems the power electronics must manage high currents (or voltages) and the switching frequency of the power semiconductor is usually limited (below 30 kHz). This results in significant High Frequency current ripple caused by the PWM of the DC/AC converter. The ripple affects the performance of the machine in terms of machine copper loss and torque [6]. In particular, the introduction of HF torque ripple is source of vibrations and noise that are undesired, especially for transport applications with high reliability requirements [7].

The number of output space vectors of SVM grows rapidly with increasing number of phases, which greatly increases the difficulty on the control of multiphase drives. However, the control of three-phase drive can be easily extended to multiphase drives with CPWM

[8]. Therefore, this thesis is mainly focused on CPWM control of voltage converters in multiphase drives.

In a multi three-phase system, the carrier phase angles in different three-phase subsystems is the degrees of freedom in the control, which can be exploited for the cancellation of some magnetic field harmonics in the air gap of the electrical machine. As a result, the introduction of the carrier shift in the control algorithm may lead to an improvement of the torque performance. The vibration and the acoustic noise of the machine can be reduced by applying proper carrier phase shift angles in multi three-phase drive systems [9]–[11]. Therefore, it is important to analyze the relationship between the PWM related torque ripple harmonic components and the carrier phase shift angles in multi three-phase systems.

This thesis proposes an analytical model of the torque ripple generated in a multi three-phase machine fed by a PWM control of multi three-phase modular converters. Starting from the model, a method for the torque ripple reduction by applying a CPS-PWM technique to the multi three-phase inverters is defined. Results of analytical, numerical and FEA simulations are presented and validated by experimental tests.

1.3 Aims and objectives

This thesis aims to present mathematical modellings of multi three-phase drives and improve the torque performance of multi three-phase PMSM by applying proper carrier phase shifts between the three-phase subsystems of the multi three-phase drive.

The objectives are:

- Development of a new approach to modelling of multi three-phase PM machine
- Development of a new approach to modelling of multi three-phase drive with modular PWM voltage source converters
- Proposal of PWM related torque ripple reduction methods on multi three-phase drive with the application of carrier phase shift angles
- Evaluation of the phase currents introduced by the PWM torque ripple reduction method
- Experimental validation of the mathematical models of multi three-phase drive, torque ripple reduction method and the effect on phase currents.

1.4 Thesis outline and content

Chapter 2 presents the literature review of the multi three-phase drive system for the marine application. The overview of the electric machines and the voltage source converters in the multi three-phase drives is presented. The PWM scheme for the control of the voltage source converters with the analytical method to determine the PWM harmonic components are described. Finally, the effect of the PWM harmonics on the machine performance in multi three-phase drives is considered.

Chapter 3 presents mathematical models of arbitrary multi three-phase PMSM. The inductance matrix of arbitrary multi-phase PMSM is analyzed by calculating the flux linkage produced by every single coil of the stator winding, which are validated by the FEA simulation results. The mathematical modelling of the multi three-phase drive is analyzed in both matrix equations and space vector equations.

Chapter 4 shows the mathematical models of the PWM voltage source converters in the multi three-phase drive and the corresponding torque equations based on chapter 3 with the consideration of the PWM harmonics. Numerical, FEA simulations and experimental tests validate the analytical models of the torque equations. The selective torque harmonic elimination method is introduced on a case study of a distributed dual three-phase drive. The selective torque harmonic elimination method is validated by simulation and experimental results.

Chapter 5 analyzes the effect on phase currents applying the proposed carrier phase shift angles by considering the mutual coupling effect between the subsystems in the multi three-phase drive. A sectored triple three-phase machine and a distributed dual three-phase machine are analyzed as case studies. Simulation results and experimental results validate the analytical models of the phase currents in both cases.

Chapter 6 draws a conclusion on this thesis. The significance of the proposed method to improve the torque performance in the multi three-phase drive is summarized. In addition, the future research work including the modelling and the performance improvement on the high power drive systems is listed.

Chapter 2 : Literature review and background

2.1 Electric marine propulsion

There is a growing tendency on using electric ships nowadays. The electric ships have several main advantages compared with traditional ships in terms of its good dynamic response, flexible design options, and high efficiency. In addition, using electric power is known as an environmental-friendly option with reduced emissions [12] [13]. A typical integrated electric ship power system is shown in Figure 2-1. The prime mover is powered by fuel, which rotates the generator to generate the electric power. The electric power drives the main propulsion motor by power converters and offers electric power to other ship service loads [14].

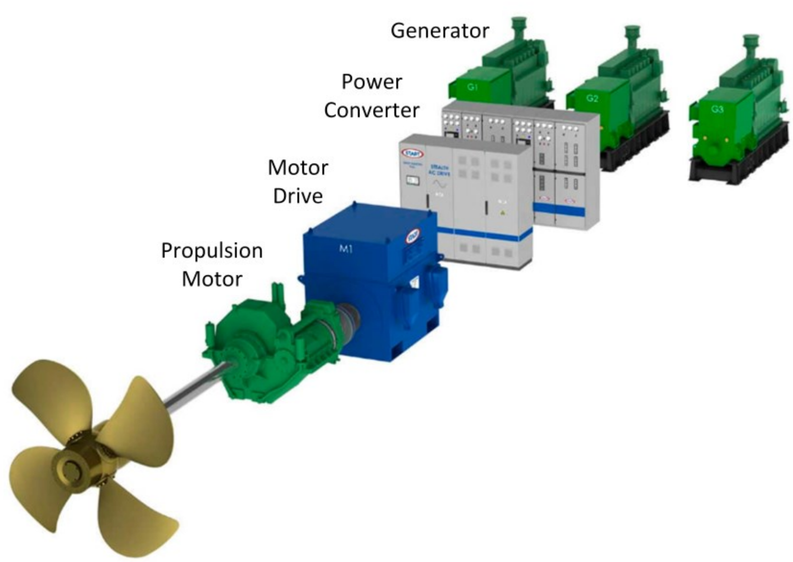

Figure 2-1: Integrated Power system for marine propulsion [15]

The history of the application of electric ships is over 100 years. Nevertheless, the most popular machinery at that stage was steam turbine propulsion, and it turns to diesel engines later on. The prime mover is directly powered by the diesel and there is no need to using electricity distribution systems. Therefore, limited amount of electric ships were used at the period of using diesel engines. In 1980s, with the development of semiconductor switching devices, which enables speed control of the electric machines by using power converters [16]

The speed of the electric machine was not able to be controlled until the switching devices such as thyristors and transistors were applied into high power electrification. The speed of the electric machine was controlled by varying the input voltage, and later the varying of the input frequency became a possible solution. At the first stage, the speed of DC electric machine was controlled by thyristor rectifiers. With the development of converters controlled by varying frequency, the ac motors became a possible solution to be controlled [1].

Multiphase drives are well known for being a suitable solution for high power systems such as ship propulsion [8]. Multiphase drives have received growing interest in recent decades, due to their high power density, high reliability and good torque performance [18]. The main advantage of a multiphase drive is the significant improvement in terms of flexibility in the design and control of the converters, and the reduced power rating requirement of the power electronic components [3].

2.2 Electrical machines for propulsion applications

2.2.1 Overview of electric machines

DC Machine

The DC machine is the one of the main types of rotating machines. There is a commutator inside a DC machine to change the direction of the dc current under each pole, which enables a net positive output torque of the machine. The DC machines have different dynamic and steady state performance with different winding connections (e.g. series connection, shunt connection and compound connection). The mathematical modelling and control algorithm of the DC machines are relatively simple compared with other rotating machines. In recent decades, the development of power electronics enables the control of AC machines. There is a tendency that the AC machine is taking the placement of the DC machine in variety of applications. Nevertheless, the DC machines will continue to be used with their flexibility and simple control of drive systems [19][20].

Induction Machine

The induction machine is a type of AC machine. Both of its stator and rotor consist of windings and the stator windings are connected to the AC power supply. The AC currents in the stator windings generates the rotating magnetic field, which produces rotor winding currents, and therefore produce the torque of the induction motor[20]. This type of machine is called as asynchronous motor, since the speed of the rotor is slower than the magnetic field generated by the stator currents. The induction machine can work under a wide speed range in field-weakening mode and it has the capability of inherent self-start. The Induction machine is easy to manufacture due to the absence of brushes, commutator, and slip ring compared with the DC machine. The induction motor dominates in the market due to its ruggedness, reliability, efficiency and robust [21].

Permanent Magnet Synchronous Machine

Besides the induction machine, the PMSM is another typical kind of AC machine. In PMSM, the stator consists of windings and it will generate the rotating magnetic field while connected to the AC source. The permanent magnet is embedded in the rotor, which rotates at the same speed with the stator magnetic field. The interaction of the two magnetic fields from stator and the rotor produces the torque of the PM machine [22]. The PM material used in PMSM has strong magnetic force, hence the PM machine tends to have large power density and torque density compared with the induction machine and the DC machine. The PMSM is the regarded as the machine with the high efficiency that is around 93% to 98%, since the rotor flux is produced the permanent magnet in the rotor rather than the exciting currents (copper loss and iron loss). Compared to the induction machine with the same power rating, the efficiency of the PMSM is around 5% to 12% higher than the induction machine, and the frame size of the PMSM is 30% smaller than the induction machine [20][23].

2.2.2 Multiphase machines

The three-phase machines were universally used at the beginning of the 20th century as it has better torque performance compared with the one-phase and the two-phase machines that produce the twice pulsating torque ripple. The increasing phase number of the machine will not produce the twice-pulsating torque ripple. The development of the power electronics in 1980s enables the adoption of the machines with more than three phases. The machine can be connected to the power converters rather than directly connected to the three-phase power supply. Therefore, arbitrary phase machine can be used as long as the phase number of the machine matches with the phase number of the power converter [8].

There is a growing concern on multiphase machines after 1990s [23]–[27], especially for the application the electric propulsion [29]–[33]. There are several reasons that the multiphase machine attracts a wide range of interest in the research community. Firstly, the multiphase machine has good fault tolerance performance compared with the conventional three-phase machine [34] [35]. Taking a 15-phase machine as an example, the machine can be operated at over 90% of the rated power with the breakdown of one phase. Secondly, the adoption of multiphase machine greatly reduces the power rating requirement of the power electronic components on each phase leg, which offers the feasibility of the multiphase machine used in high power applications [17], [36]–[39]. Additionally, the flexibility in the design and control of multiphase drive is significantly improved. There are more degrees of freedom in the multiphase drive system, which gives the possibility to cancel the time-domain harmonics and space-domain harmonics in the drive system. Therefore, the efficiency and the torque performance in multiphase is improved compared with the conventional three-phase drives [2], [40]–[47].

Among the multiphase drives, the multi three-phase layout offers the possibility to obtain a multiphase system by means of commercial three-phase inverters. Furthermore, the multi three-phase layout with parallel or independent dc links offers a higher fault tolerance [34]. A scheme of a multi three-phase drive is presented in Figure 1-1. The multi three-phase machine with separate neutral points is one of the most popular option among the multiphase machines with the advantage of the simplicity to implement fault tolerant control [48]. Besides, commercial three-phase inverters can be directly used to the control the multi three-phase machine [41]–[43]. The dual three-phase is one of most commonly used multi three-phase drive, and detailed analysis on the dual three-phase drive is presented in this thesis. The displacement phase angle between the two sets of the three-phase stator windings (in electrical radians) is generally 0 or $\pi/6$ [49]–[53].

2.3 Voltage source converters

2.3.1 The three-phase full bridge converter

Figure 2-2 shows a conventional simplified circuit of two-level three-phase voltage source inverter. A three-phase full bridge converter consists of six groups of active switches (S_1~S_6), and each switch is paralleled with a free-wheeling diode. The function of the inverter is to convert the constant DC link voltage into AC voltage with variable speed and variable frequency. The PWM and SVM are the two general schemes used to control the two-level three-phase inverter [55].

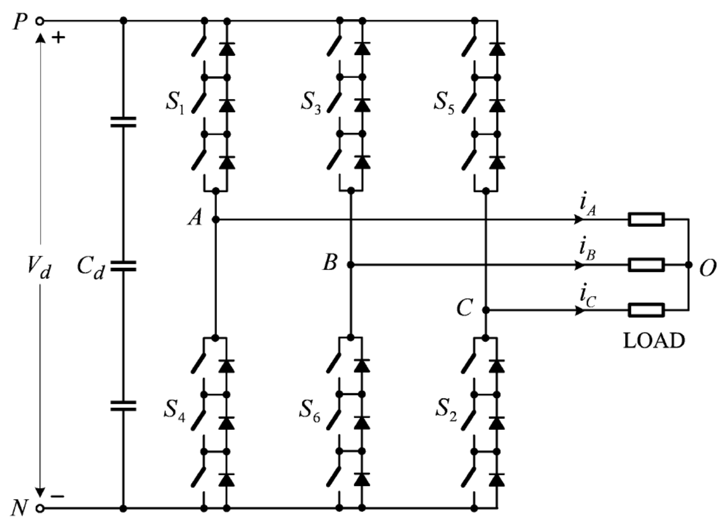

Figure 2-2：Three-phase full bridge converter for high-power applications (with series connected switches) [55]

The conventional three-phase full bridge can be applied into high power applications with the power rating up to a few megawatts [56]. The two-level three-phase converter dominates in the market due to its simple control algorithm, high reliability, simple capacitor pre-charging circuit and the low manufacturing cost. However, the two-level three-phase full bridge converter has the disadvantage that it has high dv/dt output voltage, which may lead to the short circuit machine winding and bearing failure [57]. In addition, the switching frequency of the two-level converter for high power applications is low due to the limitation of switching devices, which leads to current harmonics in the machine stator windings and power loss in the machine.

2.3.2 Multilevel converters for high power applications

This section presents a brief overview of typical multilevel converters including neutral-point clamped inverter, cascaded H-bridge inverter and flying capacitor inverter for high power applications. The per-phase diagram of voltage source inverter topologies of the two-level inverter and the three types multilevel converters are shown in Figure 2-3 [55].

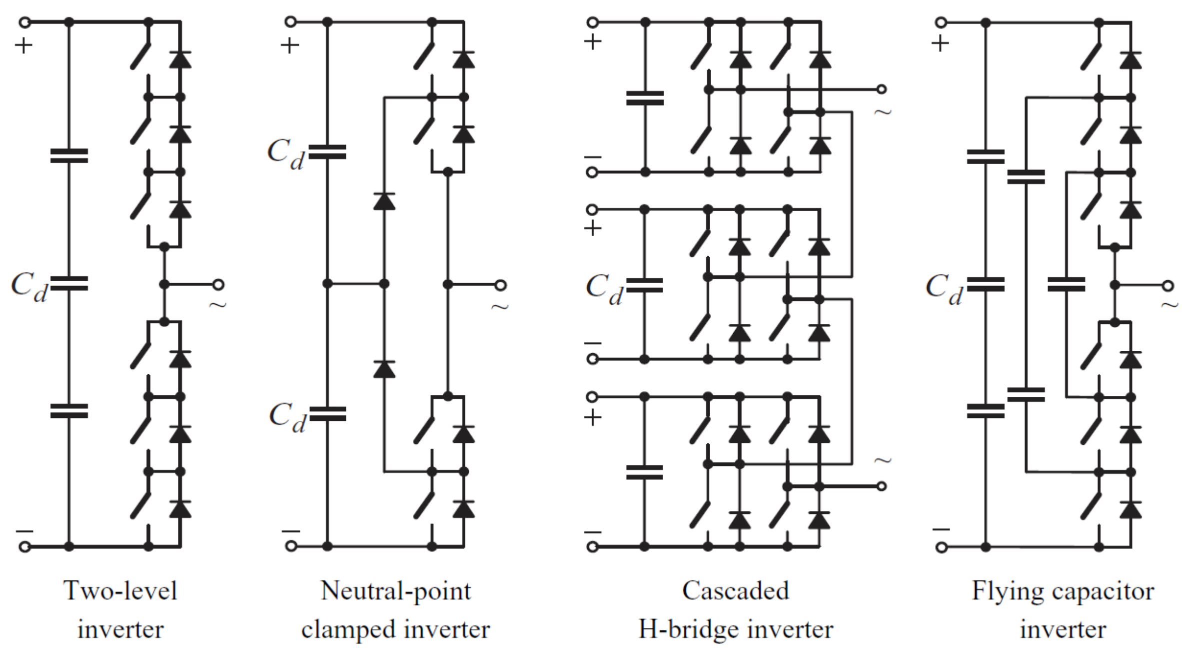

Figure 2-3: Topologies of phase voltage source inverters [55]

Neutral-point clamped inverter

The neutral-point clamped (NPC) inverter is one of the most commonly used diode-clamped multilevel inverter in high power medium voltage applications, which is shown in Figure 2-3 [58] [59]. The NPC inverter is widely manufactured and dominates the market as a commercial product [60]–[63]. An NPC inverter phase leg consists of four switches and four antiparallel diodes. There are two capacitors on the dc side, which is split by the neutral point connected by the two clamped diodes on the other side.

Compared to the two-level three-phase converter, the NPC inverter has reduced dv/dt due to the increased number of voltage level. Besides, the effective switching frequency is doubled compared the two-level converter, resulting in a reduced THD of ac output voltage. Additionally, all the switches in the NPC inverter bear the same voltage (half of the dc link) and the dynamic voltage is balanced on each switch. Nevertheless, the main disadvantage of the NPC inverter is that the complexity on the modulation scheme is increased due to the increased number of the ac output voltage levels. Further control algorithm needs to be adopted to control the voltage variation on the neutral point. Besides, additional clamped diodes are used compared with the two-level converter with the same power rating [64]–[66].

Cascaded H-bridge inverter

The cascaded H-bridge (CHB) is another widely used multilevel inverter for high power medium voltage applications, which is shown in Figure 2-3 [67]–[70]. The H-bridge modules in the CHB inverter are the supplied with isolated dc links, and they are connected in series on the ac side. The number of the cascaded H-bridge cell in the CHB inverter determines the power and voltage capacity of the CHB inverter, and the ac output voltage THD. The level of ac output voltage depends on the number of cascaded H-bridge modules.

For instance, if there is m H-bridge per leg, then the phase voltage has 2m+1 levels and line-to-line voltage has 4m+1 levels.

Compared with the conventional two-level three-phase converter, the CHB inverter has reduced dv/dt due to the increased number of voltage levels. Besides, the effective switching frequency is proportional to the level of the ac output voltage, resulting in a reduced THD of ac output voltage. Additionally, the CHB inverter is composed of identical modular H-bridges, which leads to a lower manufacture cost on each module. Nevertheless, the CHB inverter has the disadvantage that it has large number of isolates dc links, hence the transformers is employed. Moreover, the CHB inverter has larger number of switching devices with anti-parallel diodes compared with the two-level inverter. The increased number of the components and the adoption of the transformer increases the size, complexity and cost of the CHB inverter [55].

Flying capacitor inverter

A three-level flying capacitor topology is shown in Figure 2-3. The difference between the two-level inverter and the flying capacitor inverter is that the dc capacitors are inserted to the cascaded switches [71][72]. The gate signals of the upper groups of the three switches are always the opposite with the lower groups of the three switches, hence three independent drive signals are supposed to drive a three-level flying capacitor inverter.

As a multilevel converter, with the same characteristics of the NPC inverter and the CHB inverter, the flying capacitor inverter has reduced dv/dt and THD due to the increased number of the output voltage levels. However, the flying capacitor has two main drawbacks. Firstly, each of the flying capacitor needs to be pre-charged and maintained at a constant value, and hence each dc capacitor requires a pre-charge circuit. Secondly, the complex control algorithm is required to control the voltage variation on each capacitor, as the voltage on each capacitors changes with the operating conditions of the converter. The two main drawback limits the application of the flying capacitor in the market [73].

2.3.3 Parallel converters

Figure 2-4 show that the parallel converters are used to control the multi single-phase and multi three-phase drives respectively. The DC/AC module in Figure 2-4 can either a 2-level three-phase inverter in Section 2.3.1, or a multilevel inverter in Section 2.3.2. The adoption of parallel converters make it possible to control very high power and high speed machines with commercial products, since the power requirement on each inverter module is reduced. Moreover, this topology has high fault tolerance, as any inverter module is independent without any electrical connections to the other modules [34]. Besides, the adoption of the parallel converters increase the flexibility of the control algorithm. The torque ripple, noise and vibration of the machine, and the dc link voltage ripple are possibly to be reduced by applying proper control scheme. However, the increasing number of the inverter modules results in a more complex control algorithm. In addition, synchronous gate signals are required to drive the parallel converter modules [74] [75].

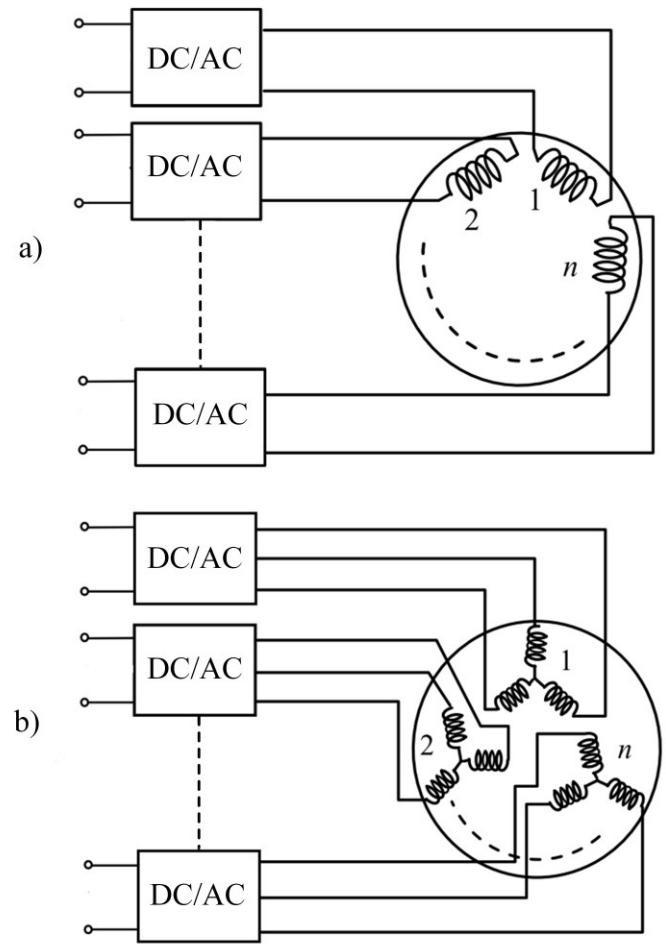

Figure 2-4: a) Multi single-phase drive with parallel converters b) Multi three-phase drive with parallel converters [76]

2.4 Modulation techniques for voltage source converters

2.4.1 Space vector modulation

The space vector modulation (SVM) is one of the most commonly used modulation technique for the digital control of the voltage source converters. The form of SVM technique was proposed in the mid of 1980s [77]. The working principle of the SVM technique is to generate an average output voltage with respect to the reference voltage by selecting the potential switching states with their corresponding dwell time. The implementation of SVM can be divided into three stages: define the switching states, calculate the dwell time and choose the switching sequence. The SVM has the advantage that it is inherently digital and it is simple to implement in hardware and software [78][79]. In addition, the SVM has better DC link utilization compared with CPWM [80] [81]. However, the number of the switching states is related to the phase number of the converter and the level of the ac output voltage. Taking an m-phase converter with n-level ac output voltage as an example, the total number of the switching states is n^m. The increasing number of the phase number and the output voltage level will increase the complexity of the implementation of the SVM [82] [83].

2.4.2 Carrier-based pulse width modulation

The carrier-based pulse width modulation (CPWM) is known as the earliest and most straightforward modulation technique [84]. The working principle of the CPWM is to compare the reference modulating signal with the high frequency carrier signal to determine the switching states of the converters. If the modulating signal is lower than the carrier signal, the lower switch of the converter leg is switched on; if the modulating signal is larger than the carrier signal, the upper switch of the converter leg is switched on. Compared with the SVM, the CPWM has lower dc link voltage utilization [85]. This drawback can be avoided by the injection of the zero-sequence harmonics [86]. The implementation of CPWM is straightforward and it can be extended to the control of the multi-phase multi-level converters without greatly increase the complexity of the control algorithm.

Phase-shifted CPWM and level-shifted CPWM are the two main types of CPWM that are applied to the control of multilevel converters. Assuming the number of ac output voltage level is m, the corresponding number of the required carriers is m-1. As for the phase-shifted CPWM, the basic working principle of the phase-shifted CPWM is that the phase angle difference between any contiguous carriers is set to be $\frac{2\pi}{m-1}$. Considering the level-shifted CPWM, the amplitudes of the carrier signal in phase-shifted CPWM are equally divided into m-1 parts, and they are vertically placed to compare with the modulating signal. The phase-shifted PWM has the same switching frequency and the same conducting periods, while the level-shifted PWM has different switching frequency and conducting periods. Therefore, the rotating of switching patterns is required on the level-shifted PWM. Due to the uneven power distribution on the power switches of the converter of the phase-shifted PWM, the carrier-shifted PWM is preferred on the CHB inverter and the flying capacitor inverter [69] [87].

2.4.3 Double Fourier integral analysis method of pulse width modulation

According to [84], if the function of both $x(t)$ and $y(t)$ are periodic functions, the function of $f(x,\ y)$ can be represented as the summation of sinusoidal harmonics. Assuming the period of both the functions $x(t)$ and $y(t)$ is 2π, the function of $f(x,\ y)$ can be represented as:

$$\begin{aligned} f(x,y) &= \frac{A_{00}}{2} + \textstyle\sum_{n=1}^{\infty}[A_{0n}\cos ny + B_{0n}\sin ny] \\ &+ \textstyle\sum_{m=1}^{\infty}[A_{m0}\cos mx + B_{m0}\sin mx] \\ &+ \textstyle\sum_{m=1}^{\infty}\sum_{n=-\infty}^{\infty}[A_{mn}\cos(mx+ny) + B_{mn}\sin(mx+ny)], \end{aligned} \tag{2-1}$$

with:

$$A_{mn} = \frac{1}{2\pi^2}\int_{-\pi}^{\pi}\int_{-\pi}^{\pi} f(x,y)\cos(mx+ny)\,dxdy, \tag{2-2}$$

$$B_{mn} = \frac{1}{2\pi^2}\int_{-\pi}^{\pi}\int_{-\pi}^{\pi} f(x,y)\sin(mx+ny)\,dxdy. \tag{2-3}$$

where m and n are the positive integer numbers.

Sine-triangle modulation is one of the most commonly used CPWM. Figure 2-5a shows the x-y plane of the sin-triangle modulation, which is presented by the function $f(x,y)$. The blue area represents the parts when the upper switch of the phase leg is turned on, and the white area represents the parts when the lower switch of the phase leg is turned on [88]. The x-axis and the y-axis are considered as the time-varying angle of the carrier signal and the time-varying angle of the modulating signal respectively. The straight line in Figure 2-5a shows the function of $y(x)$. The slope of the function $y(x)$ is the ratio between the modulating signal frequency and the carrier signal frequency. The intersection points between the function $y(x)$ and the changing boundaries of the function $f(x,y)$ are the switching time instants of the converter. The corresponding PWM output voltage waveform is shown in Figure 2-5b.

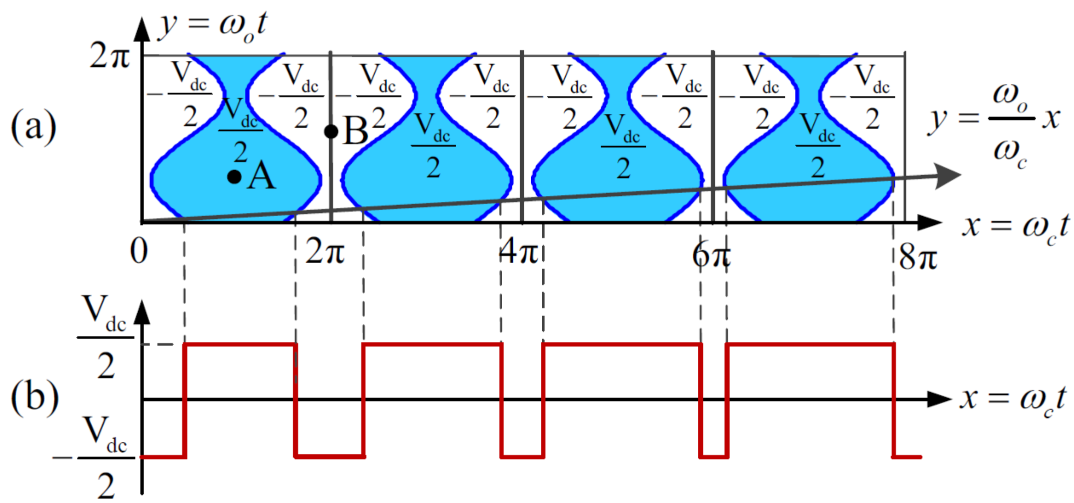

Figure 2-5: (a) The x-y plane for the sine-triangle modulation (b) The x-y plane for the corresponding PWM output voltage [89]

The time varying modulating signal can be presented as:

$$V_m(t) = M\cos y, \tag{2-4}$$

where M is the modulation index, y is the time varying angle of the modulating signal.

With respect to (2-4), the intersection points in Figure 2-5a can be given as two cases:

for the function $f(x,y)$ changes from $-\frac{V_{dc}}{2}$ to $\frac{V_{dc}}{2}$, the switching instants happens at:

$$x = 2\pi p + \frac{\pi}{2}(1 + M\cos y), p = 0, 1, 2, 3, \ldots \tag{2-5}$$

for the function $f(x,y)$ changes from $\frac{V_{dc}}{2}$ to $-\frac{V_{dc}}{2}$, the switching time happens at:

$$x = 2\pi p - \frac{\pi}{2}(1 + M\cos y), p = 0, 1, 2, 3, \ldots \tag{2-6}$$

The switching time instants in (2-5) and (2-6) are the upper and the lower integral limits in (2-2) and (2-3) respectively. The function of $f(x, y) = \frac{V_{dc}}{2}$ between the upper and the lower limits. Substituting (2-5) and (2-6) into (2-2) and (2-3), A_{mn} and B_{mn} can be rewritten as:

$$A_{mn} = \frac{1}{2\pi^2} \int_{-\pi}^{\pi} \int_{-\frac{\pi}{2}(1+M\cos y)}^{\frac{\pi}{2}(1+M\cos y)} \frac{V_{dc}}{2} \cos(mx + ny)\, dxdy, \tag{2-7}$$

$$B_{mn} = \frac{1}{2\pi^2} \int_{-\pi}^{\pi} \int_{-\frac{\pi}{2}(1+M\cos y)}^{\frac{\pi}{2}(1+M\cos y)} \frac{V_{dc}}{2} \sin(mx + ny)\, dxdy. \tag{2-8}$$

Substituting (2-7) and (2-8) into (2-1), and replacing x and y with $\omega_c t + \theta_c$ and $\omega_o t + \theta_o$ respectively, the function of $f(t)$ can be expressed as:

$$\begin{aligned} f(t) = {} & \underbrace{\frac{V_{dc}}{2}}_{DC\ offset} + \underbrace{\frac{V_{dc}}{2} M\cos(\omega_o t + \theta_o)}_{fundamental\ component} \\ & + \underbrace{\frac{4V_{dc}}{\pi} \sum_{m=1}^{\infty} \frac{1}{m} J_0\left(m\frac{\pi}{2}M\right) \sin m\frac{\pi}{2} \cos(m[\omega_c t + \theta_c])}_{carrier\ harmonics} \\ & + \underbrace{\frac{4V_{dc}}{\pi} \sum_{m=1}^{\infty} \sum_{n=-\infty}^{\infty} \frac{1}{m} J_n\left(m\frac{\pi}{2}M\right) \sin\left([m+n]\frac{\pi}{2}\right) \cos(m[\omega_c t + \theta_c] + n[\omega_o t + \theta_o])}_{sideband\ harmonics}, \end{aligned} \tag{2-9}$$

where θ_o is the initial phase angle of the modulating signal and θ_c is the initial phase angle of the carrier signal.

By using the double Fourier integral method, the time-varying phase leg voltage of $f(t)$ can be expressed with all the harmonics components in (2-9).

2.5 The PWM harmonic effect on the machine performance

The pulse width modulation (PWM) technique for the control of the power converters is one of the main factors that leads to the machine torque ripple [90]–[94]. The PWM related torque ripple harmonic components are the source of vibration, acoustic noise [95]–[97] and affect machine power loss [98], [99]. Taking a dual three-phase system as an example, the carrier phase angle difference between the two three-phase subsystems is a degree of freedom in the control, which can be exploited for the cancellation of some magnetic field harmonics in the air gap of the electrical machine. As a result, the introduction of the carrier shift in the control algorithm may lead to an improvement of the torque performance [49]. The vibration and the acoustic noise of the machine can be reduced by applying proper carrier phase shift angles in dual three-phase drive systems [11] [100].

In [11], for a dual three-phase drive system without phase displacement, the vibration of the system is effectively improved when the carrier phase shift angle π is applied between the two subsystems in the dual three-phase drive at the PWM switching frequency of 4 kHz. Figure 2-6 shows the experimental results that the vibration harmonics around 4 kHz (once the PWM frequency) and 12 kHz (three times the PWM frequency) are effectively eliminated with the proposed carrier phase shift method. It is demonstrates in [100] that the acoustic noise amplitude is decreased by 15.43% with the proposed carrier phase shift angle in a dual three-phase system. Xu (2019) shows that, for a dual three-phase drive with the phase displacement of $\frac{\pi}{6}$, the torque ripple harmonic components at the second order of the PWM switching frequency are effectively be eliminated with applying carrier phase angle of $\frac{\pi}{4}$ between the two subsystems [54].

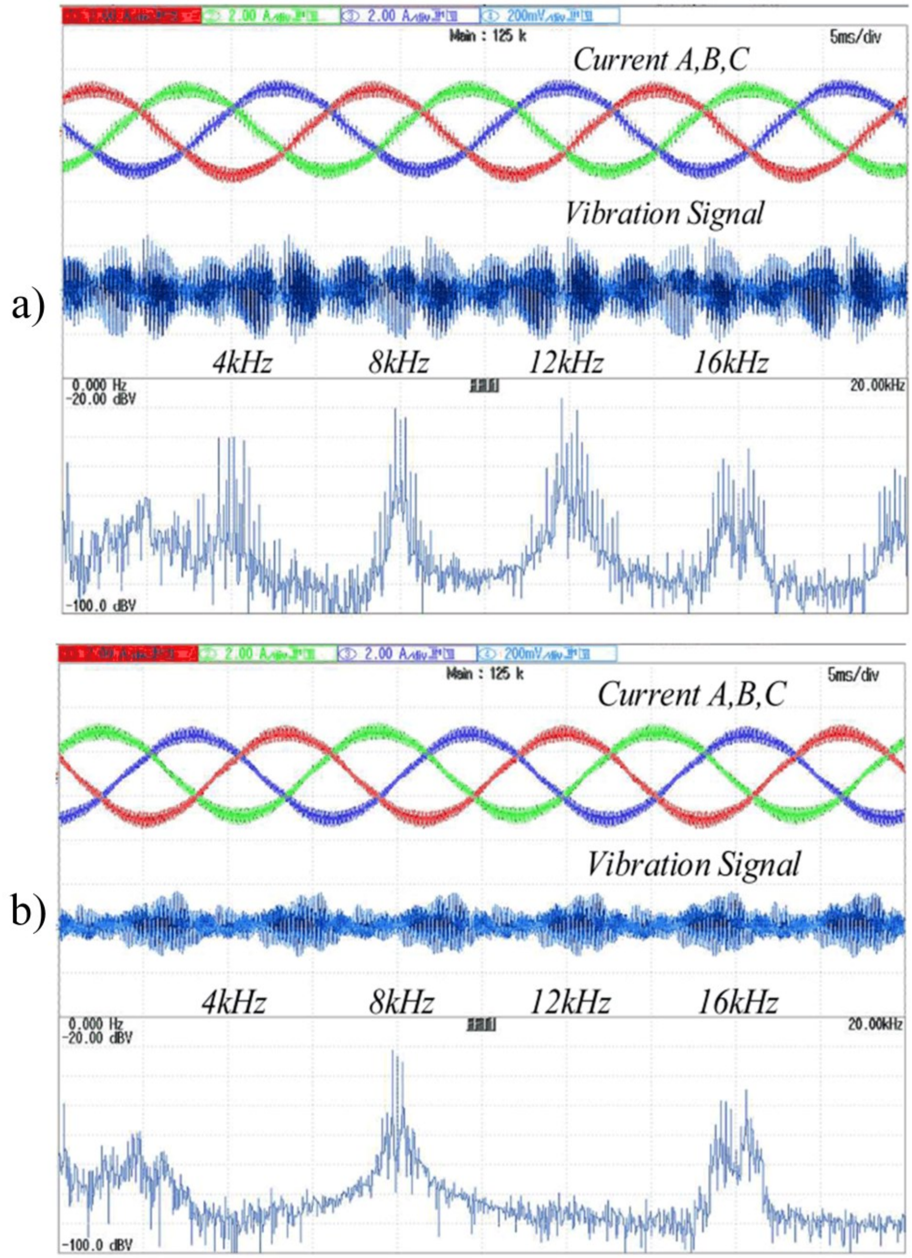

Figure 2-6: The vibration signal waveforms and their corresponding FFT spectra a) without the proposed carrier phase shift b) with the proposed carrier phase shift [11]

Therefore, it is important to analyze the relationship between the PWM related torque ripple harmonic components and the carrier phase shift angles in multi three-phase systems. An analytical model of the torque ripple generated in a multi three-phase machine fed by a

PWM control of multi three-phase modular converters is analyzed in this thesis. Starting from the model, a method for the torque ripple reduction by applying a CPS-PWM technique to the multi three-phase inverters is defined. Taking a dual three-phase drive as an example, this work presents how the PWM related torque ripple harmonic components can be eliminated by applying CPS-PWM in the drive system with arbitrary phase angle displacement. Two dual three-phase PMSM with phase displacement of 0 and $\pi/6$, considering as two case studies, are considered with their respective CPS-PWM.

Chapter 3 : Modelling of multi three-phase machines

3.1 Inductance analysis of arbitrary phase PMSM

There are two main ways to analyze inductance, including the permeance of magnetic circuit analysis method and the magnetic field analysis method [21]. In this thesis, the permeance analysis method is discussed. In the analysis process of this section, the effect of iron saturation is neglected, which means that the reluctance of magnetic circuit is a constant value and it does not vary with the flux density. Additionally, the effect of some secondary factors such as the hysteresis and eddy-current are neglected. Besides that, the effect on slot harmonics and iron reluctance is not considered for simplicity's sake.

The flux-linkages produced by loop currents in AC machines can be divided into two main parts, including the air-gap flux linkage and the leakage flux linkage. The air-gap flux linkage is the main part which links the stator and the rotor through the air gap. The inductance produced by leakage flux including two parts, one is the inductance produced by slot leakage flux and the other is the inductance produced by the end region leakage flux. With regard to the inductance produced by slot leakage flux, the mutual inductance produced by the slot leakage flux exists only between the coil bars in the same slot. For the inductance produced by end region leakage flux, it is very difficult to calculate exactly the inductance produced by end region leakage flux.

The inductance is analyzed with a single coil as a minimum unit in this thesis, thus it can be extended to arbitrary phase machines with different winding configurations. In this thesis, only the air-gap flux linkage produced by stator coils is considered, and all of the leakage flux linkage is neglected.

3.1.1 Air-gap MMF produced by single coil current

The rectangular MMF caused by the electric current passes through stator coil AA' is shown in Figure 3-1.

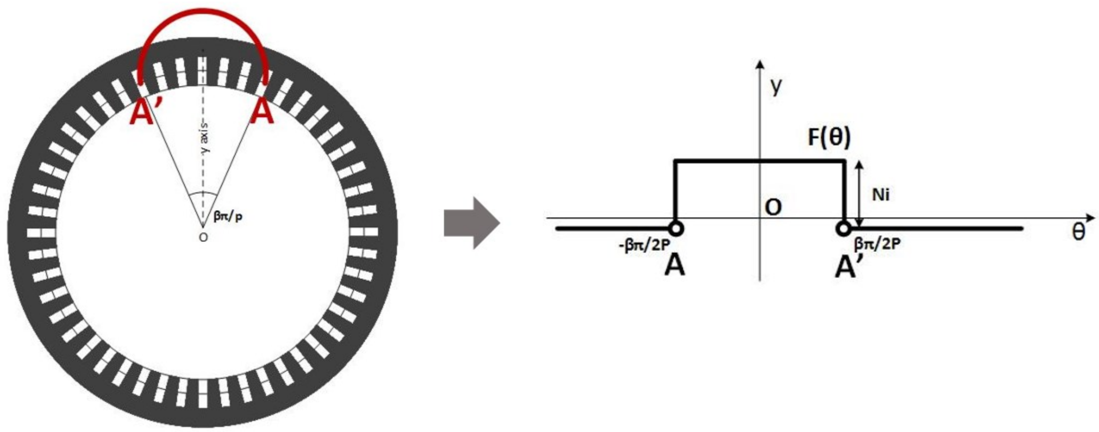

Figure 3-1: Air-gap MMF produced by the current of stator coil AA'

In Figure 3-1, $F(\theta)$ represents the MMF produced by a single coil. θ is the horizontal axis, which represents the mechanical angle of the electric machine. y is the vertical axis, which is the centreline of coil AA', and represents the MMF generated by the coil AA'. According to Kirchhoff's first law, the average value of $F(\theta)$ over one period (-π, π) is 0. Hence there is no dc component of function $F(\theta)$. y is the centreline of coil AA', which means the $F(\theta)=F(-\theta)$. Therefore $F(\theta)$ is an even function with only cosine components and without dc component. The function $F(\theta)$ can be written as:

$$F(\theta) = \sum_n a_n \cos n\theta , \qquad n = 1,2,3, \dots \tag{3-1}$$

with:

$$a_n = \frac{1}{\pi}\int_{-\pi}^{\pi} F(\theta) \cos n\theta \, d\theta = \frac{2}{n\pi} iN \sin\frac{n\beta\pi}{2P}. \tag{3-2}$$

where P is pole-pair number; β is ratio of actual pitch to full pitch; N is the turn number of the coil.

3.1.2 Self-inductance of a single coil

For a non-salient machine, the air-gap permeance coefficient λ can be assumed to be a constant value. F_n represents the n^th harmonic of MMF produced by the current of single coil AA'. The n^th harmonic flux density B_n produced by the corresponding MMF F_n can be obtained as:

$$B_n = F_n \times \lambda. \tag{3-3}$$

The n^th self flux-linkage of coil AA' can be obtained as follows:

$$\Psi_n = N \int_{S_1}^{S_2} B_n \, ds, \tag{3-4}$$

where R is the stator inner radius; l is the stator iron length; θ is the mechanical angle of the electric machine. Since $ds = d(\theta Rl) = Rld\theta$, the n^th self flux-linkage of coil AA' Ψ_n can be rewritten as:

$$\Psi_n = NRl \int_{\theta_1}^{\theta_2} B_n \, d\theta. \tag{3-5}$$

As shown in Figure 3-1, for coil AA', $\theta_1 = -\frac{\beta\pi}{2P}$ and $\theta_2 = \frac{\beta\pi}{2P}$ respectively. Substituting the values of θ_1 and θ_2 into (3-5), the n^th self flux-linkage of coil AA' Ψ_n can be rewritten as:

$$\Psi_n = NRl \int_{-\frac{\beta\pi}{2P}}^{\frac{\beta\pi}{2P}} B_n \, d\theta = NRl \int_{-\frac{\beta\pi}{2P}}^{\frac{\beta\pi}{2P}} \lambda a_n \cos n\theta \, d\theta = \frac{4iN^2\lambda Rl}{n^2\pi} (\sin\frac{n\beta\pi}{2P})^2. \tag{3-6}$$

The self inductance L of the coil AA' produced by the total air-gap magnetic flux linkage Ψ is represented as:

$$L = \frac{\Psi}{i} = \frac{\sum \Psi_n}{i} = \frac{4N^2 \lambda R l}{\pi} \sum_n \frac{(\sin\frac{n\beta\pi}{2P})^2}{n^2} \quad n = 1,2,3,\ldots \tag{3-7}$$

3.1.3 Mutual inductance between two coils

The process to calculate the mutual inductance between stator winding coils is similar with the process to calculate the self inductance of a single coil which is shown in Section 3.1.2. While considering the mutual inductance between coils, an additional variable α (the space shift angle of the two coils), is taken into account. As it is shown in

Figure 3-2, the centerline of coil BB' leads the centerline of AA' by α (mechanical angle). In this case, the lower limit and the upper limit of the integral are $\alpha - \frac{\beta\pi}{2P}$ and $\alpha + \frac{\beta\pi}{2P}$ respectively.

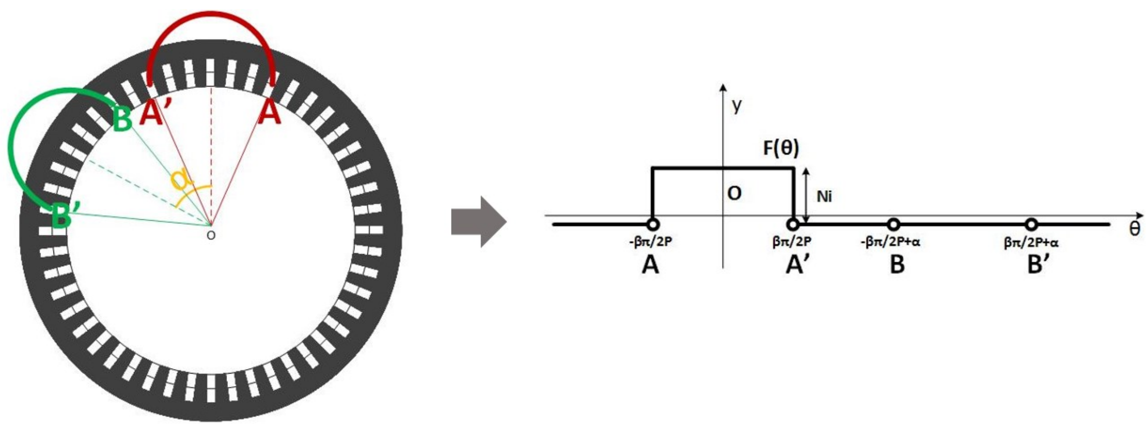

Figure 3-2: Stator coil AA' and stator coil BB'

The nth mutual flux linkage between coil AA' and coil BB' can be represented as:

$$\Psi_{ABn} = NRl \int_{\alpha-\frac{\beta\pi}{2P}}^{\alpha+\frac{\beta\pi}{2P}} B_n \, d\theta = \frac{4iN^2\lambda Rl}{n^2\pi} (\sin\frac{n\beta\pi}{2P})^2 \cos n\alpha. \tag{3-8}$$

The mutual inductance between coil AA' and coil BB' caused by total air-gap flux linkage is written as:

$$M_{AB} = \frac{\Psi_{AB}}{i} = \frac{\sum \Psi_{ABn}}{i} = \frac{4N^2\lambda Rl}{\pi}\sum_n \frac{(\sin\frac{n\beta\pi}{2P})^2}{n^2}\cos n\alpha \quad n = 1,2,3,\ldots \tag{3-9}$$

3.1.4 Self-inductance of two single coils

The self inductance of any two single coils can be obtained based on the calculation of self inductance on single coil in Section 3.1.2. As it is shown in Figure 3-3, the coil A_2A_2' leads A_1A_1' by ε (mechanical angle). The self-inductance of the two single coils can be obtained through the total flux linkage produced the two single coils. For coil A_1A_1', the flux linkage is calculated through the integration of the flux density with the lower limit and upper limit is $-\frac{\beta\pi}{2P}$ and $+\frac{\beta\pi}{2P}$ respectively. For coil A_2A_2', the flux linkage is calculated through the integration of the flux density with the lower limit and the upper limit of the integral $\varepsilon - \frac{\beta\pi}{2P}$ and $\varepsilon + \frac{\beta\pi}{2P}$ respectively.

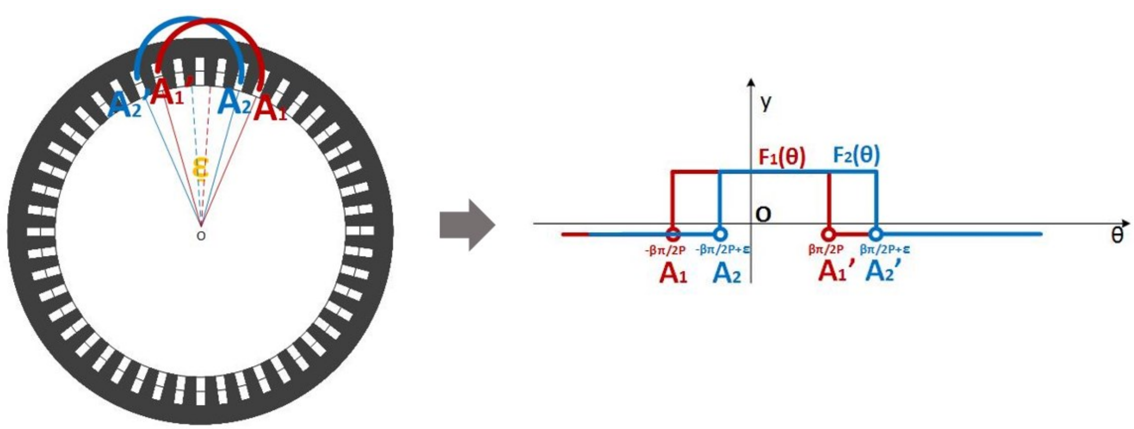

Figure 3-3: Air-gap MMF produced by the current of stator coil A_1A_1' and A_2A_2'

$F_1(\theta)$ represents the MMF produced by the single coil A_1A_1', and the function *$F_1(\theta)$* can be written as:

$$F_1(\theta) = \sum_n a_n \cos n\theta\,, \qquad n = 1,2,3,\ldots \tag{3-10}$$

$F_2(\theta)$ represents the MMF produced by the single coil A_2A_2'. *$F_2(\theta)$* is the function *$F_1(\theta)$* translate through horizontal axis by ε, and the function *$F_2(\theta)$* can be written as:

$$F_2(\theta) = \sum_n a_n \cos n(\theta + \varepsilon), \qquad n = 1,2,3 \ldots \tag{3-11}$$

$F(\theta)$ represents the total MMF produced by coil A_1A_1' and A_2A_2', which can be written as:

$$F(\theta) = F_1(\theta) + F_2(\theta) = \sum_n a_n [\cos n\theta + \cos n(\theta + \varepsilon)] \quad n = 1,2,3, \ldots \tag{3-12}$$

The n^{th} harmonic flux density produced by the n^{th} MMF can be obtained as:

$$B_n = F_n \times \lambda = (F_{1n}(\theta) + F_{2n}(\theta)) \times \lambda. \tag{3-13}$$

The total flux-linkage of coil A_1A_1' can be obtained as follows:

$$\Psi_{1n} = N \int_{S_1}^{S_2} B_n \, ds = NRl \int_{-\frac{\beta\pi}{2P}}^{\frac{\beta\pi}{2P}} B_n \, d\theta = \frac{4iN^2\lambda Rl}{n^2\pi} (\sin\frac{n\beta\pi}{2P})^2 (1 + \cos n\varepsilon). \tag{3-14}$$

The total flux-linkage of coil A_2A_2' can be obtained as follows:

$$\Psi_{2n} = N \int_{S_1}^{S_2} B_n \, ds = NRl \int_{\varepsilon-\frac{\beta\pi}{2P}}^{\varepsilon+\frac{\beta\pi}{2P}} B_n \, d\theta = \frac{4iN^2\lambda Rl}{n^2\pi} (\sin\frac{n\beta\pi}{2P})^2 (1 + \cos n\varepsilon). \tag{3-15}$$

The total flux-linkage of coil A_1A_1' and A_2A_2' can be obtained as follows:

$$\Psi_n = \Psi_{1n} + \Psi_{2n} = \frac{8iN^2\lambda Rl}{n^2\pi} (\sin\frac{n\beta\pi}{2P})^2 (1 + \cos n\varepsilon). \tag{3-16}$$

The total self inductance of the coil A_1A_1' and A_2A_2' produced by total air-gap magnetic flux linkage is:

$$L = \frac{\Psi_1 + \Psi_2}{i} = \frac{\sum(\Psi_{1n} + \Psi_{2n})}{i} = \frac{8N^2\lambda Rl}{\pi} \sum_n \frac{(\sin\frac{n\beta\pi}{2P})^2}{n^2} (1 + \cos n\varepsilon) \quad n = 1,2,3, \ldots \tag{3-17}$$

3.2 Analytical matrix torque equations of multi three-phase machines

3.2.1 Matrix inductance table of multi three-phase machines

While considering the self-inductance and mutual inductance of the inductance matrix table, the effect of iron saturation is not taken into account, which means that the inductance value does not vary with the flux density. Assuming the self-inductance value on each stator phase a_1, b_1, c_1, …, a_N, b_N, c_N are represented by $L_{\mathrm{a}_1\mathrm{a}_1}$, $L_{\mathrm{b}_1\mathrm{b}_1}$, $L_{\mathrm{c}_1\mathrm{c}_1}$, …, $L_{\mathrm{a}_N\mathrm{a}_N}$, $L_{\mathrm{b}_N\mathrm{b}_N}$, $L_{\mathrm{c}_N\mathrm{c}_N}$ respectively. Assuming the mutual-inductance value between phase a_1, b_1, c_1, …, a_N, b_N, c_N are represented by $M_{a_1\mathrm{b}_1}$, $M_{\mathrm{a}_1\mathrm{c}_1}$, …, $M_{\mathrm{c}_N a_N}$, $M_{\mathrm{c}_N b_N}$ respectively. The matrix inductance table is a $3N \times 3N$ matrix table, which can be represented by $\boldsymbol{L}$:

$$\boldsymbol{L} = \begin{bmatrix} L_{\mathrm{a}_1\mathrm{a}_1} & M_{\mathrm{a}_1\mathrm{b}_1} & M_{\mathrm{a}_1\mathrm{c}_1} & & M_{\mathrm{a}_1\mathrm{a}_N} & M_{\mathrm{a}_1\mathrm{b}_N} & M_{\mathrm{a}_1\mathrm{c}_N} \\ M_{\mathrm{b}_1\mathrm{a}_1} & L_{\mathrm{b}_1\mathrm{b}_1} & M_{\mathrm{b}_1\mathrm{c}_1} & \cdots & M_{\mathrm{b}_1\mathrm{a}_N} & M_{\mathrm{b}_1\mathrm{b}_N} & M_{\mathrm{b}_1\mathrm{c}_N} \\ M_{\mathrm{c}_1\mathrm{a}_1} & M_{\mathrm{c}_1\mathrm{b}_1} & L_{\mathrm{c}_1\mathrm{c}_1} & & M_{\mathrm{c}_1\mathrm{a}_N} & M_{\mathrm{c}_1\mathrm{b}_N} & M_{\mathrm{c}_1\mathrm{c}_N} \\ & \vdots & & \ddots & & \vdots & \\ M_{\mathrm{a}_N\mathrm{a}_1} & M_{\mathrm{a}_N\mathrm{b}_1} & M_{\mathrm{a}_N\mathrm{c}_1} & & L_{\mathrm{a}_N\mathrm{a}_N} & M_{\mathrm{a}_N\mathrm{b}_N} & M_{\mathrm{a}_N\mathrm{c}_N} \\ M_{\mathrm{b}_N\mathrm{a}_1} & M_{\mathrm{b}_N\mathrm{b}_1} & M_{\mathrm{b}_N\mathrm{c}_1} & \cdots & M_{\mathrm{b}_N\mathrm{a}_N} & L_{\mathrm{b}_N\mathrm{b}_N} & M_{\mathrm{b}_N\mathrm{c}_N} \\ M_{\mathrm{c}_N\mathrm{a}_1} & M_{\mathrm{c}_N\mathrm{b}_1} & M_{\mathrm{c}_N\mathrm{c}_1} & & M_{\mathrm{c}_N\mathrm{a}_N} & M_{\mathrm{c}_N\mathrm{b}_N} & L_{\mathrm{c}_N\mathrm{c}_N} \end{bmatrix}.$$

Assuming i and j represent the i^{th} row and the j^{th} column of matrix $\boldsymbol{L}$ respectively. Due to the mutual inductance theory, $M_{ij} = M_{ji}$, so Matrix $\boldsymbol{L}$ is a real symmetric matrix. The Matrix $\boldsymbol{L}$ is strictly diagonally dominant matrix where $L_{ii} > \sum_{j=1,j\neq i}^{3N} \left| M_{ij} \right|$ and L_{ii}>0, Therefore, the inverse of matrix $\boldsymbol{L}$ can be written as $\boldsymbol{L}^{-1}$, and the determinant of matrix $\boldsymbol{L}$ can be represented by $|\boldsymbol{L}|$, and $|\boldsymbol{L}| > 0$ [101].

3.2.2 The relationship between phase currents and phase voltages in multi three-phase machines

This section is focused on analyzing the relationship between phase currents and phase voltages of multi three-phase machines without phase displacements among different sub three-phase systems, which is shown in Figure 3-4. The relationship between phase currents and phase voltages with arbitrary phase displacements among different sub three-phase systems is analyzed in Section 3.3.

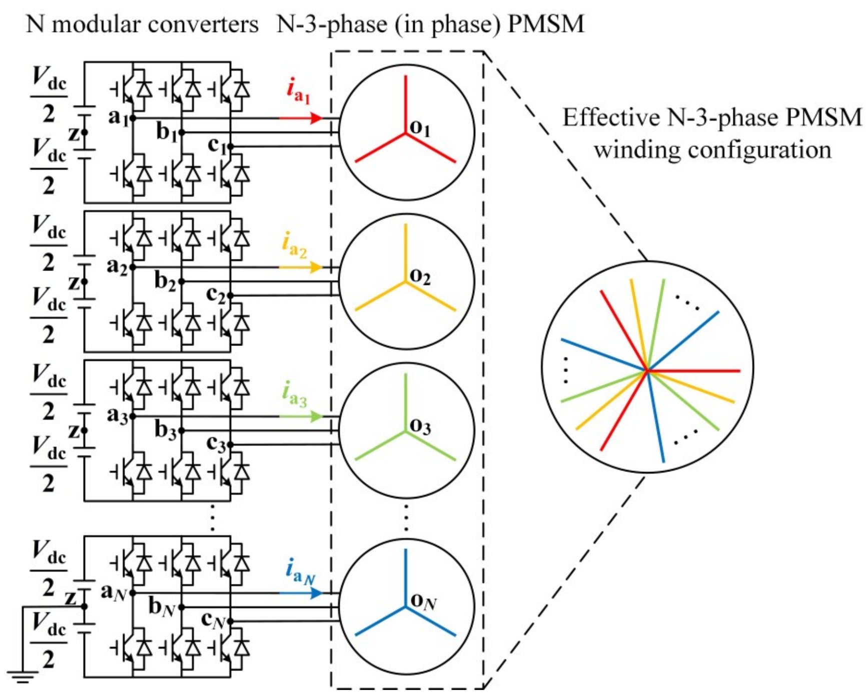

Figure 3-4: *N* three-phase drive system without phase displacements among different sub three-phase systems

The phase voltage is voltage drop between terminals a_1, b_1, c_1, …, a_N, b_N, c_N and terminal o_1, …, o_N which can be represented by u_{a_1}, u_{b_1}, u_{c_1}, …, u_{a_N}, u_{b_N}, u_{c_N} respectively. The phase current is the current flowing through phase a_1, b_1, c_1, …, a_N, b_N,

c_N, which can be represented by i_{a_1}, i_{b_1}, i_{c_1}, …, i_{a_N}, i_{b_N}, i_{c_N} respectively. The back-emf generated on each phase is represented by e_{a_1}, e_{b_1}, e_{c_1}, …, e_{a_N}, e_{b_N}, e_{c_N} respectively. According to the electric principle, the phase voltage matrix is represented by (3-18):

$$\begin{bmatrix} u_{\mathrm{a}_1} \\ u_{\mathrm{b}_1} \\ u_{\mathrm{c}_1} \\ \vdots \\ u_{\mathrm{a}_N} \\ u_{\mathrm{b}_N} \\ u_{\mathrm{c}_N} \end{bmatrix} = \begin{bmatrix} L_{\mathrm{a}_1\mathrm{a}_1} & M_{\mathrm{a}_1\mathrm{b}_1} & M_{\mathrm{a}_1\mathrm{c}_1} & & M_{\mathrm{a}_1\mathrm{a}_N} & M_{\mathrm{a}_1\mathrm{b}_N} & M_{\mathrm{a}_1\mathrm{c}_N} \\ M_{\mathrm{b}_1\mathrm{a}_1} & L_{\mathrm{b}_1\mathrm{b}_1} & M_{\mathrm{b}_1\mathrm{c}_1} & \cdots & M_{\mathrm{b}_1\mathrm{a}_N} & M_{\mathrm{b}_1\mathrm{b}_N} & M_{\mathrm{b}_1\mathrm{c}_N} \\ M_{\mathrm{c}_1\mathrm{a}_1} & M_{\mathrm{c}_1\mathrm{b}_1} & L_{\mathrm{c}_1\mathrm{c}_1} & & M_{\mathrm{c}_1\mathrm{a}_N} & M_{\mathrm{c}_1\mathrm{b}_N} & M_{\mathrm{c}_1\mathrm{c}_N} \\ & \vdots & & \ddots & & \vdots & \\ M_{\mathrm{a}_N\mathrm{a}_1} & M_{\mathrm{a}_N\mathrm{b}_1} & M_{\mathrm{a}_N\mathrm{c}_1} & & L_{\mathrm{a}_N\mathrm{a}_N} & M_{\mathrm{a}_N\mathrm{b}_N} & M_{\mathrm{a}_N\mathrm{c}_N} \\ M_{\mathrm{b}_N\mathrm{a}_1} & M_{\mathrm{b}_N\mathrm{b}_1} & M_{\mathrm{b}_N\mathrm{c}_1} & \cdots & M_{\mathrm{b}_N\mathrm{a}_N} & L_{\mathrm{b}_N\mathrm{b}_N} & M_{\mathrm{b}_N\mathrm{c}_N} \\ M_{\mathrm{c}_N\mathrm{a}_1} & M_{\mathrm{c}_N\mathrm{b}_1} & M_{\mathrm{c}_N\mathrm{c}_1} & & M_{\mathrm{c}_N\mathrm{a}_N} & M_{\mathrm{c}_N\mathrm{b}_N} & L_{\mathrm{c}_N\mathrm{c}_N} \end{bmatrix} \frac{d}{dt} \begin{bmatrix} i_{\mathrm{a}_1} \\ i_{\mathrm{b}_1} \\ i_{\mathrm{c}_1} \\ \vdots \\ i_{\mathrm{a}_N} \\ i_{\mathrm{b}_N} \\ i_{\mathrm{c}_N} \end{bmatrix} + R \begin{bmatrix} i_{\mathrm{a}_1} \\ i_{\mathrm{b}_1} \\ i_{\mathrm{c}_1} \\ \vdots \\ i_{\mathrm{a}_N} \\ i_{\mathrm{b}_N} \\ i_{\mathrm{c}_N} \end{bmatrix} + \begin{bmatrix} e_{\mathrm{a}_1} \\ e_{\mathrm{b}_1} \\ e_{\mathrm{c}_1} \\ \vdots \\ e_{\mathrm{a}_N} \\ e_{\mathrm{b}_N} \\ e_{\mathrm{c}_N} \end{bmatrix}, \tag{3-18}$$

simplified as:

$$\boldsymbol{U} = \boldsymbol{L}\frac{d\,\boldsymbol{I}}{dt} + R\boldsymbol{I} + \boldsymbol{E} \tag{3-19}$$

with:

$$\boldsymbol{U} = \begin{bmatrix} u_{\mathrm{a}_1} \\ u_{\mathrm{b}_1} \\ u_{\mathrm{c}_1} \\ \vdots \\ u_{\mathrm{a}_N} \\ u_{\mathrm{b}_N} \\ u_{\mathrm{c}_N} \end{bmatrix}, \boldsymbol{I} = \begin{bmatrix} i_{\mathrm{a}_1} \\ i_{\mathrm{b}_1} \\ i_{\mathrm{c}_1} \\ \vdots \\ i_{\mathrm{a}_N} \\ i_{\mathrm{b}_N} \\ i_{\mathrm{c}_N} \end{bmatrix}, \boldsymbol{E} = \begin{bmatrix} e_{\mathrm{a}_1} \\ e_{\mathrm{b}_1} \\ e_{\mathrm{c}_1} \\ \vdots \\ e_{\mathrm{a}_N} \\ e_{\mathrm{b}_N} \\ e_{\mathrm{c}_N} \end{bmatrix}.$$

Due to the symmetrical design principle of machine winding configurations, the matrix inductance table among multi three-phase systems a_1, b_1, c_1, …, a_N, b_N, c_N are identical, which means the inductance matrix $\boldsymbol{L}_{pp} = \boldsymbol{L}_{NN}$, $\boldsymbol{M}_{pq} = \boldsymbol{M}_{p+1,q+1}$, $\boldsymbol{M}_{N,q} = \boldsymbol{M}_{1,q+1}$, where $p \neq q,\ p,q \in \{1,2,\dots,N\}$, and:

$$\boldsymbol{L}_{pp} = \begin{bmatrix} L_{\mathrm{a}_p\mathrm{a}_p} & M_{\mathrm{a}_p\mathrm{b}_p} & M_{\mathrm{a}_p\mathrm{c}_p} \\ M_{\mathrm{b}_p\mathrm{a}_p} & L_{\mathrm{b}_p\mathrm{b}_p} & M_{\mathrm{b}_p\mathrm{c}_p} \\ M_{\mathrm{c}_p\mathrm{a}_p} & M_{\mathrm{c}_p\mathrm{b}_p} & L_{\mathrm{c}_p\mathrm{c}_p} \end{bmatrix}, \boldsymbol{M}_{pq} = \begin{bmatrix} M_{\mathrm{a}_p\mathrm{a}_q} & M_{\mathrm{a}_p\mathrm{b}_q} & M_{\mathrm{a}_p\mathrm{c}_q} \\ M_{\mathrm{b}_p\mathrm{a}_q} & M_{\mathrm{b}_p\mathrm{b}_q} & M_{\mathrm{b}_p\mathrm{c}_q} \\ M_{\mathrm{c}_p\mathrm{a}_q} & M_{\mathrm{c}_p\mathrm{b}_q} & M_{\mathrm{c}_p\mathrm{c}_q} \end{bmatrix}.$$

Additionally, in this section, there is no phase displacements among different three-phase subsystems. Therefore, the back-EMFs generated on each phase are identical with the same magnitudes and phases, which means the back-EMF matrixes $\boldsymbol{E}_p = \boldsymbol{E}_\mathrm{N}$, where $p \in \{1,2, \dots, N\}$, and:

$$\boldsymbol{E}_p = \begin{bmatrix} e_{\mathrm{a}_p} \\ e_{\mathrm{b}_p} \\ e_{\mathrm{c}_p} \end{bmatrix}, \boldsymbol{E}_N = \begin{bmatrix} e_{\mathrm{a}_N} \\ e_{\mathrm{b}_N} \\ e_{\mathrm{c}_N} \end{bmatrix}.$$

According to operational properties of matrices, (3-18) can be rewritten as:

$$\begin{bmatrix} u_{\mathrm{a,T}} \\ u_{\mathrm{b,T}} \\ u_{\mathrm{c,T}} \end{bmatrix} = \begin{bmatrix} L_{\mathrm{aa,T}} & M_{\mathrm{ab,T}} & M_{\mathrm{ac,T}} \\ M_{\mathrm{ba,T}} & L_{\mathrm{bb,T}} & M_{\mathrm{bc,T}} \\ M_{\mathrm{ca,T}} & M_{\mathrm{cb,T}} & L_{\mathrm{cc,T}} \end{bmatrix} \frac{d}{dt} \begin{bmatrix} i_{\mathrm{a,T}} \\ i_{\mathrm{b,T}} \\ i_{\mathrm{c,T}} \end{bmatrix} + R \begin{bmatrix} i_{\mathrm{a,T}} \\ i_{\mathrm{b,T}} \\ i_{\mathrm{c,T}} \end{bmatrix} + \begin{bmatrix} e_{\mathrm{a,T}} \\ e_{\mathrm{b,T}} \\ e_{\mathrm{c,T}} \end{bmatrix}, \tag{3-20}$$

simplified as:

$$\boldsymbol{U}_\mathrm{T} = \boldsymbol{L}_\mathrm{T} \frac{d\,\boldsymbol{I}_T}{dt} + R\boldsymbol{I}_\mathrm{T} + \boldsymbol{E}_\mathrm{T}, \tag{3-21}$$

with:

$$\boldsymbol{U}_\mathrm{T} = \begin{bmatrix} u_{\mathrm{a,T}} \\ u_{\mathrm{b,T}} \\ u_{\mathrm{c,T}} \end{bmatrix}, \boldsymbol{L}_\mathrm{T} = \begin{bmatrix} L_{\mathrm{aa,T}} & M_{\mathrm{ab,T}} & M_{\mathrm{ac,T}} \\ M_{\mathrm{ba,T}} & L_{\mathrm{bb,T}} & M_{\mathrm{bc,T}} \\ M_{\mathrm{ca,T}} & M_{\mathrm{cb,T}} & L_{\mathrm{cc,T}} \end{bmatrix}, \boldsymbol{I}_\mathrm{T} = \begin{bmatrix} i_{\mathrm{a,T}} \\ i_{\mathrm{b,T}} \\ i_{\mathrm{c,T}} \end{bmatrix}, \boldsymbol{E}_\mathrm{T} = \begin{bmatrix} e_{\mathrm{a,T}} \\ e_{\mathrm{b,T}} \\ e_{\mathrm{c,T}} \end{bmatrix}.$$

where $\boldsymbol{U}_\mathrm{T}$ is the total equivalent voltage; $\boldsymbol{I}_\mathrm{T}$ is the total equivalent current; $\boldsymbol{E}_\mathrm{T}$ is the total equivalent back-emf; $\boldsymbol{L}_\mathrm{T}$ is the total equivalent inductance.

According to (3-21), by using Laplace formula, neglecting the initial conditions, $\boldsymbol{U}_\mathrm{T}$ can be represented as:

$$\boldsymbol{U}_\mathrm{T} = (s\boldsymbol{L}_\mathrm{T} + R)\boldsymbol{I}_\mathrm{T} + \boldsymbol{E}_\mathrm{T} \tag{3-22}$$

Neglecting the harmonics caused by cogging effect and the shape permanent magnet, the back-EMF is considered to be ideal sinusoidal. Therefore, for $\boldsymbol{U}_{\mathrm{T}}$ and $\boldsymbol{I}_{\mathrm{T}}$, only the fundamental component, and the harmonic components which are generated by PWM modulation effect are considered. According to (3-22), the total equivalent fundamental voltage $\boldsymbol{U}_{\mathrm{f}}$, the total equivalent fundamental current $\boldsymbol{I}_{\mathrm{f}}$, the total equivalent harmonic voltage $\boldsymbol{U}_{\mathrm{h}}$ and the total equivalent harmonic current $\boldsymbol{I}_{\mathrm{h}}$ can be represented as:

$$\left.\begin{array}{c} \boldsymbol{U}_{\mathrm{T}} = \boldsymbol{U}_{\mathrm{f}} + \boldsymbol{U}_{\mathrm{h}} \\ \boldsymbol{I}_{\mathrm{T}} = \boldsymbol{I}_{\mathrm{f}} + \boldsymbol{I}_{\mathrm{h}} \\ \boldsymbol{U}_{\mathrm{f}} = (s\boldsymbol{L}_{\mathrm{T}} + R)\boldsymbol{I}_{\mathrm{f}} + \boldsymbol{E}_{\mathrm{T}} \\ \boldsymbol{U}_{\mathrm{h}} = (s\boldsymbol{L}_{\mathrm{T}} + R)\boldsymbol{I}_{\mathrm{h}} \end{array}\right\} , \tag{3-23}$$

with:

$$\boldsymbol{U}_{\mathrm{f}} = \begin{bmatrix} u_{\mathrm{a,f}} \\ u_{\mathrm{b,f}} \\ u_{\mathrm{c,f}} \end{bmatrix}, \boldsymbol{I}_{\mathrm{f}} = \begin{bmatrix} i_{\mathrm{a,f}} \\ i_{\mathrm{b,f}} \\ i_{\mathrm{c,f}} \end{bmatrix}, \boldsymbol{U}_{\mathrm{h}} = \begin{bmatrix} u_{\mathrm{a,h}} \\ u_{\mathrm{b,h}} \\ u_{\mathrm{c,h}} \end{bmatrix}, \boldsymbol{I}_{\mathrm{f}} = \begin{bmatrix} i_{\mathrm{a,h}} \\ i_{\mathrm{b,h}} \\ i_{\mathrm{c,h}} \end{bmatrix}.$$

According to (3-23), by using Laplace formula, neglecting the initial conditions, $\boldsymbol{U}_{\mathrm{h}}$ can be represented as:

$$\boldsymbol{U}_{\mathrm{h}} = \boldsymbol{A}(s)\boldsymbol{I}_{\mathrm{h}}, \tag{3-24}$$

with:

$$\boldsymbol{A}(s) = (s\boldsymbol{L}_{\mathrm{T}} + R) = \begin{bmatrix} sL_{\mathrm{aa,T}} + R & sM_{\mathrm{ab,T}} & sM_{\mathrm{ac,T}} \\ sM_{\mathrm{ba,T}} & sL_{\mathrm{bb,T}} + R & sM_{\mathrm{bc,T}} \\ sM_{\mathrm{ca,T}} & sM_{\mathrm{cb,T}} & sL_{\mathrm{cc,T}} + R \end{bmatrix}. \tag{3-25}$$

According to (3-23), $\boldsymbol{I}_{\mathrm{h}}$ can be represented as:

$$\boldsymbol{I}_{\mathrm{h}} = \boldsymbol{B}(s)\boldsymbol{U}_{\mathrm{h}}, \tag{3-26}$$

where $\boldsymbol{B}(s)$ is the inverse of matrix $\boldsymbol{A}(s)$, and $\boldsymbol{B}(s)$ can be represented as:

$$\boldsymbol{B}(s) = \frac{1}{|\boldsymbol{A}(s)|} adj(\boldsymbol{A}(s)), \tag{3-27}$$

with:

$$|\boldsymbol{A}(s)| = (sL_{\text{aa,T}} + R)(sL_{\text{bb,T}} + R)(sL_{\text{cc,T}} + R) - s^2(sL_{\text{aa,T}} + R)M_{\text{bc,T}}^2$$

$$-s^2(sL_{\text{bb,T}} + R)M_{\text{ac,T}}^2 - s^2(sL_{\text{cc,T}} + R)M_{\text{ab,T}}^2 + 2s^3 M_{\text{ab,T}} M_{\text{ac,T}} M_{\text{bc,T}},$$

$$adj(\boldsymbol{A}(s))$$

$$= \begin{bmatrix} (sL_{\text{bb,T}} + R)(sL_{\text{cc,T}} + R) - s^2 M_{\text{bc,T}}^2 & -s(sL_{\text{cc,T}} + R)M_{\text{ab,T}} + s^2 M_{\text{ac,T}} M_{\text{bc,T}} & -s(sL_{\text{bb,T}} + R)M_{\text{ac,T}} + s^2 M_{\text{ab,T}} M_{\text{bc,T}} \\ -s(sL_{\text{cc,T}} + R)M_{\text{ab,T}} + s^2 M_{\text{ac,T}} M_{\text{bc,T}} & (sL_{\text{aa,T}} + R)(sL_{\text{cc,T}} + R) - s^2 M_{\text{ac,T}}^2 & -s(sL_{\text{aa,T}} + R)M_{\text{bc,T}} + s^2 M_{\text{ab,T}} M_{\text{ac,T}} \\ -s(sL_{\text{bb,T}} + R)M_{\text{ac,T}} + s^2 M_{\text{ab,T}} M_{\text{bc,T}} & -s(sL_{\text{aa,T}} + R)M_{\text{bc,T}} + s^2 M_{\text{ab,T}} M_{\text{ac,T}} & (sL_{\text{aa,T}} + R)(sL_{\text{bb,T}} + R) - s^2 M_{\text{ab,T}}^2 \end{bmatrix}.$$

According to (3-25), $\boldsymbol{B}(s)$ can be alternatively represented as:

$$\boldsymbol{B}(s) = \begin{bmatrix} B_1(s) & B_2(s) & B_3(s) \\ B_2(s) & B_4(s) & B_5(s) \\ B_3(s) & B_5(s) & B_6(s) \end{bmatrix},$$

with:

$$B_1(s) = \frac{(sL_{\text{bb,T}}+R)(sL_{\text{cc,T}}+R)-s^2 M_{\text{bc,T}}^2}{|\boldsymbol{A}(s)|},$$

$$B_2(s) = \frac{-s(sL_{\text{cc,T}}+R)M_{\text{ab,T}}+s^2 M_{\text{ac,T}} M_{\text{bc,T}}}{|\boldsymbol{A}(s)|},$$

$$B_3(s) = \frac{-s(sL_{\text{bb,T}}+R)M_{\text{ac,T}}+s^2 M_{\text{ab,T}} M_{\text{bc,T}}}{|\boldsymbol{A}(s)|},$$

$$B_4(s) = \frac{(sL_{\text{aa,T}}+R)(sL_{\text{cc,T}}+R)-s^2 M_{\text{ac,T}}^2}{|\boldsymbol{A}(s)|},$$

$$B_5(s) = \frac{-s(sL_{\text{aa,T}}+R)M_{\text{bc,T}}+s^2 M_{\text{ab,T}} M_{\text{ac,T}}}{|\boldsymbol{A}(s)|},$$

$$B_6(s) = \frac{(sL_{\mathrm{aa,T}}+R)(sL_{\mathrm{bb,T}}+R)-s^2M_{\mathrm{ab,T}}^2}{|\boldsymbol{A}(s)|},$$

$$|\boldsymbol{A}(s)| = (sL_{\mathrm{aa,T}}+R)(sL_{\mathrm{bb,T}}+R)(sL_{\mathrm{cc,T}}+R) - s^2(sL_{\mathrm{aa,T}}+R)M_{\mathrm{bc,T}}^2 -$$

$$s^2(sL_{\mathrm{bb,T}}+R)M_{\mathrm{ac,T}}^2 - s^2(sL_{\mathrm{cc,T}}+R)M_{\mathrm{ab,T}}^2 + 2s^3M_{\mathrm{ab,T}}M_{\mathrm{ac,T}}M_{\mathrm{bc,T}}.$$

It can be seen that the all the elements in the matrix $\boldsymbol{B}(s)$ including $B_1(s)$, $B_2(s)$, $B_3(s)$, $B_4(s)$, $B_5(s)$, $B_6(s)$ can be represented by $B_l(s)$:

$$B_l(s) = \frac{C_{1l}s^2+C_{2l}s+C_{3l}}{C_{4l}s^3+C_{5l}s^2+C_{6l}s+C_{7l}},$$

where $l \in \{1,2,3,4,5,6\}$; $C_{1l}, C_{2l}, C_{3l}, C_{4l}, C_{5l}, C_{6l}, C_{7l}$ are constants for any value of l. Therefore, referring to the formula of $B_l(s)$, it can be seen that $B_1(s)$, $B_2(s)$, $B_3(s)$, $B_4(s)$, $B_5(s)$, $B_6(s)$ are low-pass filters.

According to the (3-25), the relationship between the total equivalent harmonic current $i_{\mathrm{a,h}}, i_{\mathrm{b,h}}, i_{\mathrm{c,h}}$ and the total equivalent harmonic voltage $u_{\mathrm{a,h}}, u_{\mathrm{b,h}}, u_{\mathrm{c,h}}$ can be represented as:

$$\begin{bmatrix} i_{\mathrm{a,h}} \\ i_{\mathrm{b,h}} \\ i_{\mathrm{c,h}} \end{bmatrix} = \begin{bmatrix} B_1(s) & B_2(s) & B_3(s) \\ B_2(s) & B_4(s) & B_5(s) \\ B_3(s) & B_5(s) & B_6(s) \end{bmatrix} \begin{bmatrix} u_{\mathrm{a,h}} \\ u_{\mathrm{b,h}} \\ u_{\mathrm{c,h}} \end{bmatrix} \tag{3-28}$$

Referring to the operational properties of matrix, hence $i_{\mathrm{a,h}}$, $i_{\mathrm{b,h}}$, $i_{\mathrm{c,h}}$ can be represented as:

$$\begin{cases} i_{\mathrm{a,h}} = B_1(s)u_{\mathrm{a,h}} + B_2(s)u_{\mathrm{b,h}} + B_3(s)u_{\mathrm{c,h}} \\ i_{\mathrm{b,h}} = B_2(s)u_{\mathrm{a,h}} + B_4(s)u_{\mathrm{b,h}} + B_5(s)u_{\mathrm{c,h}} \\ i_{\mathrm{c,h}} = B_3(s)u_{\mathrm{a,h}} + B_5(s)u_{\mathrm{b,h}} + B_6(s)u_{\mathrm{c,h}} \end{cases}. \tag{3-29}$$

According to (3-29), the total equivalent harmonic currents $i_{\mathrm{a,h}}$, $i_{\mathrm{b,h}}$, $i_{\mathrm{c,h}}$ are considered to be generated by the total equivalent harmonic voltages $u_{\mathrm{a,h}}$, $u_{\mathrm{b,h}}$, $u_{\mathrm{c,h}}$ through low-pass filters (i.e. the resistance-inductance network $B_l(s)$). The cancellation of phase voltage harmonic components may result in the cancellation of phase current harmonic components. The next sub-chapter will show that the major torque ripple is caused by the total equivalent harmonic currents. Thus, the working principle of the proposed torque ripple reduction method is based on the cancellation of total equivalent harmonic voltage harmonic voltages.

Considering the low pass filter effect of the relationship between total equivalent harmonic voltage and current, and more harmfulness of lower order harmonics in electric machine systems, the lower order harmonic voltage is of first importance to be eliminated.

3.2.3 Analytical matrix torque equations in multi three-phase machines

The electromagnetic torque can be represented by:

$$T_\mathrm{e} = \frac{1}{\omega_\mathrm{m}} \boldsymbol{I}^\mathrm{T} \cdot \boldsymbol{E} = \frac{1}{\omega_\mathrm{m}} \begin{bmatrix} i_{\mathrm{a}_1} & i_{\mathrm{b}_1} & i_{\mathrm{c}_1} \cdots i_{\mathrm{a}_N} & i_{\mathrm{b}_N} & i_{\mathrm{c}_N} \end{bmatrix} \begin{bmatrix} e_{\mathrm{a}_1} \\ e_{\mathrm{b}_1} \\ e_{\mathrm{c}_1} \\ \vdots \\ e_{\mathrm{a}_N} \\ e_{\mathrm{b}_N} \\ e_{\mathrm{c}_N} \end{bmatrix}, \tag{3-30}$$

where ω_m is the mechanical speed of the machine.

Since $\boldsymbol{E}_p = \boldsymbol{E}_\mathrm{N}$ for $p \in \{1,2,\dots,N\}$, (3-30) can be rewritten as:

$$T_\mathrm{e} = \frac{1}{\omega_\mathrm{m}} \begin{bmatrix} i_{\mathrm{a,T}} & i_{\mathrm{b,T}} & i_{\mathrm{c,T}} \end{bmatrix} \begin{bmatrix} e_{\mathrm{a}_N} \\ e_{\mathrm{b}_N} \\ e_{\mathrm{c}_N} \end{bmatrix}. \tag{3-31}$$

According to (3-31), the electromagnetic torque ripple can be represented as:

$$T_{\mathrm{e,h}} = \frac{1}{\omega_{\mathrm{m}}}\begin{bmatrix} i_{\mathrm{a,h}} & i_{\mathrm{b,h}} & i_{\mathrm{c,h}} \end{bmatrix}\begin{bmatrix} e_{\mathrm{a}_N} \\ e_{\mathrm{b}_N} \\ e_{\mathrm{c}_N} \end{bmatrix} \tag{3-32}$$

According to (3-32), as only the fundamental component of the back-EMF is considered, the torque ripple is related to the total equivalent harmonic current $i_{\mathrm{a,h}}, i_{\mathrm{b,h}}, i_{\mathrm{c,h}}$. As it has been discussed in the Section 3.2.2 that the cancellation of phase voltage harmonic components may result in the cancellation of current harmonic components. Therefore, the working principle of the proposed torque ripple reduction method is based on the cancellation of total equivalent harmonic voltages.

3.3 Analytical torque equations of multi three-phase machines by voltage and current space vectors

This section is focused on analyzing the torque ripple equations of multi three-phase machines with arbitrary phase displacements among different sub three-phase systems by using current and voltage space vectors, which is shown in Figure 3-5.

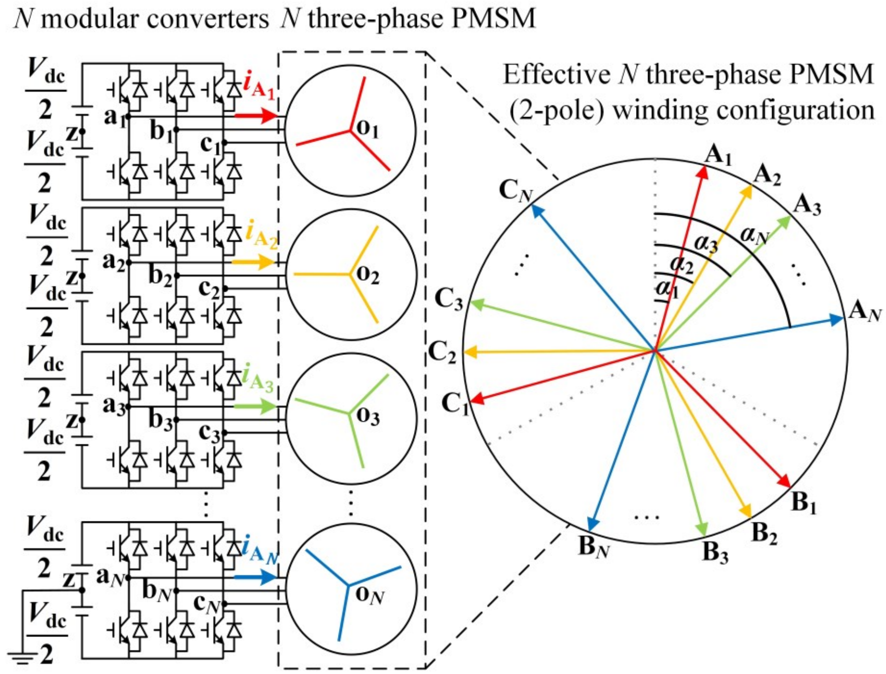

Figure 3-5: *N* three-phase drive system without phase displacements among different sub three-phase systems [102]

As it is shown in Figure 3-5, in a equivalent 2-pole space winding structure of the N three-phase systems, the space shift angles between p^{th}, $p \in \{1, .., N\}$ three-phase system and the stator reference frame are represented by α_1, …, α_N respectively. The phase voltage is the voltage drop between the terminals a_1, b_1, c_1, …, a_N, b_N, c_N and the terminals o_1, …,

o_N, and are named as u_{a_1}, u_{b_1}, u_{c_1}, …, u_{a_N}, u_{b_N}, u_{c_N} respectively. The equivalent phase voltage space vector of the p^{th} ($p \in \{1,..,N\}$) three-phase subsystem $\vec{u}_p(t)$ can be represented as:

$$\vec{u}_p(t) = \frac{2}{3}[u_{a_p}(t)e^{j\alpha_p} + u_{b_p}(t)e^{j(\alpha_p+\frac{2}{3}\pi)} + u_{c_p}(t)e^{j(\alpha_p-\frac{2}{3}\pi)}], \tag{3-33}$$

where α_p is the space phase shift angle between the p^{th} three-phase system and the reference frame. The total equivalent phase space vector of N three-phase subsystems $\vec{u}_{\text{total}}(t)$ can be represented as:

$$\vec{u}_{\text{total}}(t) = \frac{1}{N}[\vec{u}_1(t)e^{j\alpha_1} + \vec{u}_2(t)e^{j\alpha_2} + \vec{u}_3(t)e^{j\alpha_3} + \cdots + \vec{u}_N(t)e^{j\alpha_N}]. \tag{3-34}$$

Substituting (3-33) into (3-34), the total equivalent phase voltage space vector $\vec{u}_{\text{total}}(t)$ can be represented as:

$$\vec{u}_{\text{total}}(t) = \frac{2}{3N}\sum_{p=1}^{N}[u_{a_p}(t)e^{j\alpha_p} + u_{b_p}(t)e^{j(\alpha_p+\frac{2}{3}\pi)} + u_{c_p}(t)e^{j(\alpha_p-\frac{2}{3}\pi)}]. \tag{3-35}$$

The back-EMFs generated on each phase are represented by e_{a_1}, e_{b_1}, e_{c_1}, …, e_{a_N}, e_{b_N}, e_{c_N} respectively. Similarly, the total equivalent back-EMF space vector $\vec{e}_{\text{total}}(t)$ of N three-phase subsystems can be represented as:

$$\vec{e}_{\text{total}}(t) = \frac{2}{3N}\sum_{p=1}^{N}[e_{a_p}(t)e^{j\alpha_p} + e_{b_p}(t)e^{j(\alpha_p+\frac{2}{3}\pi)} + e_{c_p}(t)e^{j(\alpha_p-\frac{2}{3}\pi)}]. \tag{3-36}$$

The phase current is the current flowing through phase A_1, B_1, C_1, …, A_N, B_N, C_N, which are represented by i_{a_1}, i_{b_1}, i_{c_1}, …, i_{a_N}, i_{b_N}, i_{c_N} respectively. The total equivalent phase current space vector of N three-phase systems $\vec{i}_{total}(t)$ can be represented as:

$$\vec{i}_{\text{total}}(t) = \frac{2}{3N}\sum_{p=1}^{N}[i_{a_p}(t)e^{j\alpha_p} + i_{b_p}(t)e^{j(\alpha_p+\frac{2}{3}\pi)} + i_{c_p}(t)e^{j(\alpha_p-\frac{2}{3}\pi)}]. \tag{3-37}$$

The instantaneous electromagnetic torque generated by the p^{th} three-phase subsystem can be written as:

$$T_p(t) = \frac{1}{\omega_m}[i_{\mathrm{a}_p}(t)e_{\mathrm{a}_p}(t) + i_{\mathrm{b}_p}(t)e_{\mathrm{b}_p}(t) + i_{\mathrm{c}_p}(t)e_{\mathrm{c}_p}(t)]$$
$$= \frac{3}{2\omega_m}[\, \vec{\imath}_p(t) \cdot \vec{e}_p(t)], \tag{3-38}$$

where ω_m is the mechanical speed of the machine.

The total instantaneous electromagnetic torque generated by N three-phase subsystems can be written as:

$$T_{total}(t) = \frac{3N}{2\omega_m}[\, \vec{\imath}_{total}(t) \cdot \vec{e}_{total}(t)]. \tag{3-39}$$

3.4 The machines in this thesis

This work aimed at designing a novel drive system for marine application. The proposed machine designed for marine propulsion is shown in Section 3.5. It is a 48-slot, 8-pole non-salient PMSM with the rated power of 2MW and rated speed of 20000rpm. The parameters of the 2MW PMSM are listed in Table 3-1. There are two potential winding configurations of the 2MW PMSM with either configured as an eight three-phase distributed machine or an eight three-phase sectored machine, which are shown in Figure 3-7 and Figure 3-8. The analytical inductance values of distributed and sectored configurations are presented and validated by FEA results in Section 3.5.

Due to the challenges of building a 2MW drive system directly, different scaled-down machines are built to validate the machine performance and the control algorithms respectively. Firstly, a scaled-down dual three-phase PMSM with the rated power of 160kW and rated speed of 20000rpm was realized, to validate the feasibility of the proposed machine to reach the maximum speed (20000rpm). The parameters of the 160kW PMSM are listed in Table 4-3. The mathematical model of the relevant drive system is validated by simulation results in PLECS in Section 4.4.1.

Secondly, a scaled-down sectored triple three-phase PMSM with the rated power of 1.5kW, and a distributed dual three-phase PMSM with rated power of 18kW have been used to test the proposed control algorithm of multi three-phase drive. The simulation results of the sectored triple three-phase PMSM are shown in Section 4.4.1 and Section 5.3.1, which are validated by the experimental results in Section 4.5.1 and Section 5.4.1. The simulation results of the distributed dual three-phase PMSM are shown in Section 4.4.2 and Section 5.3.2, which are validated by the experimental results in Section 4.5.2 and Section 5.4.2.

3.5 Simulation results

This section shows the simulation results of machine inductances from FEA (Finite Element Analysis) model in Maxwell and analytical models shown in Section 3.2.1. Figure 3-6 shows a 2MW non-salient PMSM machine model in Maxwell which is designed for the marine propulsion. It is a 48-slot, 8-pole double layer non-salient PMSM with rated speed of 20000rpm. The parameters of the machine are listed in Table 3-1.

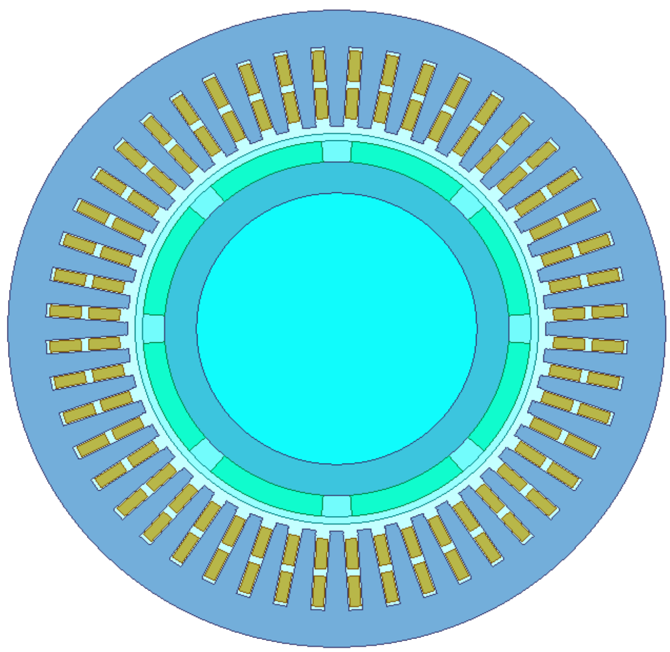

Figure 3-6: 2MW machine model in Maxwell

Figure 3-7 and Figure 3-8 show the machine windings of distributed construction and sectored configuration respectively. Both constructions have 8 three-phase subsystems. Distributed construction has the advantage of balanced mutual effect among three phases in each subsystem, while it has strong mutual coupling effect among different three-phase subsystems. Sectored construction has the advantage of weak mutual coupling effect among different three-phase subsystems, while it has unbalanced mutual effect in each subsystem. Therefore, it is of importance to compare the mutual coupling effect between distributed construction and sectored construction.

Parameter	**Value**
DC link Voltage	500 [V]
Fundamental frequency	1333.33 [Hz]
Pole pair number	4
Rated phase current (RMS)	550 [A]
Phase resistance	0.9 [mΩ]
Back-EMF coefficient	0.073 (Phase rms back-EMF is 152.26V at 1333.33Hz)
Pitch factor	5/6
Number of turns per phase	2
Stator length	0.233 [m]
Stator inner radius	0.137 [m]
Air gap length	0.033 [m]
Self inductance of phase A1, B1, C1,…, A8, B8, C8	$L_{\mathrm{a1}} = L_{\mathrm{b1}} = L_{\mathrm{c1}} = \ldots = L_{\mathrm{a8}} = L_{\mathrm{b8}} = L_{\mathrm{c8}}$ =12μH

Table 3-1: Parameters of 2MW PMSM for Marine propulsion

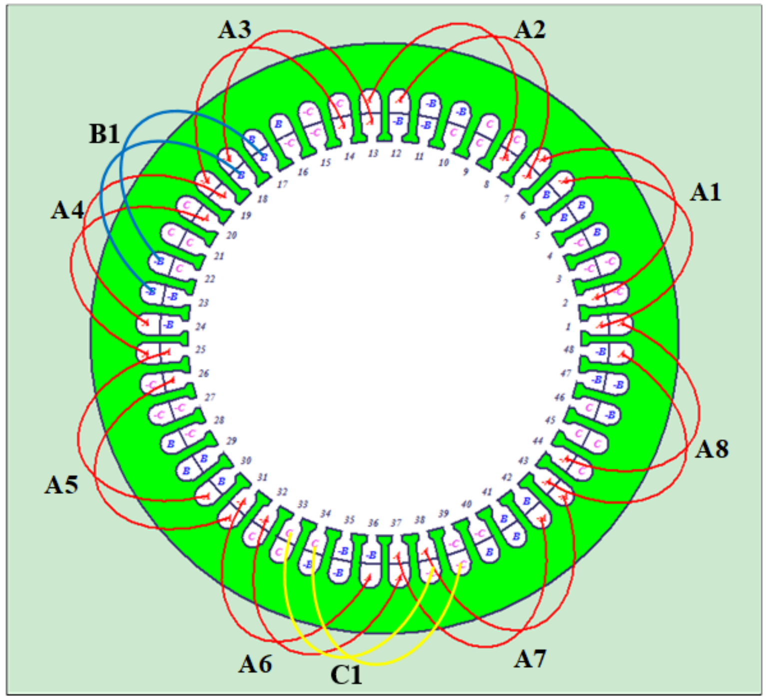

Figure 3-7: 2MW machine of distributed winding construction

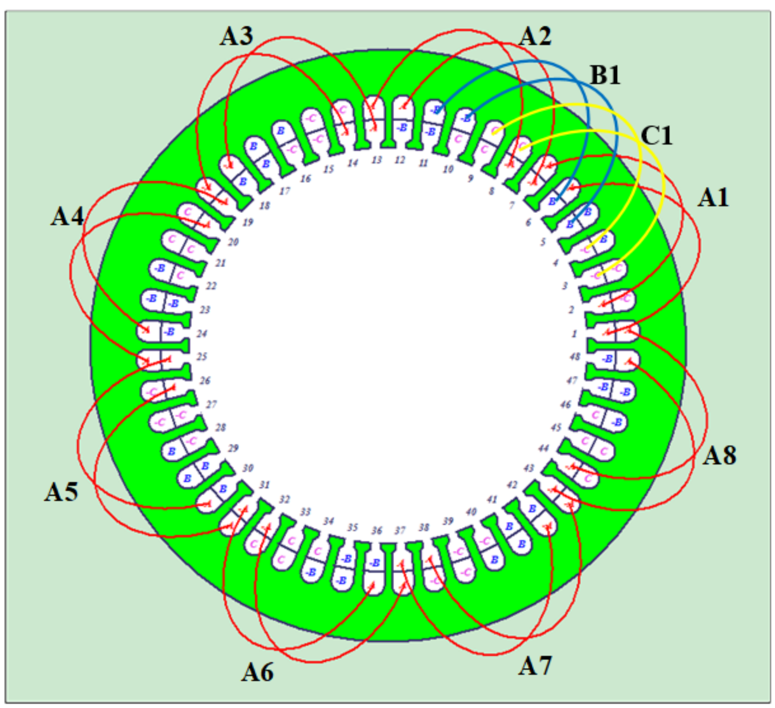

Figure 3-8: 2MW machine of sectored winding construction

Table 3-2 and Table 3-4 show the inductance matrixes of FEA (Finite Element Analysis) results based on the Maxwell machine model shown in Figure 3-6 in distributed winding construction (Figure 3-7) and sectored winding construction (Figure 3-8) respectively. The Maxwell machine model is working at rated power (RMS phase current at 550A and speed at 20000rpm). Table 3-3 and Table 3-5 show the inductance matrices of analytical results based on (3-9) and (3-17) with machine parameters shown in Table 3-1 in distributed winding construction (Figure 3-7) and sectored winding construction (Figure 3-8) respectively. The corresponding MATLAB code to generate the analytical inductance matrix values are shown in Appendix A.

Comparing Table 3-2 (Table 3-4) with Table 3-3 (Table 3-5), the analytical results matches with the FEA results in general. The differences between values in Table 3-2 (Table 3-4) and Table 3-3 (Table 3-5) are mainly due to two reasons. The first reason is the parameter uncertainties in the model, related to uncertainties in the machine parameters including the changes of them with working operation because of saturations and non-linear effects. Secondly, as it has been mentioned in Section 3.1, the analytical inductance values are obtained by the air-gap flux linkage, which means the self and mutual flux leakage are not considered in the analytical equations, which will also result in the difference between analytical result and FEA result.

Comparing Table 3-3 and Table 3-5, distributed winding construction and sectored winding construction have different mutual coupling effects. For the distributed winding construction, the machine is $M_{a_1\mathrm{b}_1}= M_{\mathrm{a}_1\mathrm{c}_1}= \ldots = M_{c_N a_N}$=$M_{c_N b_N}$=1.3μH. Therefore, the machine has balanced mutual coupling effect in each three-phase subsystem. For the sectored winding construction, the machine has weak mutual coupling effect with the other three-phase subsystems. For example, the subsystems $A_1B_1C_1$ and $A_2B_2C_2$ have weak mutual coupling with the subsystems $A_1B_1C_1$, $A_2B_2C_2$, $A_3B_3C_3$, $A_4B_4C_4$, $A_5B_5C_5$, $A_6B_6C_6$. Therefore, the sectored winding construction has less effect on other subsystems while different control techniques applied to different subsystems (i.e. different PWM carrier phase angles is applied to different subsystems).

It is of importance to analyze the different mutual coupling effect between the distributed and the sectored winding configurations, as the two winding configurations have different advantages with different applications. The effects on the current ripple introduced by the PWM related torque ripple reduction method, is analyzed with two case studies of one triple three-phase sectored machine and one distributed dual three-phase machine in Chapter 5.

	A1	A2	A3	A4	A5	A6	A7	A8	B1	B2	B3	B4	B5	B6	B7	B8	C1	C2	C3	C4	C5	C6	C7	C8
A1	12.1	1.9	-0.7	0.7	-0.7	0.7	-0.7	1.9	-0.7	0.7	-0.7	0.7	-0.7	-3.5	-0.5	0.7	-0.7	0.7	-0.5	-3.5	-0.7	0.7	-0.7	0.7
A2	1.9	12.1	1.9	-0.7	0.7	-0.7	0.7	-0.7	0.7	-0.7	0.7	-0.7	0.7	-0.7	-3.5	-0.5	0.7	-0.7	0.7	-0.5	-3.5	-0.7	0.7	-0.7
A3	-0.7	1.9	12.1	1.9	-0.7	0.7	-0.7	0.7	-0.5	0.7	-0.7	0.7	-0.7	0.7	-0.7	-3.5	-0.7	0.7	-0.7	0.7	-0.5	-3.5	-0.7	0.7
A4	0.7	-0.7	1.9	12.1	1.9	-0.7	0.7	-0.7	-3.5	-0.5	0.7	-0.7	0.7	-0.7	0.7	-0.7	0.7	-0.7	0.7	-0.7	0.7	-0.5	-3.5	-0.7
A5	-0.7	0.7	-0.7	1.9	12.1	1.9	-0.7	0.7	-0.7	-3.5	-0.5	0.7	-0.7	0.7	-0.7	0.7	-0.7	0.7	-0.7	0.7	-0.7	0.7	-0.5	-3.5
A6	0.7	-0.7	0.7	-0.7	1.9	12.1	1.9	-0.7	0.7	-0.7	-3.5	-0.5	0.7	-0.7	0.7	-0.7	-3.5	-0.7	0.7	-0.7	0.7	-0.7	0.7	-0.5
A7	-0.7	0.7	-0.7	0.7	-0.7	1.9	12.1	1.9	-0.7	0.7	-0.7	-3.5	-0.5	0.7	-0.7	0.7	-0.5	-3.5	-0.7	0.7	-0.7	0.7	-0.7	0.7
A8	1.9	-0.7	0.7	-0.7	0.7	-0.7	1.9	12.1	0.7	-0.7	0.7	-0.7	-3.5	-0.5	0.7	-0.7	0.7	-0.5	-3.5	-0.7	0.7	-0.7	0.7	-0.7
B1	-0.7	0.7	-0.5	-3.5	-0.7	0.7	-0.7	0.7	12.1	1.9	-0.7	0.7	-0.7	0.7	-0.7	1.9	-0.7	0.7	-0.7	0.7	-0.7	-3.5	-0.5	0.7
B2	0.7	-0.7	0.7	-0.5	-3.5	-0.7	0.7	-0.7	1.9	12.1	1.9	-0.7	0.7	-0.7	0.7	-0.7	0.7	-0.7	0.7	-0.7	0.7	-0.7	-3.5	-0.5
B3	-0.7	0.7	-0.7	0.7	-0.5	-3.5	-0.7	0.7	-0.7	1.9	12.1	1.9	-0.7	0.7	-0.7	0.7	-0.5	0.7	-0.7	0.7	-0.7	0.7	-0.7	-3.5
B4	0.7	-0.7	0.7	-0.7	0.7	-0.5	-3.5	-0.7	0.7	-0.7	1.9	12.1	1.9	-0.7	0.7	-0.7	-3.5	-0.5	0.7	-0.7	0.7	-0.7	0.7	-0.7
B5	-0.7	0.7	-0.7	0.7	-0.7	0.7	-0.5	-3.5	-0.7	0.7	-0.7	1.9	12.1	1.9	-0.7	0.7	-0.7	-3.5	-0.5	0.7	-0.7	0.7	-0.7	0.7
B6	-3.5	-0.7	0.7	-0.7	0.7	-0.7	0.7	-0.5	0.7	-0.7	0.7	-0.7	1.9	12.1	1.9	-0.7	0.7	-0.7	-3.5	-0.5	0.7	-0.7	0.7	-0.7
B7	-0.5	-3.5	-0.7	0.7	-0.7	0.7	-0.7	0.7	-0.7	0.7	-0.7	0.7	-0.7	1.9	12.1	1.9	-0.7	0.7	-0.7	-3.5	-0.5	0.7	-0.7	0.7
B8	0.7	-0.5	-3.5	-0.7	0.7	-0.7	0.7	-0.7	1.9	-0.7	0.7	-0.7	0.7	-0.7	1.9	12.1	0.7	-0.7	0.7	-0.7	-3.5	-0.5	0.7	-0.7
C1	-0.7	0.7	-0.7	0.7	-0.7	-3.5	-0.5	0.7	-0.7	0.7	-0.5	-3.5	-0.7	0.7	-0.7	0.7	12.1	1.9	-0.7	0.7	-0.7	0.7	-0.7	1.9
C2	0.7	-0.7	0.7	-0.7	0.7	-0.7	-3.5	-0.5	0.7	-0.7	0.7	-0.5	-3.5	-0.7	0.7	-0.7	1.9	12.1	1.9	-0.7	0.7	-0.7	0.7	-0.7
C3	-0.5	0.7	-0.7	0.7	-0.7	0.7	-0.7	-3.5	-0.7	0.7	-0.7	0.7	-0.5	-3.5	-0.7	0.7	-0.7	1.9	12.1	1.9	-0.7	0.7	-0.7	0.7
C4	-3.5	-0.5	0.7	-0.7	0.7	-0.7	0.7	-0.7	0.7	-0.7	0.7	-0.7	0.7	-0.5	-3.5	-0.7	0.7	-0.7	1.9	12.1	1.9	-0.7	0.7	-0.7
C5	-0.7	-3.5	-0.5	0.7	-0.7	0.7	-0.7	0.7	-0.7	0.7	-0.7	0.7	-0.7	0.7	-0.5	-3.5	-0.7	0.7	-0.7	1.9	12.1	1.9	-0.7	0.7
C6	0.7	-0.7	-3.5	-0.5	0.7	-0.7	0.7	-0.7	-3.5	-0.7	0.7	-0.7	0.7	-0.7	0.7	-0.5	0.7	-0.7	0.7	-0.7	1.9	12.1	1.9	-0.7
C7	-0.7	0.7	-0.7	-3.5	-0.5	0.7	-0.7	0.7	-0.5	-3.5	-0.7	0.7	-0.7	0.7	-0.7	0.7	-0.7	0.7	-0.7	0.7	-0.7	1.9	12.0	1.9
C8	0.7	-0.7	0.7	-0.7	-3.5	-0.5	0.7	-0.7	0.7	-0.5	-3.5	-0.7	0.7	-0.7	0.7	-0.7	1.9	-0.7	0.7	-0.7	0.7	-0.7	1.9	12.1

Table 3-2: Inductance (μH) matrix of FEA (Maxwell) result in distributed winding construction

	A1	A2	A3	A4	A5	A6	A7	A8	B1	B2	B3	B4	B5	B6	B7	B8	C1	C2	C3	C4	C5	C6	C7	C8
A1	10.2	1.3	-1.3	1.3	-1.3	1.3	-1.3	1.3	-1.3	1.3	-1.3	1.3	-1.3	-6.4	1.2	1.3	-1.3	1.3	1.2	-6.4	-1.3	1.3	-1.3	1.3
A2	1.3	10.2	1.3	-1.3	1.3	-1.3	1.3	-1.3	1.3	-1.3	1.3	-1.3	1.3	-1.3	-6.4	1.2	1.3	-1.3	1.3	1.2	-6.4	-1.3	1.3	-1.3
A3	-1.3	1.3	10.2	1.3	-1.3	1.3	-1.3	1.3	1.2	1.3	-1.3	1.3	-1.3	1.3	-1.3	-6.4	-1.3	1.3	-1.3	1.3	1.2	-6.4	-1.3	1.3
A4	1.3	-1.3	1.3	10.2	1.3	-1.3	1.3	-1.3	-6.4	1.2	1.3	-1.3	1.3	-1.3	1.3	-1.3	1.3	-1.3	1.3	-1.3	1.3	1.2	-6.4	-1.3
A5	-1.3	1.3	-1.3	1.3	10.2	1.3	-1.3	1.3	-1.3	-6.4	1.2	1.3	-1.3	1.3	-1.3	1.3	-1.3	1.3	-1.3	1.3	-1.3	1.3	1.2	-6.4
A6	1.3	-1.3	1.3	-1.3	1.3	10.2	1.3	-1.3	1.3	-1.3	-6.4	1.2	1.3	-1.3	1.3	-1.3	-6.4	-1.3	1.3	-1.3	1.3	-1.3	1.3	1.2
A7	-1.3	1.3	-1.3	1.3	-1.3	1.3	10.2	1.3	-1.3	1.3	-1.3	-6.4	1.2	1.3	-1.3	1.3	1.2	-6.4	-1.3	1.3	-1.3	1.3	-1.3	1.3
A8	1.3	-1.3	1.3	-1.3	1.3	-1.3	1.3	10.2	1.3	-1.3	1.3	-1.3	-6.4	1.2	1.3	-1.3	1.3	1.2	-6.4	-1.3	1.3	-1.3	1.3	-1.3
B1	-1.3	1.3	1.2	-6.4	-1.3	1.3	-1.3	1.3	10.2	1.3	-1.3	1.3	-1.3	1.3	-1.3	1.3	-1.3	1.3	-1.3	1.3	-1.3	-6.4	1.2	1.3
B2	1.3	-1.3	1.3	1.2	-6.4	-1.3	1.3	-1.3	1.3	10.2	1.3	-1.3	1.3	-1.3	1.3	-1.3	1.3	-1.3	1.3	-1.3	1.3	-1.3	-6.4	1.2
B3	-1.3	1.3	-1.3	1.3	1.2	-6.4	-1.3	1.3	-1.3	1.3	10.2	1.3	-1.3	1.3	-1.3	1.3	1.2	1.3	-1.3	1.3	-1.3	1.3	-1.3	-6.4
B4	1.3	-1.3	1.3	-1.3	1.3	1.2	-6.4	-1.3	1.3	-1.3	1.3	10.2	1.3	-1.3	1.3	-1.3	-6.4	1.2	1.3	-1.3	1.3	-1.3	1.3	-1.3
B5	-1.3	1.3	-1.3	1.3	-1.3	1.3	1.2	-6.4	-1.3	1.3	-1.3	1.3	10.2	1.3	-1.3	1.3	-1.3	-6.4	1.2	1.3	-1.3	1.3	-1.3	1.3
B6	-6.4	-1.3	1.3	-1.3	1.3	-1.3	1.3	1.2	1.3	-1.3	1.3	-1.3	1.3	10.2	1.3	-1.3	1.3	-1.3	-6.4	1.2	1.3	-1.3	1.3	-1.3
B7	1.2	-6.4	-1.3	1.3	-1.3	1.3	-1.3	1.3	-1.3	1.3	-1.3	1.3	-1.3	1.3	10.2	1.3	-1.3	1.3	-1.3	-6.4	1.2	1.3	-1.3	1.3
B8	1.3	1.2	-6.4	-1.3	1.3	-1.3	1.3	-1.3	1.3	-1.3	1.3	-1.3	1.3	-1.3	1.3	10.2	1.3	-1.3	1.3	-1.3	-6.4	1.2	1.3	-1.3
C1	-1.3	1.3	-1.3	1.3	-1.3	-6.4	1.2	1.3	-1.3	1.3	1.2	-6.4	-1.3	1.3	-1.3	1.3	10.2	1.3	-1.3	1.3	-1.3	1.3	-1.3	1.3
C2	1.3	-1.3	1.3	-1.3	1.3	-1.3	-6.4	1.2	1.3	-1.3	1.3	1.2	-6.4	-1.3	1.3	-1.3	1.3	10.2	1.3	-1.3	1.3	-1.3	1.3	-1.3
C3	1.2	1.3	-1.3	1.3	-1.3	1.3	-1.3	-6.4	-1.3	1.3	-1.3	1.3	1.2	-6.4	-1.3	1.3	-1.3	1.3	10.2	1.3	-1.3	1.3	-1.3	1.3
C4	-6.4	1.2	1.3	-1.3	1.3	-1.3	1.3	-1.3	1.3	-1.3	1.3	-1.3	1.3	1.2	-6.4	-1.3	1.3	-1.3	1.3	10.2	1.3	-1.3	1.3	-1.3
C5	-1.3	-6.4	1.2	1.3	-1.3	1.3	-1.3	1.3	-1.3	1.3	-1.3	1.3	-1.3	1.3	1.2	-6.4	-1.3	1.3	-1.3	1.3	10.2	1.3	-1.3	1.3
C6	1.3	-1.3	-6.4	1.2	1.3	-1.3	1.3	-1.3	-6.4	-1.3	1.3	-1.3	1.3	-1.3	1.3	1.2	1.3	-1.3	1.3	-1.3	1.3	10.2	1.3	-1.3
C7	-1.3	1.3	-1.3	-6.4	1.2	1.3	-1.3	1.3	1.2	-6.4	-1.3	1.3	-1.3	1.3	-1.3	1.3	-1.3	1.3	-1.3	1.3	-1.3	1.3	10.2	1.3
C8	1.3	-1.3	1.3	-1.3	-6.4	1.2	1.3	-1.3	1.3	1.2	-6.4	-1.3	1.3	-1.3	1.3	-1.3	1.3	-1.3	1.3	-1.3	1.3	-1.3	1.3	10.2

Table 3-3: Inductance (μH) matrix of analytical result in distributed winding construction

	A1	A2	A3	A4	A5	A6	A7	A8	B1	B2	B3	B4	B5	B6	B7	B8	C1	C2	C3	C4	C5	C6	C7	C8
A1	12.1	1.9	-0.7	0.7	-0.7	0.7	-0.7	1.9	-0.5	0.7	-0.7	0.7	-0.7	0.7	-0.7	-3.5	-3.5	-0.7	0.7	-0.7	0.7	-0.7	0.7	-0.5
A2	1.9	12.1	1.9	-0.7	0.7	-0.7	0.7	-0.7	-3.5	-0.5	0.7	-0.7	0.7	-0.7	0.7	-0.7	-0.5	-3.5	-0.7	0.7	-0.7	0.7	-0.7	0.7
A3	-0.7	1.9	12.1	1.9	-0.7	0.7	-0.7	0.7	-0.7	-3.5	-0.5	0.7	-0.7	0.7	-0.7	0.7	0.7	-0.5	-3.5	-0.7	0.7	-0.7	0.7	-0.7
A4	0.7	-0.7	1.9	12.1	1.9	-0.7	0.7	-0.7	0.7	-0.7	-3.5	-0.5	0.7	-0.7	0.7	-0.7	-0.7	0.7	-0.5	-3.5	-0.7	0.7	-0.7	0.7
A5	-0.7	0.7	-0.7	1.9	12.1	1.9	-0.7	0.7	-0.7	0.7	-0.7	-3.5	-0.5	0.7	-0.7	0.7	0.7	-0.7	0.7	-0.5	-3.5	-0.7	0.7	-0.7
A6	0.7	-0.7	0.7	-0.7	1.9	12.1	1.9	-0.7	0.7	-0.7	0.7	-0.7	-3.5	-0.5	0.7	-0.7	-0.7	0.7	-0.7	0.7	-0.5	-3.5	-0.7	0.7
A7	-0.7	0.7	-0.7	0.7	-0.7	1.9	12.1	1.9	-0.7	0.7	-0.7	0.7	-0.7	-3.5	-0.5	0.7	0.7	-0.7	0.7	-0.7	0.7	-0.5	-3.5	-0.7
A8	1.9	-0.7	0.7	-0.7	0.7	-0.7	1.9	12.1	0.7	-0.7	0.7	-0.7	0.7	-0.7	-3.5	-0.5	-0.7	0.7	-0.7	0.7	-0.7	0.7	-0.5	-3.5
B1	-0.5	-3.5	-0.7	0.7	-0.7	0.7	-0.7	0.7	12.1	1.9	-0.7	0.7	-0.7	0.7	-0.7	1.9	-3.5	-0.5	0.7	-0.7	0.7	-0.7	0.7	-0.7
B2	0.7	-0.5	-3.5	-0.7	0.7	-0.7	0.7	-0.7	1.9	12.1	1.9	-0.7	0.7	-0.7	0.7	-0.7	-0.7	-3.5	-0.5	0.7	-0.7	0.7	-0.7	0.7
B3	-0.7	0.7	-0.5	-3.5	-0.7	0.7	-0.7	0.7	-0.7	1.9	12.1	1.9	-0.7	0.7	-0.7	0.7	0.7	-0.7	-3.5	-0.5	0.7	-0.7	0.7	-0.7
B4	0.7	-0.7	0.7	-0.5	-3.5	-0.7	0.7	-0.7	0.7	-0.7	1.9	12.1	1.9	-0.7	0.7	-0.7	-0.7	0.7	-0.7	-3.5	-0.5	0.7	-0.7	0.7
B5	-0.7	0.7	-0.7	0.7	-0.5	-3.5	-0.7	0.7	-0.7	0.7	-0.7	1.9	12.1	1.9	-0.7	0.7	0.7	-0.7	0.7	-0.7	-3.5	-0.5	0.7	-0.7
B6	0.7	-0.7	0.7	-0.7	0.7	-0.5	-3.5	-0.7	0.7	-0.7	0.7	-0.7	1.9	12.1	1.9	-0.7	-0.7	0.7	-0.7	0.7	-0.7	-3.5	-0.5	0.7
B7	-0.7	0.7	-0.7	0.7	-0.7	0.7	-0.5	-3.5	-0.7	0.7	-0.7	0.7	-0.7	1.9	12.1	1.9	0.7	-0.7	0.7	-0.7	0.7	-0.7	-3.5	-0.5
B8	-3.5	-0.7	0.7	-0.7	0.7	-0.7	0.7	-0.5	1.9	-0.7	0.7	-0.7	0.7	-0.7	1.9	12.1	-0.5	0.7	-0.7	0.7	-0.7	0.7	-0.7	-3.5
C1	-3.5	-0.5	0.7	-0.7	0.7	-0.7	0.7	-0.7	-3.5	-0.7	0.7	-0.7	0.7	-0.7	0.7	-0.5	12.1	1.9	-0.7	0.7	-0.7	0.7	-0.7	1.9
C2	-0.7	-3.5	-0.5	0.7	-0.7	0.7	-0.7	0.7	-0.5	-3.5	-0.7	0.7	-0.7	0.7	-0.7	0.7	1.9	12.1	1.9	-0.7	0.7	-0.7	0.7	-0.7
C3	0.7	-0.7	-3.5	-0.5	0.7	-0.7	0.7	-0.7	0.7	-0.5	-3.5	-0.7	0.7	-0.7	0.7	-0.7	-0.7	1.9	12.1	1.9	-0.7	0.7	-0.7	0.7
C4	-0.7	0.7	-0.7	-3.5	-0.5	0.7	-0.7	0.7	-0.7	0.7	-0.5	-3.5	-0.7	0.7	-0.7	0.7	0.7	-0.7	1.9	12.0	1.9	-0.7	0.7	-0.7
C5	0.7	-0.7	0.7	-0.7	-3.5	-0.5	0.7	-0.7	0.7	-0.7	0.7	-0.5	-3.5	-0.7	0.7	-0.7	-0.7	0.7	-0.7	1.9	12.1	1.9	-0.7	0.7
C6	-0.7	0.7	-0.7	0.7	-0.7	-3.5	-0.5	0.7	-0.7	0.7	-0.7	0.7	-0.5	-3.5	-0.7	0.7	0.7	-0.7	0.7	-0.7	1.9	12.1	1.9	-0.7
C7	0.7	-0.7	0.7	-0.7	0.7	-0.7	-3.5	-0.5	0.7	-0.7	0.7	-0.7	0.7	-0.5	-3.5	-0.7	-0.7	0.7	-0.7	0.7	-0.7	1.9	12.1	1.9
C8	-0.5	0.7	-0.7	0.7	-0.7	0.7	-0.7	-3.5	-0.7	0.7	-0.7	0.7	-0.7	0.7	-0.5	-3.5	1.9	-0.7	0.7	-0.7	0.7	-0.7	1.9	12.1

Table 3-4: Inductance (μH) matrix of FEA (Maxwell) result in sectored winding construction

	A1	A2	A3	A4	A5	A6	A7	A8	B1	B2	B3	B4	B5	B6	B7	B8	C1	C2	C3	C4	C5	C6	C7	C8
A1	10.2	1.3	-1.3	1.3	-1.3	1.3	-1.3	1.3	1.2	1.3	-1.3	1.3	-1.3	1.3	-1.3	-6.4	-6.4	-1.3	1.3	-1.3	1.3	-1.3	1.3	1.2
A2	1.3	10.2	1.3	-1.3	1.3	-1.3	1.3	-1.3	-6.4	1.2	1.3	-1.3	1.3	-1.3	1.3	-1.3	1.2	-6.4	-1.3	1.3	-1.3	1.3	-1.3	1.3
A3	-1.3	1.3	10.2	1.3	-1.3	1.3	-1.3	1.3	-1.3	-6.4	1.2	1.3	-1.3	1.3	-1.3	1.3	1.3	1.2	-6.4	-1.3	1.3	-1.3	1.3	-1.3
A4	1.3	-1.3	1.3	10.2	1.3	-1.3	1.3	-1.3	1.3	-1.3	-6.4	1.2	1.3	-1.3	1.3	-1.3	-1.3	1.3	1.2	-6.4	-1.3	1.3	-1.3	1.3
A5	-1.3	1.3	-1.3	1.3	10.2	1.3	-1.3	1.3	-1.3	1.3	-1.3	-6.4	1.2	1.3	-1.3	1.3	1.3	-1.3	1.3	1.2	-6.4	-1.3	1.3	-1.3
A6	1.3	-1.3	1.3	-1.3	1.3	10.2	1.3	-1.3	1.3	-1.3	1.3	-1.3	-6.4	1.2	1.3	-1.3	-1.3	1.3	-1.3	1.3	1.2	-6.4	-1.3	1.3
A7	-1.3	1.3	-1.3	1.3	-1.3	1.3	10.2	1.3	-1.3	1.3	-1.3	1.3	-1.3	-6.4	1.2	1.3	1.3	-1.3	1.3	-1.3	1.3	1.2	-6.4	-1.3
A8	1.3	-1.3	1.3	-1.3	1.3	-1.3	1.3	10.2	1.3	-1.3	1.3	-1.3	1.3	-1.3	-6.4	1.2	-1.3	1.3	-1.3	1.3	-1.3	1.3	1.2	-6.4
B1	1.2	-6.4	-1.3	1.3	-1.3	1.3	-1.3	1.3	10.2	1.3	-1.3	1.3	-1.3	1.3	-1.3	1.3	-6.4	1.2	1.3	-1.3	1.3	-1.3	1.3	-1.3
B2	1.3	1.2	-6.4	-1.3	1.3	-1.3	1.3	-1.3	1.3	10.2	1.3	-1.3	1.3	-1.3	1.3	-1.3	-1.3	-6.4	1.2	1.3	-1.3	1.3	-1.3	1.3
B3	-1.3	1.3	1.2	-6.4	-1.3	1.3	-1.3	1.3	-1.3	1.3	10.2	1.3	-1.3	1.3	-1.3	1.3	1.3	-1.3	-6.4	1.2	1.3	-1.3	1.3	-1.3
B4	1.3	-1.3	1.3	1.2	-6.4	-1.3	1.3	-1.3	1.3	-1.3	1.3	10.2	1.3	-1.3	1.3	-1.3	-1.3	1.3	-1.3	-6.4	1.2	1.3	-1.3	1.3
B5	-1.3	1.3	-1.3	1.3	1.2	-6.4	-1.3	1.3	-1.3	1.3	-1.3	1.3	10.2	1.3	-1.3	1.3	1.3	-1.3	1.3	-1.3	-6.4	1.2	1.3	-1.3
B6	1.3	-1.3	1.3	-1.3	1.3	1.2	-6.4	-1.3	1.3	-1.3	1.3	-1.3	1.3	10.2	1.3	-1.3	-1.3	1.3	-1.3	1.3	-1.3	-6.4	1.2	1.3
B7	-1.3	1.3	-1.3	1.3	-1.3	1.3	1.2	-6.4	-1.3	1.3	-1.3	1.3	-1.3	1.3	10.2	1.3	1.3	-1.3	1.3	-1.3	1.3	-1.3	-6.4	1.2
B8	-6.4	-1.3	1.3	-1.3	1.3	-1.3	1.3	1.2	1.3	-1.3	1.3	-1.3	1.3	-1.3	1.3	10.2	1.2	1.3	-1.3	1.3	-1.3	1.3	-1.3	-6.4
C1	-6.4	1.2	1.3	-1.3	1.3	-1.3	1.3	-1.3	-6.4	-1.3	1.3	-1.3	1.3	-1.3	1.3	1.2	10.2	1.3	-1.3	1.3	-1.3	1.3	-1.3	1.3
C2	-1.3	-6.4	1.2	1.3	-1.3	1.3	-1.3	1.3	1.2	-6.4	-1.3	1.3	-1.3	1.3	-1.3	1.3	1.3	10.2	1.3	-1.3	1.3	-1.3	1.3	-1.3
C3	1.3	-1.3	-6.4	1.2	1.3	-1.3	1.3	-1.3	1.3	1.2	-6.4	-1.3	1.3	-1.3	1.3	-1.3	-1.3	1.3	10.2	1.3	-1.3	1.3	-1.3	1.3
C4	-1.3	1.3	-1.3	-6.4	1.2	1.3	-1.3	1.3	-1.3	1.3	1.2	-6.4	-1.3	1.3	-1.3	1.3	1.3	-1.3	1.3	10.2	1.3	-1.3	1.3	-1.3
C5	1.3	-1.3	1.3	-1.3	-6.4	1.2	1.3	-1.3	1.3	-1.3	1.3	1.2	-6.4	-1.3	1.3	-1.3	-1.3	1.3	-1.3	1.3	10.2	1.3	-1.3	1.3
C6	-1.3	1.3	-1.3	1.3	-1.3	-6.4	1.2	1.3	-1.3	1.3	-1.3	1.3	1.2	-6.4	-1.3	1.3	1.3	-1.3	1.3	-1.3	1.3	10.2	1.3	-1.3
C7	1.3	-1.3	1.3	-1.3	1.3	-1.3	-6.4	1.2	1.3	-1.3	1.3	-1.3	1.3	1.2	-6.4	-1.3	-1.3	1.3	-1.3	1.3	-1.3	1.3	10.2	1.3
C8	1.2	1.3	-1.3	1.3	-1.3	1.3	-1.3	-6.4	-1.3	1.3	-1.3	1.3	-1.3	1.3	1.2	-6.4	1.3	-1.3	1.3	-1.3	1.3	-1.3	1.3	10.2

Table 3-5: Inductance (μH) matrix of analytical result in sectored winding construction

3.6 Conclusion

This chapter presents mathematical models of arbitrary multi three-phase PMSM. In Section 3.1, the inductance matrix of arbitrary multi-phase PMSM is analyzed by calculating the flux linkage produced by every single coil of the stator winding. Section 3.2 derives the mathematical matrix torque equations of arbitrary multi three-phase machines, with detailed analysis on the relationship between phase current and phase voltage by using the multi three-phase inductance matrix. Section 3.3 describes the torque equations of multi three-phase machine with voltage and current space vectors. Section 3.4 shows an overview of different machines used in this thesis.

The simulation results of machine inductances from FEA (Finite Element Analysis) model in Maxwell and analytical models in Section 3.1 are shown in Section 3.5. It shows that the analytical results matches with the FEA results generally. Besides, the distributed winding construction and sectored winding construction have different mutual coupling effects. The distributed winding construction has balanced mutual coupling effect in each three-phase subsystem, while the sectored winding construction has weaker mutual coupling effect with other subsystems. The numerical, FEA and experimental results will be presented in Chapter 5 and Chapter 6 to validate the analytical torque equations in Section 3.2 and 3.3.

Chapter 4 : Analysis of PWM related torque ripple reduction method in multi three-phase drives

4.1 Modelling of multi three-phase PWM voltage converters

For double-edge naturally sampled pulse width modulation, the harmonic components of the PWM voltage waveform of each converter leg, and the resulting phase voltage, can be evaluated by using the double Fourier integration [84]. The voltage difference between the terminals a_1, b_1, c_1, …, a_N, b_N, c_N and the middle point of the DC link (z in Figure 3-5) is referred to as $u_{k_p\mathrm{z}}$. Its time-varying expression $u_{k_p\mathrm{z}}(t)$ can be represented by (4-1):

$$u_{k_p\mathrm{z}}(t) = \frac{V_{\mathrm{dc}}}{2} M\cos[y(t) - \alpha_p] + \sum_{m=1}^{\infty} \sum_{n=-\infty}^{\infty} A_{mn} \cos\{m x_p(t) + n[y(t) - \alpha_p]\}, \tag{4-1}$$

With:

$$A_{mn} = \frac{2V_{\mathrm{dc}}}{m\pi} J_n\left(m\frac{\pi}{2}M\right)\sin[(m+n)\frac{\pi}{2}], \tag{4-2}$$

$$x_p(t) = \omega_{\mathrm{c}} t + \theta_{\mathrm{c},p}, \tag{4-3}$$

$$y(t) = \omega_{\mathrm{o}} t + \theta_{\mathrm{o}}, \tag{4-4}$$

where $k \in \{a, b, c\}$ and $p \in \{1, \dots, N\}$. α_p is the space phase shift angle between the p^{th} three-phase system and the stator reference frame (resulting from the machine current control of the multiphase machine). V_{dc} is the DC link supply voltage of each independent converter module. M is the modulation index, ($M \in [0,1]$). m and n are the carrier and modulating signal index respectively. $x_p(t)$ is the time-varying angle of the carrier signal in the p^{th} three-phase system [rad]. $y(t)$ is time-varying angle of the fundamental phase voltage (modulating signal) of the first three-phase system [rad]. A_{mn} is the amplitude of the harmonic component. ω_c is the frequency of the carrier signal in rad/s (f_c is the frequency of the carrier signal in Hz). ω_o is the frequency of the modulating signal in rad/s (f_o is the frequency of the modulating signal in Hz). $\theta_{c,p}$ is the phase angle of the carrier signal of the p^{th} three-phase system. $\theta_o$is the phase angle of the modulating signal of the first three-phase system. According to (4-1) (4-2) (4-3) and (4-4), setting V_{dc} = 60 V, M = 0.8, f_o = 50 Hz, f_c =2 kHz, the time-varying phase leg voltage waveform and its FFT spectrum are shown in Figure 4-1.

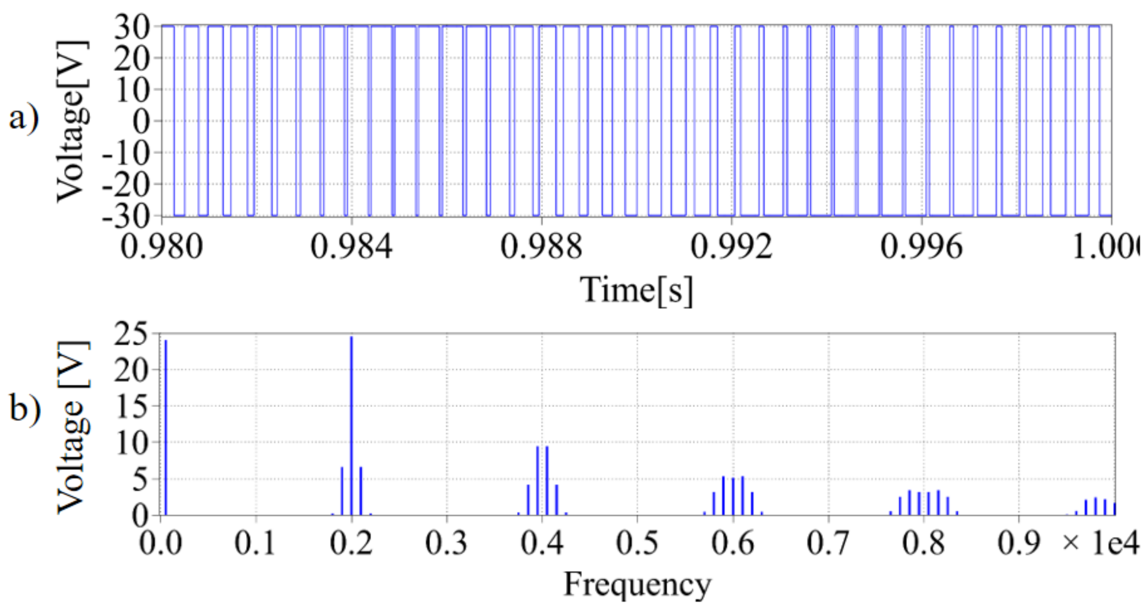

Figure 4-1: Phase leg voltage a) time varying phase leg voltage b) the corresponding FFT spectrum of the phase leg voltage waveform

According to (4-1), the phase leg voltage of the p^{th}, $p \in \{1,..,N\}$ three-phase subsystem $u_{\mathrm{a}_p\mathrm{z}}$, $u_{\mathrm{b}_p\mathrm{z}}$ and $u_{\mathrm{c}_p\mathrm{z}}$ are represented as:

$$u_{a_p\mathrm{z}}(t) = \frac{V_{\mathrm{dc}}}{2} M\cos[y_{\mathrm{a}}(t) - \alpha_p] \\ + \sum_{m=1}^{\infty} \sum_{n=-\infty}^{\infty} A_{mn} \cos\{m x_p(t) + n[y_{\mathrm{a}}(t) - \alpha_p]\}, \tag{4-5}$$

$$u_{b_p\mathrm{z}}(t) = \frac{V_{\mathrm{dc}}}{2} M\cos[y_{\mathrm{a}}(t) - \frac{2}{3}\pi - \alpha_p] \\ + \sum_{m=1}^{\infty} \sum_{n=-\infty}^{\infty} A_{mn} \cos\{m x_p(t) + n[y_{\mathrm{a}}(t) - \tfrac{2}{3}\pi - \alpha_p]\}, \tag{4-6}$$

$$u_{c_p\mathrm{z}}(t) = \frac{V_{\mathrm{dc}}}{2} M\cos[y_{\mathrm{a}}(t) + \frac{2}{3}\pi - \alpha_p] \\ + \sum_{m=1}^{\infty} \sum_{n=-\infty}^{\infty} A_{mn} \cos\{m x_p(t) + n[y_{\mathrm{a}}(t) + \tfrac{2}{3}\pi - \alpha_p]\}, \tag{4-7}$$

with:

$$y_{\mathrm{a}}(t) = \omega_{\mathrm{o}} t + \theta_{\mathrm{o,a}}, \tag{4-8}$$

where $y_{\mathrm{a}}(t)$ is time-varying angle of the fundamental phase A voltage (modulating signal) of the first three-phase system [rad].

According to Euler's formula:

$$\cos(\gamma) = \frac{e^{j\gamma} + e^{-j\gamma}}{2}, \tag{4-9}$$

Substituting (4-9) into (4-5), (4-6) and (4-7):

$$u_{a_p\mathrm{z}}(t) = \frac{V_{\mathrm{dc}}}{4} M\{e^{j(y_{\mathrm{a}}(t) - \alpha_p)} + e^{-j(y_{\mathrm{a}}(t) - \alpha_p)}\} \\ + \frac{1}{2} \sum_{m=1}^{\infty} \sum_{n=-\infty}^{\infty} A_{mn} \{e^{j[m x_p(t) + n(y_{\mathrm{a}}(t) - \alpha_p)]} + e^{-j[m x_p(t) + n(y_{\mathrm{a}}(t) - \alpha_p)]}\}, \tag{4-10}$$

$$u_{b_p\mathrm{z}}(t) = \frac{V_{\mathrm{dc}}}{4} M\{e^{j(y_{\mathrm{a}}(t) - \frac{2}{3}\pi - \alpha_p)} + e^{-j(y_{\mathrm{a}}(t) - \frac{2}{3}\pi - \alpha_p)}\} \tag{4-11}$$

$$+\frac{1}{2}\sum_{m=1}^{\infty}\sum_{n=-\infty}^{\infty} A_{mn}\{e^{j[mx_p(t)+n(y_\mathrm{a}(t)-\frac{2}{3}\pi-\alpha_p)]}+e^{-j[mx_p(t)+n(y_\mathrm{a}(t)-\frac{2}{3}\pi-\alpha_p)]}\},$$

$$u_{c_p\mathrm{z}}(t)=\frac{V_\mathrm{dc}}{4}M\{e^{j(y_\mathrm{a}(t)+\frac{2}{3}\pi-\alpha_p)}+e^{-j(y_\mathrm{a}(t)+\frac{2}{3}\pi-\alpha_p)}\}$$

(4-12)

$$+\frac{1}{2}\sum_{m=1}^{\infty}\sum_{n=-\infty}^{\infty} A_{mn}\{e^{j[mx_p(t)+n(y_\mathrm{a}(t)+\frac{2}{3}\pi-\alpha_p)]}+e^{-j[mx_p(t)+n(y_\mathrm{a}(t)+\frac{2}{3}\pi-\alpha_p)]}\}.$$

The phase voltage is the voltage drop between the terminals a_1, b_1, c_1, …, a_N, b_N, c_N and the terminals o_1, …, o_N, and are named as u_{A_1}, u_{B_1}, u_{C_1}, …, u_{A_N}, u_{B_N}, u_{C_N} respectively. The phase voltage space vector of the p^{th}, $p \in \{1,..,N\}$ three-phase subsystem is represented in (3-33). The voltage difference between o_p and z, is referred to as the common mode voltage $u_{\mathrm{o}_p\mathrm{z}}$. Since each three-phase system is star connected, according to Kirchhoff's law, the common mode voltage will not generate any zero sequence current. Therefore, the common mode voltage will not lead to torque ripple, and its effects are not considered in this thesis. Removing all the common mode voltage components from the phase leg voltages in (4-10), (4-11) and (4-12), the p^{th} voltage space vector can be obtained by substituting (4-10), (4-11) and (4-12) into (3-33), which can represented as:

$$\vec{u}_p(t)=\frac{V_\mathrm{dc}}{2}Me^{j[y_\mathrm{a}(t)-\alpha_p]}+$$

$$\frac{1}{3}A_{mn}\sum_{m=1}^{\infty}\sum_{n=-\infty}^{\infty}\begin{matrix}\overbrace{e^{j[mx_p(t)+n(y_\mathrm{a}(t)-\alpha_p)]}+e^{j[mx_p(t)+n(y_\mathrm{a}(t)-\frac{2}{3}\pi-\alpha_p)]}+e^{j[mx_p(t)+n(y_\mathrm{a}(t)+\frac{2}{3}\pi-\alpha_p)]}}^{\text{positive sequence}}\\ \underbrace{e^{-j[mx_p(t)+n(y_\mathrm{a}(t)-\alpha_p)]}+e^{-j[mx_p(t)+n(y_\mathrm{a}(t)-\frac{2}{3}\pi-\alpha_p)]}e^{-j[mx_p(t)+n(y_\mathrm{a}(t)+\frac{2}{3}\pi-\alpha_p)]}}_{\text{negative sequence}}\end{matrix},$$

(4-13)

simplified as:

$$\vec{u}_p(t) = \frac{V_{\text{dc}}}{2} M e^{j[y_{\text{a}}(t)-\alpha_p]} +$$

$$A_{mn} \sum_{m=1}^{\infty} \sum_{n=-\infty}^{\infty} \begin{cases} e^{j[mx_p(t)+n(y_{\text{a}}(t)-\alpha_p)]} & ,n = 3l+1 \\ e^{-j[mx_p(t)+n(y_{\text{a}}(t)-\alpha_p)]} & ,n = 3l-1 \end{cases} \tag{4-14}$$

where l is an integer number. The voltage space vector $\vec{u}_p(t)$ contains the fundamental component $\frac{V_{\text{dc}}}{2} M e^{j[y_{\text{a}}(t)-\alpha_p]}$ and the harmonic components which are caused by the PWM. The harmonic components include both positive sequence components:

$$\sum_{m=1}^{\infty} \sum_{n=-\infty}^{\infty} A_{mn}\, e^{j[mx_p(t)+n(y_{\text{a}}(t)-\alpha_p)]},$$

and negative sequence components:

$$\sum_{m=1}^{\infty} \sum_{n=-\infty}^{\infty} A_{mn}\, e^{-j[mx_p(t)+n(y_{\text{a}}(t)-\alpha_p)]}.$$

Considering an N three-phase PMSM with arbitrary phase shifts referring to the reference frame, its effective two-pole stator winding construction is shown in Figure 4-2. The total voltage space vector fed by modular three-phase converters to control the N multi three-phase PMSM are represented in (3-34). The total voltage space vector with all harmonic contributions can be obtained by substituting (3-34) into (4-14):

$$\vec{u}_{total}(t) = \frac{V_{\text{dc}}}{2} M e^{jy_{\text{a}}(t)} +$$

$$\frac{1}{N} A_{mn} \sum_{p=1}^{N} \sum_{m=1}^{\infty} \sum_{n=-\infty}^{\infty} \begin{cases} e^{j[mx_p(t)+n(y_{\text{a}}(t)-\alpha_p)+\alpha_p]} & ,n = 3l+1 \\ e^{-j[mx_p(t)+n(y_{\text{a}}(t)-\alpha_p)-\alpha_p]} & ,n = 3l-1 \end{cases} \tag{4-15}$$

The voltage space vector $\vec{u}_{total}(t)$ contains the fundamental component $\frac{V_{\text{dc}}}{2} M e^{jy(t)}$ and the harmonic components which are caused by the PWM. The harmonic components include both positive sequence components:

$$\frac{1}{N} A_{mn} \sum_{p=1}^{N} \sum_{m=1}^{\infty} \sum_{n=-\infty}^{\infty} e^{j[mx_p(t)+n(y_a(t)-\alpha_p)+\alpha_p]},$$

and negative sequence components:

$$\frac{1}{N} A_{mn} \sum_{p=1}^{N} \sum_{m=1}^{\infty} \sum_{n=-\infty}^{\infty} e^{-j[mx_p(t)+n(y_a(t)-\alpha_p)-\alpha_p)]}.$$

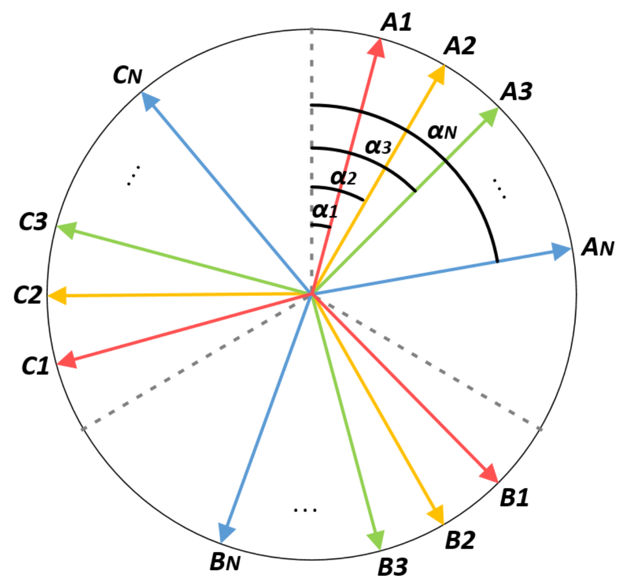

Figure 4-2: Effective two-pole *N* three-phase winding construction

According to (4-15), the total harmonic voltage space vector can be eliminated by applying different values of carrier phase angle (θ_c) into different three-phase subsystems. For example, for a *N* three-phase PMSM without any space phase shifts among different subsystems ($\alpha_p = 0$, for $p \in \{1, \ldots, N\}$). When $x_p = \omega_c t + \frac{2\pi(p-1)}{N}$, all of the harmonics are cancelled out except the groups of the harmonics around $Nm\omega_c$. The total voltage space vector ($\vec{u}_{total}$) FFT spectra with applying $\frac{2\pi(p-1)}{N}$ to each three-phase subsystem are shown in Figure 4-3, Figure 4-4 and Figure 4-5. Figure 4-3, Figure 4-4 and Figure 4-5 show that the PWM voltage harmonic components can be effectively eliminated by applying the proposed CPS-PWM. There is more degrees of freedom to eliminate the voltage harmonic components with increasing number of multi three-phase subsystems (*N*). As the fundamental voltage of a *N* three-phase drive is a constant despite the value of *N*, the voltage components without CPS-PWM are always the same as the voltage components of *N=1*. All the voltage harmonic groups less than $10f_c$ are eliminated when *N*=10 applying the proposed CPS-PWM. In addition, comparing Figure 4-3, Figure 4-4 and Figure 4-5, the fundamental voltage are proportional to the modulation index M due to the term $\frac{V_{\mathrm{dc}}}{2}Me^{j\gamma_{\mathrm{a}}(t)}$ in (4-15). The amplitude of each PWM harmonic component changes under different modulation index (*M*). The modulation index is one of the main factor affecting the amplitudes of the harmonics.

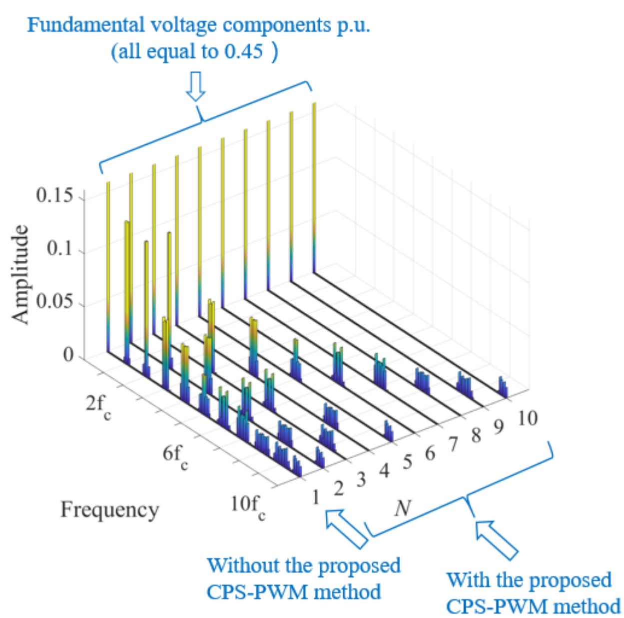

Figure 4-3: Total voltage space vector FFT spectra without and with applying CPS-PWM under M=0.9

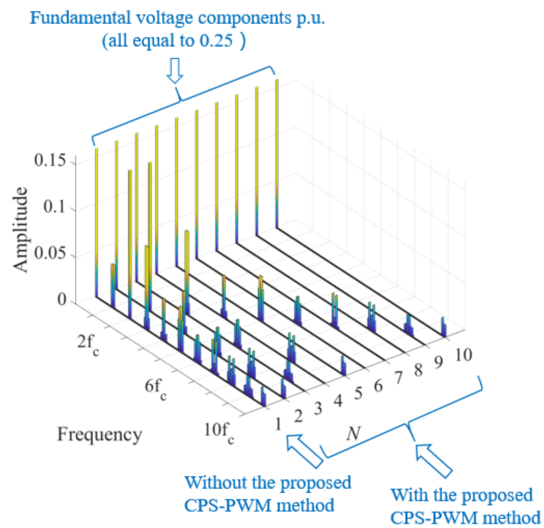

Figure 4-4: Total voltage space vector FFT spectra without and with applying CPS-PWM under M=0.5

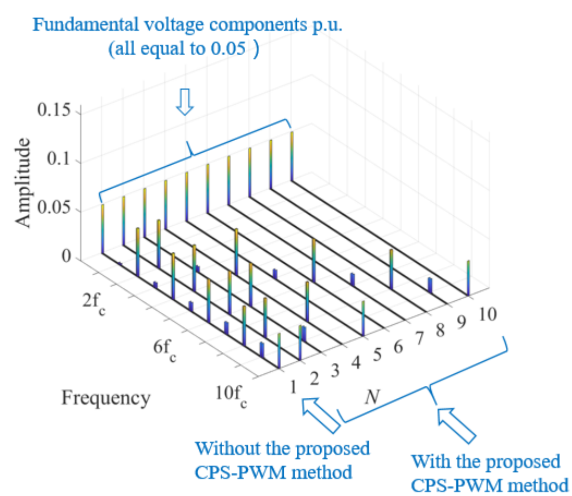

Figure 4-5: Total voltage space vector FFT spectra without and with applying CPS-PWM under M=0.1

4.2 Analytical PWM related torque equations in multi three-phase drives

The main torque ripple caused by the PWM is due to the interaction of the high order winding field harmonics with the fundamental component of the permanent magnet field. The torque ripple caused by the interaction of the high order harmonics (5^{th}, 7^{th}, 11^{th}, 13^{th}…) of back-EMF is neglected in this analysis. Thus, only the fundamental component of the total back-EMF space vector $\vec{e}_{\text{total,f}}(t)$ is considered while modelling the total phase current space vector $\vec{\imath}_{\text{total}}(t)$. The relationship between phase voltages and phase currents is shown in (3-18). Since the three phases in each subsystem are star-connected, the sum of three-phase currents is zero in any subsystem leading to the following constraint:

$$i_{\text{a}_p} + i_{\text{b}_p} + i_{\text{c}_p} = 0, \tag{4-16}$$

where for $p \in \{1, \ldots, N\}$. According to (3-18), (4-15) and (4-16), the total current space vector $\vec{\imath}_{\text{total}}(t)$ can be represented as:

$$\vec{\imath}_{total}(t) = I_{\text{f}} e^{jy'(t)} + \frac{1}{N}\frac{A_{mn}}{Z(\omega_{mn})}\sum_{m=1}^{\infty}\sum_{n=-\infty}^{\infty} A_{mn} \begin{cases} e^{j[mx_p(t)+n(y_{\text{a}}(t)-\alpha_p)+\alpha_p]} & ,n = 3l+1 \\ e^{-j[mx_p(t)+n(y_{\text{a}}(t)-\alpha_p)-\alpha_p]} & ,n = 3l-1 \end{cases}, \tag{4-17}$$

with:

$$I_{\text{f}} e^{jy'(t)} = \frac{1}{Z(\omega_o)}\left[\frac{V_{\text{dc}}}{2} M e^{jy(t)} - \vec{e}_{\text{total,f}}(t)\right], \tag{4-18}$$

$$y'(t) = \omega_{\text{o}} t + \theta'_{\text{o}}, \tag{4-19}$$

$$\omega_{mn} = n\omega_{\text{o}} + m\omega_{\text{c}}, \tag{4-20}$$

where ω_{mn} is the frequency of the harmonic component with *m* carrier signal index and *n* modulating signal index. $Z(\omega_{mn})$ is the impedance of the harmonic component at frequency ω_{mn}. $Z(\omega_o)$ is the impedance of the fundamental component, and θ_{o}' is the phase angle of the fundamental component of phase current of the first three-phase system.

Under the assumption of considering for only the fundamental component of the total back-EMF space vector $\vec{e}_{\mathrm{total,f}}(t)$, the instantaneous electromagnetic torque can be represented by:

$$T_{\mathrm{total,PWM}}(t) = \frac{3N}{2\omega_m}\left[\vec{\iota}_{\mathrm{total}}(t) \cdot \vec{e}_{\mathrm{total,f}}(t)\right]. \tag{4-21}$$

It results from (4-21) that the average torque is produced by controlling the fundamental component I_{f} of the total current space vector $\vec{\iota}_{\mathrm{total}}(t)$, whereas the main torque ripple caused by the PWM is generated by the harmonic components in the total current space vector $\vec{\iota}_{\mathrm{total}}(t)$. Therefore, the minimization of the harmonic components of the total current space vector $\vec{\iota}_{\mathrm{total}}(t)$ corresponds to the minimization of the related torque ripple. As it is expressed in (4-17), there are N degrees of freedom to change the carrier phase angle $\theta_{\mathrm{c},p}$ of each sub three-phase system. Thus, different optimized carrier phase angles $\theta_{\mathrm{c},p}$ can be found for multi three-phase drives with different values of three-phase systems N and related phase shift angles α_p.

As a case study, an 18 slots and 6 poles triple three-phase PMSM is shown in Figure 4-6. The machine has three sectors, sector 1, sector 2 and sector 3 respectively. Each sector has three phases (phase A, phase B, phase C) with an independent floating neutral point. Therefore, the three-phase back-EMFs generated in each sector are supposed to have no electrical degree phase shift with respect to other sectors.

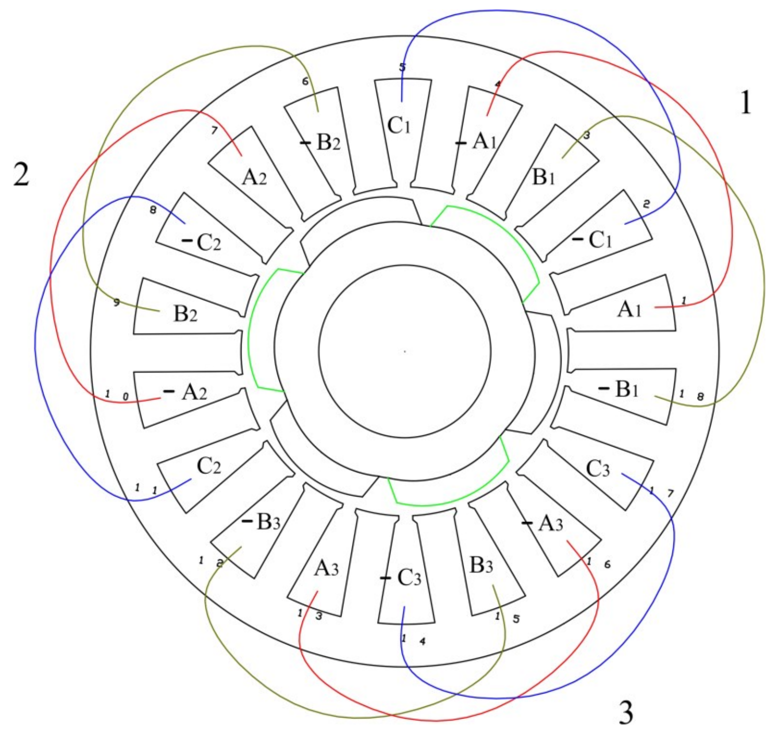

Figure 4-6: Cross section of the 18 slots – 6 poles 3 sectored PM machine [102]

For the mathematical model of the total current space vector $\vec{i}_{\text{total}}(t)$ shown in (4-17), the number of three-phase systems is 3 ($N = 3$) and the equivalent space phase shift angle is 0 for all of the three sectors ($\alpha_p = 0, p \in \{1, 2, 3\}$).

The effect of the carrier phase angle of the p^{th} three-phase system $\theta_{\text{c},p}$ ($x_p(t) = \omega_\text{c} t + \theta_{\text{c},p}$) is analyzed through the voltage and current total space vector equations in (4-15) and (4-17). It is found that when the carrier phase shift angles are $\theta_{\text{c},1} = 0$, $\theta_{\text{c},2} = \frac{2\pi}{3}$ and $\theta_{\text{c},3} = \frac{4\pi}{3}$ for sector 1, sector 2 and sector 3 respectively, all of the harmonic components of the current space vector are cancelled out except the groups of harmonics around the frequency of $3mf_\text{c}$ ($m \in \{1, 2, \dots, \infty\}$). According to (4-21), the corresponding FFT spectrum of the normalized torque without and with applying the proposed carrier phase shift angles under different modulation index (M) is shown in Figure 4-7. In Figure 4-7,

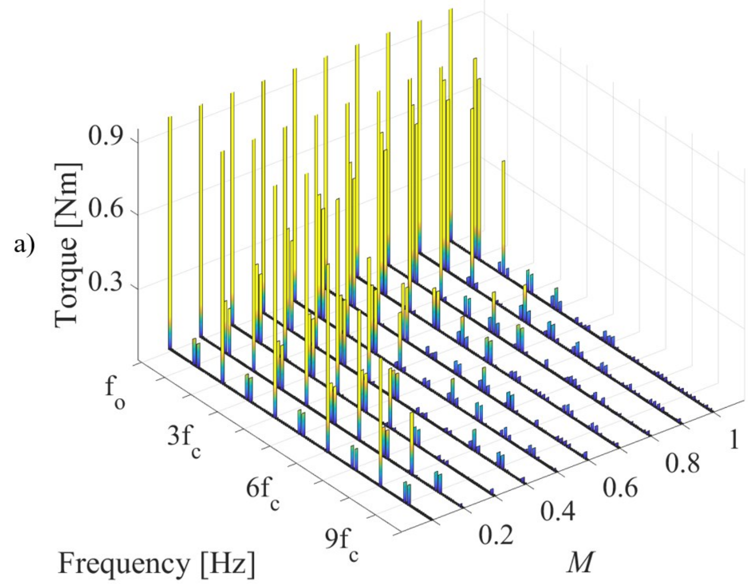

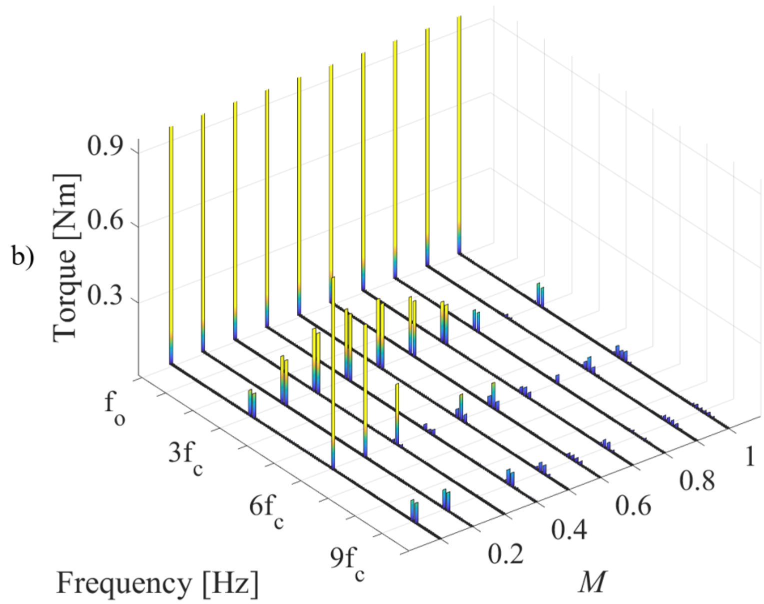

Figure 4-7: FFT spectrum of the normalized torque a) without applying carrier phase shift method b) with applying the proposed carrier phase shift method [102].

the x-axis refers to the frequency of the groups of harmonic components at mf_c ($m \in \{1, 2, \dots, \infty\}$; f_c is the carrier frequency), and the y-axis refer to the modulation index M.

As it is shown in (4-2) and (4-17), the amplitude of each PWM harmonic component changes under different moduation index (M). The modulation index is one of the main factor affecting the amplitudes of the harmonics. As it is shown in (4-2), the modulation index M affects the amplitudes of the PWM harmonic components with the term of the Bessel functions $J_n\left(m\frac{\pi}{2}M\right)$ ($m, n \in \{1, 2, 3 \dots\}$). The Bessel functions $J_n(\xi)$ for $n = 0,1, \dots, 6$ are shown in Figure 4-8, which shows that $J_n(\xi)$ tends to decease with the increase of ξ.

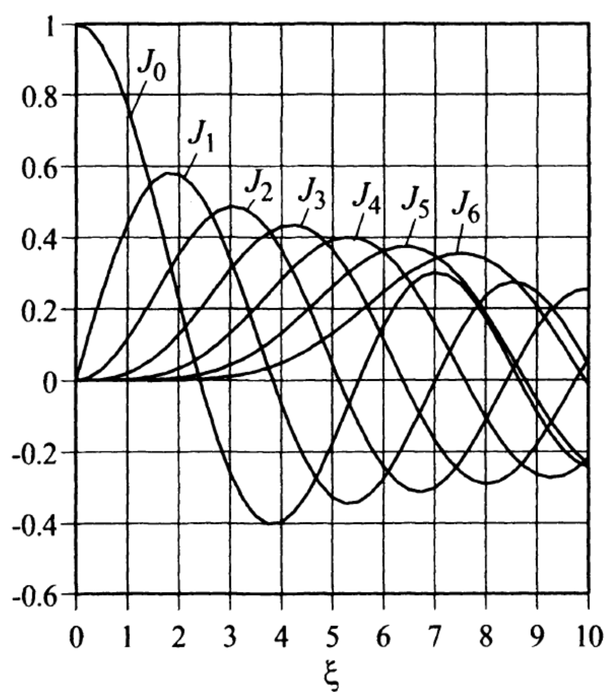

Figure 4-8: Bessel functions $J_n(\xi)$ for $n = 0,1, \dots, 6$ [84]

4.3 Selective torque harmonic elimination method on dual three-phase drives

This Section presents a model of dual three-phase drives with arbitrary phase displacements. Torque ripple harmonic components can be selectively eliminated by applying a proper carrier phase shift between the two three-phase subsystems of a dual three-phase drive. This section presents how the PWM related torque ripple harmonic components can be eliminated by applying Carrier Phase Shift Pulse Width Modulation (CPS-PWM) in a dual three-phase system with arbitrary phase angle displacement. The displacement phase angle between the two sets of the three-phase stator windings (in electrical radians) is generally 0 or π/6 [41]–[43], [49]–[54]. Therefore, two dual three-phase Permanent Magnet Synchronous Machines (PMSM) with phase displacement of 0 and π/6, considering as two case studies, are considered with their respective CPS-PWM.

4.3.1 Dual three-phase drive system

Figure 4-9 shows a dual three-phase drive system fed by two independent modular three-phase converters. The voltage differences between terminals $\mathrm{a_1}$, $\mathrm{b_1}$, $\mathrm{c_1}$, $\mathrm{a_2}$, $\mathrm{b_2}$, $\mathrm{c_2}$ and terminals $\mathrm{o_1}$, $\mathrm{o_2}$ are considered as phase voltages, which are represented by $u_{\mathrm{a_1}}$, $u_{\mathrm{b_1}}$, $u_{\mathrm{c_1}}$, $u_{\mathrm{a_2}}$, $u_{\mathrm{b_2}}$, $u_{\mathrm{c_2}}$ respectively. Similarly, the phase currents are represented by $i_{\mathrm{a_1}}$, $i_{\mathrm{b_1}}$, $i_{\mathrm{c_1}}$, $i_{\mathrm{a_2}}$, $i_{\mathrm{b_2}}$, $i_{\mathrm{c_2}}$, and the back-EMFs generated on each phase by the rotor flux (permanent magnets) can be defined as $e_{\mathrm{a_1}}$, $e_{\mathrm{b_1}}$, $e_{\mathrm{c_1}}$, $e_{\mathrm{a_2}}$, $e_{\mathrm{b_2}}$, $e_{\mathrm{c_2}}$ respectively. In the considered dual three-phase drive system it is possible to introduce a total voltage space vector $\vec{u}_{\mathrm{total}}$, current space vector $\vec{\imath}_{\text{total}}$ and the back-EMF space vector $\vec{e}_{\text{total}}$ by means of the transformation (4-22):

$$\vec{g}_{\text{total}} = \frac{1}{3}\{\underbrace{[g_{a_1}(t) + g_{b_1}(t)e^{j\frac{2}{3}\pi} + g_{c_1}(t)e^{-j\frac{2}{3}\pi}]}_{\vec{g}_1} + \underbrace{[g_{a_2}(t) + g_{b_2}(t)e^{j\left(\frac{2}{3}\pi\right)} + g_{c_2}(t)e^{j\left(-\frac{2}{3}\pi\right)}]}_{\vec{g}_2} e^{j\alpha}\}, \tag{4-22}$$

where $g \in \{u, i, e\}$; $\vec{g}_1$ and $\vec{g}_2$ are the voltage (current, back-EMF) space vectors of the first and the second three-phase subsystems respectively.

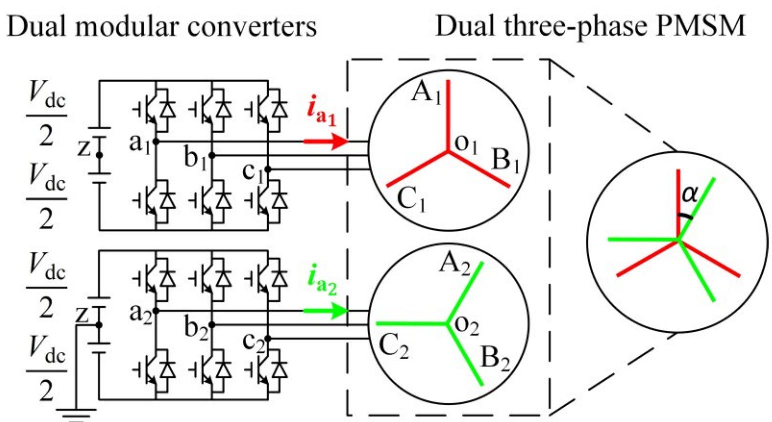

Figure 4-9: Dual three-phase drive system

The main PWM related torque ripple is caused by the interaction of the fundamental component of the rotor field with the high frequency harmonic components of the stator field. The torque ripple caused by the interaction of the high order rotor field harmonics such as 5th, 7th, 11th, 13th… are neglected in this analysis. Thus, only the fundamental component of the total back-EMF space vector $\vec{e}_{\text{total,f}}$ is considered. Therefore, the main electromagnetic torque ripple caused by the PWM current distortion $T_{\text{em,PWM}}$ can be represented by (4-23):

$$T_{\text{total,PWM}} = \frac{3}{\omega_m}\left[\vec{\imath}_{\text{total,PWM}} \cdot \vec{e}_{\text{total,f}}\right]$$
$$= \frac{3}{\omega_m}\left[\frac{\vec{u}_{\text{total,PWM}}}{Z(\omega_h)} \cdot \vec{e}_{\text{total,f}}\right], \tag{4-23}$$

where $\vec{\imath}_{\text{total,PWM}}$ includes all the PWM related harmonic components of the total current space vector $\vec{\imath}_{\text{total}}$, as $\vec{u}_{\text{total,PWM}}$ the PWM related harmonic components of the total voltage space vector $\vec{u}_{\text{total}}$. The main torque ripple caused by the PWM is generated by the voltage space vector $\vec{u}_{\text{total,PWM}}$. Thus, the elimination of the harmonic components in the voltage space vector $\vec{u}_{\text{total,PWM}}$ is related to the elimination of the corresponding harmonics in the torque ripple.

4.3.2 Analysis of PWM Related Torque Ripple Reduction Method

As it has been mentioned in Section 4.3.1, the PWM torque ripple can be reduced by eliminating the corresponding PWM harmonic components of the total voltage space vector. Therefore, for the sake of simplicity, the focus of the analysis for the torque ripple reduction is on the PWM voltage space vectors rather than on the torque.

The phase leg voltages are the voltage differences between the terminals a_1, b_1, c_1, a_2, b_2, c_2 and the middle point of the DC link (z in Figure 4-9). Considering a double-edge naturally sampled PWM, the complete PWM harmonic content of the phase leg voltage is solved by using the double Fourier integration method [84] [89]. Thus, the PWM harmonic voltage space vectors of the first three-phase subsystem $\vec{u}_{1,\text{PWM}}$ and the second three-phase subsystem with respect to the first three-phase subsystem $\vec{u}'_{2,\mathrm{PWM}}$ ($\vec{u}_{2,\mathrm{PWM}}e^{j\alpha}$) can be represented by (4-24) and (4-25) respectively:

$$\vec{u}_{1,\mathrm{PWM}} = \frac{1}{2}A_{mn} \sum_{m=1}^{\infty}\sum_{n=-\infty}^{n=\infty}\begin{cases} e^{j[(m\omega_\mathrm{c}+n\omega_\mathrm{o})t+(m\theta_{\mathrm{c}1}+n\theta_\mathrm{o})]}, & n=3k+1 \\ e^{-j[(m\omega_\mathrm{c}+n\omega_\mathrm{o})t+(m\theta_{\mathrm{c}1}+n\theta_\mathrm{o})]}, & n=3k-1 \end{cases}, \tag{4-24}$$

$$\vec{u}'_{2,\mathrm{PWM}} = \frac{1}{2}A_{mn} \sum_{m=1}^{\infty}\sum_{n=-\infty}^{n=\infty}\begin{cases} e^{j[(m\omega_\mathrm{c}+n\omega_\mathrm{o})t+(m\theta_{\mathrm{c}2}+n\theta_\mathrm{o}-n\alpha)+\alpha]}, & n=3k+1 \\ e^{-j[(m\omega_\mathrm{c}+n\omega_\mathrm{o})t+(m\theta_{\mathrm{c}2}+n\theta_\mathrm{o}-n\alpha)-\alpha]}, & n=3k-1 \end{cases}, \tag{4-25}$$

with:

$$A_{mn} = \frac{2V_\mathrm{dc}}{m\pi}J_n\left(m\frac{\pi}{2}M\right)\sin[(m+n)\frac{\pi}{2}], \tag{4-26}$$

where k is an integer number. In (4-25), α contributes to the phase of the space vector $\vec{u}'_{2,\mathrm{PWM}}$ with two terms:

- the term $e^{\pm j[n\theta_\mathrm{o}-n\alpha]}$ introduced by the control algorithm of the dual three-phase machine, which aims to maximize the performance of the drive according to the desired Field Oriented Control (FOC) strategy;
- the term $e^{j\alpha}$ which results from the definition of the total space vector according to the transformation (4-22).

Comparing (4-24) and (4-25), the amplitudes of the harmonic components are the same at the frequency of ω_{mn} with any value of m and n (the amplitudes of the PWM harmonics are $\frac{1}{2}A_{mn}$ in both (4-24) and (4-25)). As it is shown in (4-22), the total PWM harmonic voltage space vector $\vec{u}_{\mathrm{total,PWM}}$ is the sum of $\vec{u}_{1,\mathrm{PWM}}$ and $\vec{u}'_{2,\mathrm{PWM}}$. Therefore, in order to cancel out the PWM harmonic component at the frequency of ω_{mn} of the total voltage space vector $\vec{u}_{\mathrm{total,PWM}}$, an appropriate carrier phase angles $\theta_{\mathrm{c}1}$in (4-24) and $\theta_{\mathrm{c}2}$ in (4-25) can be chosen. In particular, the harmonic components (at the frequency of ω_{mn}) in (4-24) and (4-25) are eliminated if a phase shift of π is applied, which means that the harmonic contributions of the two converters to $\vec{u}_{\mathrm{total,PWM}}$ (at the frequency of ω_{mn}) needs to be out of phase.

The PWM harmonic phase angles of the two three-phase subsystem voltage space vectors ($\vec{u}_{1,\mathrm{PWM}}(0)$ and $\vec{u}'_{2,\mathrm{PWM}}(0)$) are shown in Table 4-1. Considering the low-pass filter effect of the relationship between the total voltage space vector and the total current space vector, and aware of the similarity of the transfer function related to the mechanical load, the lower order harmonics are more harmful in electrical machine systems. It results that the lower order PWM harmonic components in voltage space vectors are of first importance in the selective ripple elimination methodology. Thus, the maximum harmonic frequency in Table 4-1 is considered around $6\omega_c$ ($m \leq 6$). Due to the attenuation of higher order sidebands, 8 sidebands are taken into account in Table 4-1 ($n \leq 8$) [84]. According to (4-24) and (4-25), the initial phase angles of all the existing PWM harmonic components with $m \leq 6$ and $n \leq 8$ are listed in Table 4-1. In order to eliminate specific harmonic components of $\vec{u}_{\mathrm{total,PWM}}$ (i.e., imposing $\vec{u}_{1,\mathrm{PWM}}$ and $\vec{u}'_{2,\mathrm{PWM}}$ out of phase), the carrier phase shift ($\theta_{\mathrm{c}2} - \theta_{\mathrm{c}1}$) remains a possible degree of freedom in the control of the drive, which can be exploited in order to optimize the performance of the two three-phase subsystems operation.

The two cases of winding layouts with $\alpha = 0$ and $\alpha = \frac{\pi}{6}$ are taken into consideration for the following analyses, as significant examples. The corresponding phase angle differences between the PWM harmonic of the voltage space vector of the two three-phase subsystems with and without applying the proposed the CPS-PWM are shown in Table 4-2 for both $\alpha = 0$ and $\alpha = \frac{\pi}{6}$. As it is shown in Table 4-2, for $\alpha = 0$, all the harmonic components around ω_c, $3\omega_c$, $5\omega_c$ in the two three-phase subsystems are out of phase (π), while a carrier shift π ($\theta_{c2} - \theta_{c1} = \pi$) is applied to the dual three-phase system. In lieu, for a dual three-phase winding with $\alpha = \frac{\pi}{6}$, applying the carrier shift $\frac{\pi}{2}$ and $-\frac{\pi}{2}$ ($\theta_{c2} - \theta_{c1} = \frac{\pi}{2}$ and $\theta_{c2} - \theta_{c1} = -\frac{\pi}{2}$) lead to different sets of harmonic components out of phase (π) in the two subsystems which are listed in Table 4-2 respectively. The corresponding FFT spectra of the real part of the total voltage space vectors with the modulation index M = 0.8 are shown in Figure 4-10.

Controlling the dual three-phase machine with different $\theta_{c2} - \theta_{c1}$ shift angles results in the elimination of different PWM harmonic components. As displayed in Table 4-1, it is possible to command an appropriate value of $\theta_{c2} - \theta_{c1}$ to eliminate specific undesired PWM harmonic components in the total voltage space vector, the total current space vector, and the torque ripple.

The Sub Three-phase System	PWM Harmonic Phase Angles under Different Frequencies (different values of m and n)					
	Harmonics Around ω_c ($m = 1$)					
	$\omega_c + 2\omega_o$ ($n = 2$)	$\omega_c - 2\omega_o$ ($n = -2$)	$\omega_c + 4\omega_o$ ($n = 4$)	$\omega_c - 4\omega_o$ ($n = -4$)	$\omega_c + 8\omega_o$ ($n = 8$)	$\omega_c - 8\omega_o$ ($n = -8$)
1st	$-\theta_{c1} - 2\theta_o$	$\theta_{c1} - 2\theta_o$	$\theta_{c1} + 4\theta_o$	$-\theta_{c1} + 4\theta_o$	$-\theta_{c1} - 8\theta_o$	$\theta_{c1} - 8\theta_o$
2nd	$-\theta_{c2} + 3\alpha - 2\theta_o$	$\theta_{c2} + 3\alpha - 2\theta_o$	$\theta_{c2} - 3\alpha + 4\theta_o$	$-\theta_{c2} - 3\alpha + 4\theta_o$	$-\theta_{c2} + 9\alpha - 8\theta_o$	$\theta_{c2} + 9\alpha - 8\theta_o$
	Harmonics Around $2\omega_c$ ($m = 2$)					
	$2\omega_c + \omega_o$ ($n = 1$)	$2\omega_c - \omega_o$ ($n = -1$)	$2\omega_c + 5\omega_o$ ($n = 5$)	$2\omega_c - 5\omega_o$ ($n = -5$)	$2\omega_c + 7\omega_o$ ($n = 7$)	$2\omega_c - 7\omega_o$ ($n = -7$)
1st	$2\theta_{c1} + \theta_o$	$-2\theta_{c1} + \theta_o$	$-2\theta_{c1} - 5\theta_o$	$2\theta_{c1} - 5\theta_o$	$2\theta_{c1} + 7\theta_o$	$-2\theta_{c1} + 7\theta_o$
2nd	$2\theta_{c2} + \theta_o$	$-2\theta_{c2} + \theta_o$	$-2\theta_{c2} + 6\alpha - 5\theta_o$	$2\theta_{c2} + 6\alpha - 5\theta_o$	$2\theta_{c2} - 6\alpha + 7\theta_o$	$2\theta_{c2} - 6\alpha + 7\theta_o$
	Harmonics Around $3\omega_c$ ($m = 3$)					
	$3\omega_c + 2\omega_o$ ($n = 2$)	$3\omega_c - 2\omega_o$ ($n = -2$)	$3\omega_c + 4\omega_o$ ($n = 4$)	$3\omega_c - 4\omega_o$ ($n = -4$)	$3\omega_c + 8\omega_o$ ($n = 8$)	$3\omega_c - 8\omega_o$ ($n = -8$)
1st	$-3\theta_{c1} - 2\theta_o$	$3\theta_{c1} - 2\theta_o$	$3\theta_{c1} + 4\theta_o$	$-3\theta_{c1} + 4\theta_o$	$-3\theta_{c1} - 8\theta_o$	$3\theta_{c1} - 8\theta_o$
2nd	$-3\theta_{c2} + 3\alpha - 2\theta_o$	$3\theta_{c2} + 3\alpha - 2\theta_o$	$3\theta_{c2} - 3\alpha + 4\theta_o$	$-3\theta_{c2} - 3\alpha + 4\theta_o$	$-3\theta_{c2} + 9\alpha - 8\theta_o$	$3\theta_{c2} + 9\alpha - 8\theta_o$

	Harmonics Around $4\omega_c$ ($m = 4$)					
	$4\omega_c + \omega_o$ ($n = 1$)	$4\omega_c - \omega_o$ ($n = -1$)	$4\omega_c + 5\omega_o$ ($n = 5$)	$4\omega_c - 5\omega_o$ ($n = -5$)	$4\omega_c + 7\omega_o$ ($n = 7$)	$4\omega_c - 7\omega_o$ ($n = -7$)
1st	$4\theta_{\mathrm{c1}} + \theta_{\mathrm{o}}$	$-4\theta_{\mathrm{c1}} + \theta_{\mathrm{o}}$	$-4\theta_{\mathrm{c1}} - 5\theta_{\mathrm{o}}$	$4\theta_{\mathrm{c1}} - 5\theta_{\mathrm{o}}$	$4\theta_{\mathrm{c1}} + 7\theta_{\mathrm{o}}$	$-4\theta_{\mathrm{c1}} + 7\theta_{\mathrm{o}}$
2nd	$4\theta_{\mathrm{c2}} + \theta_{\mathrm{o}}$	$-4\theta_{\mathrm{c2}} + \theta_{\mathrm{o}}$	$-4\theta_{\mathrm{c2}} + 6\alpha - 5\theta_{\mathrm{o}}$	$4\theta_{\mathrm{c2}} + 6\alpha - 5\theta_{\mathrm{o}}$	$4\theta_{\mathrm{c2}} - 6\alpha + 7\theta_{\mathrm{o}}$	$4\theta_{\mathrm{c2}} - 6\alpha + 7\theta_{\mathrm{o}}$
	Harmonics Around $5\omega_c$ ($m = 5$)					
	$5\omega_c + 2\omega_o$ ($n = 2$)	$5\omega_c - 2\omega_o$ ($n = -2$)	$5\omega_c + 4\omega_o$ ($n = 4$)	$5\omega_c - 4\omega_o$ ($n = -4$)	$5\omega_c + 8\omega_o$ ($n = 8$)	$5\omega_c - 8\omega_o$ ($n = -8$)
1st	$-5\theta_{\mathrm{c1}} - 2\theta_{\mathrm{o}}$	$5\theta_{\mathrm{c1}} - 2\theta_{\mathrm{o}}$	$5\theta_{\mathrm{c1}} + 4\theta_{\mathrm{o}}$	$-5\theta_{\mathrm{c1}} + 4\theta_{\mathrm{o}}$	$-5\theta_{\mathrm{c1}} - 8\theta_{\mathrm{o}}$	$5\theta_{\mathrm{c1}} - 8\theta_{\mathrm{o}}$
2nd	$-5\theta_{\mathrm{c2}} + 3\alpha - 2\theta_{\mathrm{o}}$	$5\theta_{\mathrm{c2}} + 3\alpha - 2\theta_{\mathrm{o}}$	$5\theta_{\mathrm{c2}} - 3\alpha + 4\theta_{\mathrm{o}}$	$-5\theta_{\mathrm{c2}} - 3\alpha + 4\theta_{\mathrm{o}}$	$-5\theta_{\mathrm{c2}} + 9\alpha - 8\theta_{\mathrm{o}}$	$5\theta_{\mathrm{c2}} + 9\alpha - 8\theta_{\mathrm{o}}$
	Harmonics Around $6\omega_c$ ($m = 6$)					
	$6\omega_c + \omega_o$ ($n = 1$)	$6\omega_c - \omega_o$ ($n = -1$)	$6\omega_c + 5\omega_o$ ($n = 5$)	$6\omega_c - 5\omega_o$ ($n = -5$)	$6\omega_c + 7\omega_o$ ($n = 7$)	$6\omega_c - 7\omega_o$ ($n = -7$)
1st	$6\theta_{\mathrm{c1}} + \theta_{\mathrm{o}}$	$-6\theta_{\mathrm{c1}} + \theta_{\mathrm{o}}$	$-6\theta_{\mathrm{c1}} - 5\theta_{\mathrm{o}}$	$6\theta_{\mathrm{c1}} - 5\theta_{\mathrm{o}}$	$6\theta_{\mathrm{c1}} + 7\theta_{\mathrm{o}}$	$-6\theta_{\mathrm{c1}} + 7\theta_{\mathrm{o}}$
2nd	$6\theta_{\mathrm{c2}} + \theta_{\mathrm{o}}$	$-6\theta_{\mathrm{c2}} + \theta_{\mathrm{o}}$	$-6\theta_{\mathrm{c2}} + 6\alpha - 5\theta_{\mathrm{o}}$	$6\theta_{\mathrm{c2}} + 6\alpha - 5\theta_{\mathrm{o}}$	$6\theta_{\mathrm{c2}} - 6\alpha + 7\theta_{\mathrm{o}}$	$6\theta_{\mathrm{c2}} - 6\alpha + 7\theta_{\mathrm{o}}$

Table 4-1: PWM harmonic phase angles (In Radian) of the two three-phase subsystem voltage space vectors ($\vec{u}_{1,\mathrm{PWM}}(0)$ and $\vec{u}'_{2,\mathrm{PWM}}(0)$)

		PWM Harmonic Phase Angles under Different Frequencies (different values of m and n)					
		Harmonics Around ω_c $(m = 1)$					
		$\omega_c + 2\omega_o$ $(n = 2)$	$\omega_c - 2\omega_o$ $(n = -2)$	$\omega_c + 4\omega_o$ $(n = 4)$	$\omega_c - 4\omega_o$ $(n = -4)$	$\omega_c + 8\omega_o$ $(n = 8)$	$\omega_c - 8\omega_o$ $(n = -8)$
α=0	θ_{c2}-θ_{c1}= 0	0	0	0	0	0	0
	θ_{c2}-θ_{c1}= π	π	π	π	π	π	π
α=$\frac{\pi}{6}$	θ_{c2}-θ_{c1}= 0	$\frac{\pi}{2}$	$\frac{\pi}{2}$	$-\frac{\pi}{2}$	$-\frac{\pi}{2}$	$-\frac{\pi}{2}$	$-\frac{\pi}{2}$
	θ_{c2}-θ_{c1}= $\frac{\pi}{2}$	0	π	0	π	π	0
	θ_{c2}-θ_{c1}=$-\frac{\pi}{2}$	π	0	π	0	0	π
		Harmonics Around $2\omega_c$ $(m = 2)$					
		$2\omega_c + \omega_o$ $(n = 1)$	$2\omega_c - \omega_o$ $(n = -1)$	$2\omega_c + 5\omega_o$ $(n = 5)$	$2\omega_c - 5\omega_o$ $(n = -5)$	$2\omega_c + 7\omega_o$ $(n = 7)$	$2\omega_c - 7\omega_o$ $(n = -7)$
α=0	θ_{c2}-θ_{c1}= 0	0	0	0	0	0	0
	θ_{c2}-θ_{c1}= π	0	0	0	0	0	0
α=$\frac{\pi}{6}$	θ_{c2}-θ_{c1}= 0	0	0	π	π	π	π
	θ_{c2}-θ_{c1}= $\frac{\pi}{2}$	π	π	0	0	0	0
	θ_{c2}-θ_{c1}=$-\frac{\pi}{2}$	π	π	0	0	0	0

		$3\omega_c + 2\omega_o$ $(n = 2)$	$3\omega_c - 2\omega_o$ $(n = -2)$	$3\omega_c + 4\omega_o$ $(n = 4)$	$3\omega_c - 4\omega_o$ $(n = -4)$	$3\omega_c + 8\omega_o$ $(n = 8)$	$3\omega_c - 8\omega_o$ $(n = -8)$
		Harmonics Around $3\omega_c$ $(m = 3)$					
α=0	θ_{c2}-θ_{c1}= 0	0	0	0	0	0	0
	θ_{c2}-θ_{c1}= π	π	π	π	π	π	π
α=$\frac{\pi}{6}$	θ_{c2}-θ_{c1}= 0	$\frac{\pi}{2}$	$\frac{\pi}{2}$	$-\frac{\pi}{2}$	$-\frac{\pi}{2}$	$-\frac{\pi}{2}$	$-\frac{\pi}{2}$
	θ_{c2}-θ_{c1}= $\frac{\pi}{2}$	π	0	π	0	0	π
	θ_{c2}-θ_{c1}=$-\frac{\pi}{2}$	0	π	0	π	π	0
		Harmonics Around $4\omega_c$ $(m = 4)$					
		$4\omega_c + \omega_o$ $(n = 1)$	$4\omega_c - \omega_o$ $(n = -1)$	$4\omega_c + 5\omega_o$ $(n = 5)$	$4\omega_c - 5\omega_o$ $(n = -5)$	$4\omega_c + 7\omega_o$ $(n = 7)$	$4\omega_c - 7\omega_o$ $(n = -7)$
α=0	θ_{c2}-θ_{c1}= 0	0	0	0	0	0	0
	θ_{c2}-θ_{c1}= π	0	0	0	0	0	0
α=$\frac{\pi}{6}$	θ_{c2}-θ_{c1}= 0	0	0	π	π	π	π
	θ_{c2}-θ_{c1}= $\frac{\pi}{2}$	0	0	π	π	π	π
	θ_{c2}-θ_{c1}=$-\frac{\pi}{2}$	0	0	π	π	π	π
		Harmonics Around $5\omega_c$ $(m = 5)$					

		$5\omega_c + 2\omega_o$ ($n = 2$)	$5\omega_c - 2\omega_o$ ($n = -2$)	$5\omega_c + 4\omega_o$ ($n = 4$)	$5\omega_c - 4\omega_o$ ($n = -4$)	$5\omega_c + 8\omega_o$ ($n = 8$)	$5\omega_c - 8\omega_o$ ($n = -8$)
α=0	θ_{c2}-θ_{c1}= 0	0	0	0	0	0	0
	θ_{c2}-θ_{c1}= π	π	π	π	π	π	π
α=$\frac{\pi}{6}$	θ_{c2}-θ_{c1}= 0	$\frac{\pi}{2}$	$\frac{\pi}{2}$	$-\frac{\pi}{2}$	$-\frac{\pi}{2}$	$-\frac{\pi}{2}$	$-\frac{\pi}{2}$
	θ_{c2}-θ_{c1}=$\frac{\pi}{2}$	0	π	0	π	π	0
	θ_{c2}-θ_{c1}=$-\frac{\pi}{2}$	π	0	π	0	0	π
		Harmonics Around $6\omega_c$ ($m = 6$)					
		$6\omega_c + \omega_o$ ($n = 1$)	$6\omega_c - \omega_o$ ($n = -1$)	$6\omega_c + 5\omega_o$ ($n = 5$)	$6\omega_c - 5\omega_o$ ($n = -5$)	$6\omega_c + 7\omega_o$ ($n = 7$)	$6\omega_c - 7\omega_o$ ($n = -7$)
α=0	θ_{c2}-θ_{c1}= 0	0	0	0	0	0	0
	θ_{c2}-θ_{c1}= π	0	0	0	0	0	0
α=$\frac{\pi}{6}$	θ_{c2}-θ_{c1}= 0	0	0	π	π	π	π
	θ_{c2}-θ_{c1}=$\frac{\pi}{2}$	π	π	0	0	0	0
	θ_{c2}-θ_{c1}=$-\frac{\pi}{2}$	π	π	0	0	0	0

Table 4-2: PWM harmonic voltage space vector phase angle differences (In Radian) between the two three-phase subsystems (the difference between the phase angle of $\vec{u}_{1,\mathrm{PWM}}$ and the phase angle of $\vec{u}'_{2,\mathrm{PWM}}$)

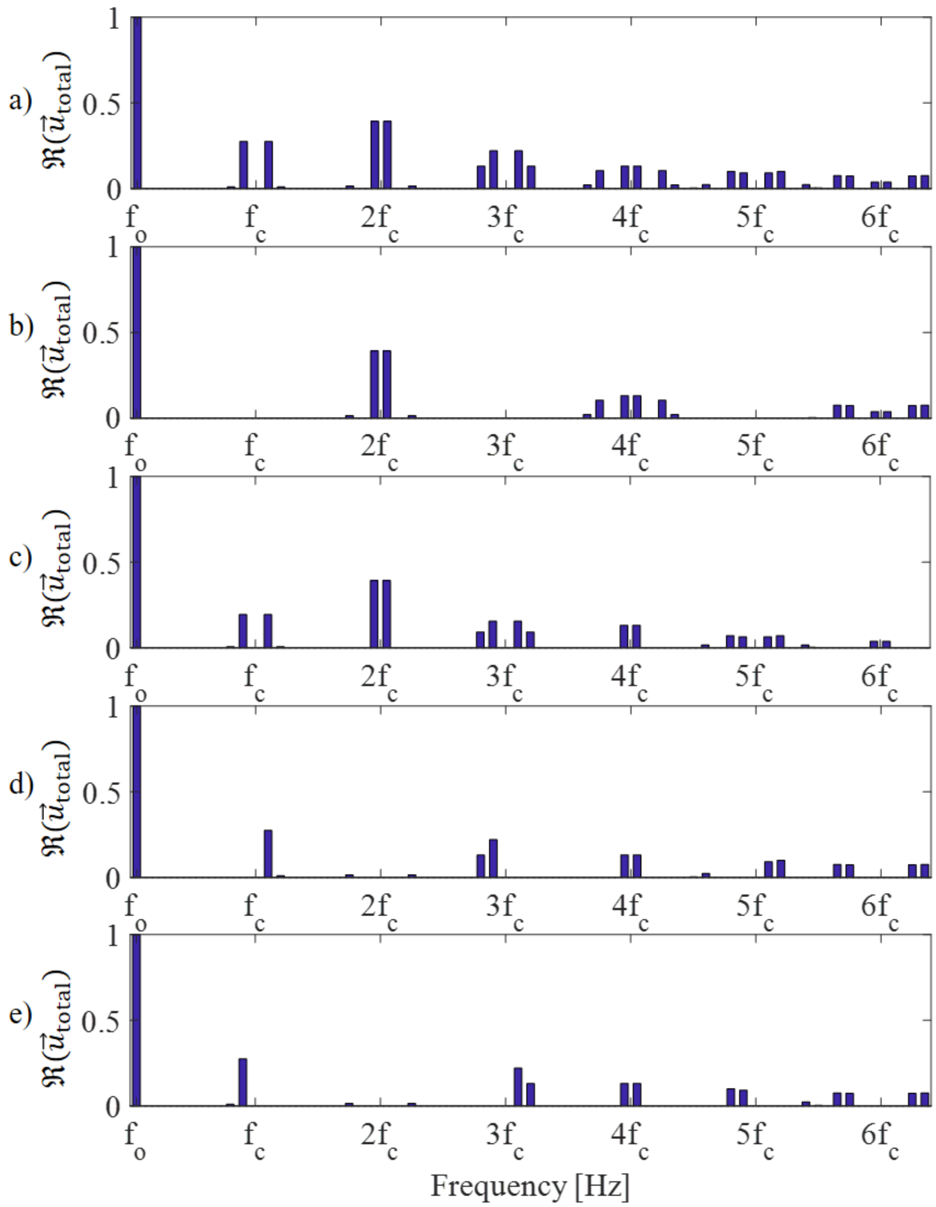

Figure 4-10: The FFT spectrums of the real part of the total voltage space vectors a) $\alpha = 0$ and $\theta_{c2} - \theta_{c1} = 0$ b) $\alpha = 0$ and $\theta_{c2} - \theta_{c1} = \pi$ c) $\alpha = \frac{\pi}{6}$ and $\theta_{c2} - \theta_{c1} = 0$ d) $\alpha = \frac{\pi}{6}$ and $\theta_{c2} - \theta_{c1} = \frac{\pi}{2}$ e) $\alpha = \frac{\pi}{6}$ and $\theta_{c2} - \theta_{c1} = -\frac{\pi}{2}$

4.4 Simulation results

4.4.1 Analytical, numerical and FEA results of the multi three-phase drive

A. Distributed dual three-phase drive

Analytical, numerical simulations have been obtained based on a distributed dual three-phase machine drive with the converter and machine paratermeters shown in Table 4-3. Analytical results are obtained using the time-varying equations (4-17) and (4-21) in MATLAB, which is shown in Appendix B. The numerical results are obtained by using variable-step simulations in PLECS. The numerical results are obtained at full load condition. The machine is operated at rated power of 160kW and rated speed of 20000rpm. The numerical results are used to validate the analytical model described by (4-17) and (4-21).

Figure 4-11, Figure 4-12 and Figure 4-13 show the phase voltage, phase current and electromagnetic torque waveforms and their corresponding FFT spectra of the dual three-phase machine in both analytical and numerical results. According to Figure 4-11, Figure 4-12 and Figure 4-13, the analytical results match with numerical results in general. The phase voltage waveforms of Figure 4-11a and Figure 4-11b are slightly different, as the numerical result is obtained with infinite number of carrier signal index m and infinite number of modulating signal index n. However, the analytical result is obtained with limited number of carrier signal index m (m=10) and limited number of modulating signal index n (n=10) in MATLAB. This means that the higher order phase voltage harmonic components are not considered in the analytical results. The lower order phase voltage harmonic components in the analytical result match with harmonic components in the numerical result, which is shown in Figure 4-11c and Figure 4-11d. There is no obvious difference between Figure 4-12a (Figure 4-13a) and Figure 4-12b (Figure 4-13b), as the phase currents (electromagnetic torque) are generated by phase voltages through low pass filters, mentioned in Section 3.2.2, which indicates that the higher order phase voltage harmonic components have less effect on the phase currents and electromagnetic torque.

Parameter	**Value**
DC link voltage (V_{dc})	500 [V]
Switching frequency (f_c)	20 [kHz]
Modulating frequency (f_o)	1 [kHz]
Rated power	160 [kW]
Rated current	280 [A]
Pole pair number	3
Phase resistance (R)	11.47 [mΩ]
mechanical speed (ω_m)	20000 [rpm]
stator phase inductance	25 [µH]
back-EMF coefficient (K_E)	0.12 (phase peak back-EMF is 248V at 1000Hz)

Table 4-3: Converter and machine parameters

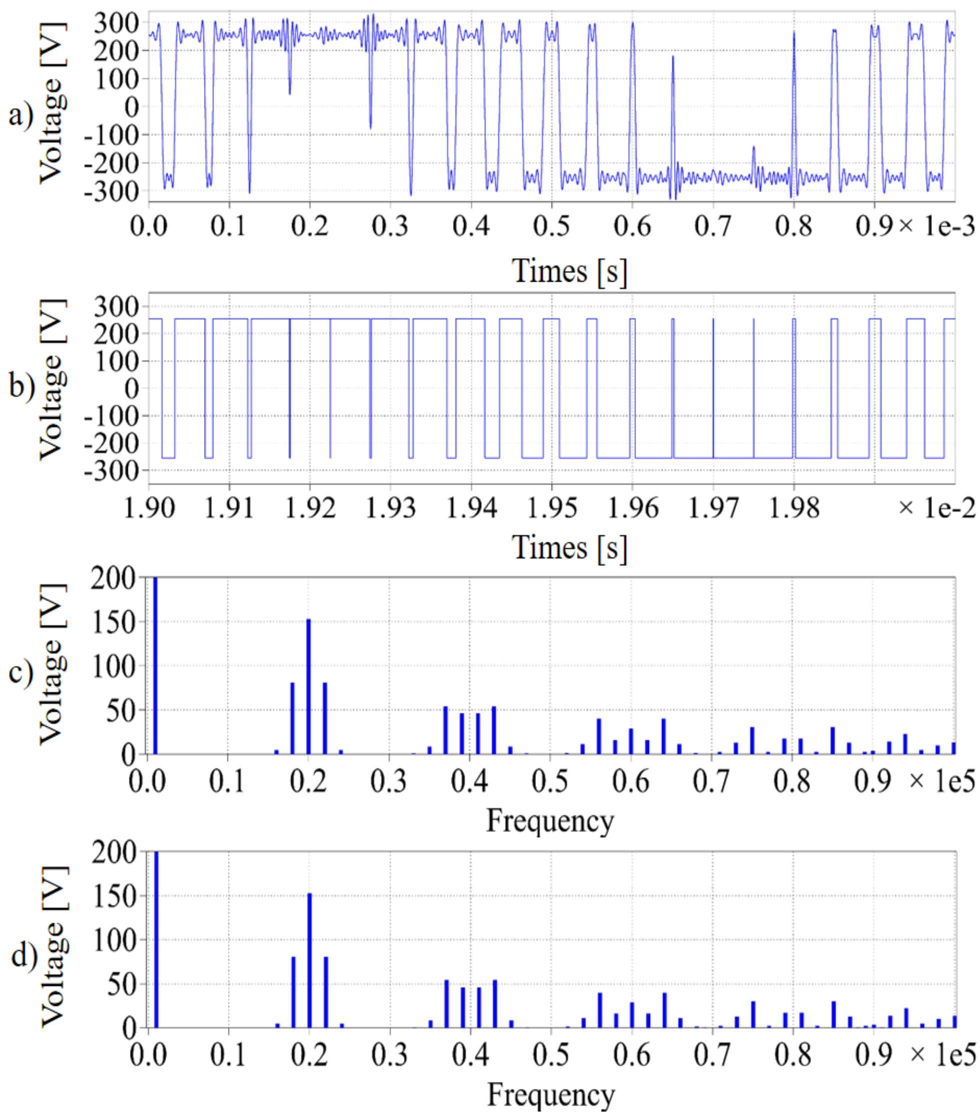

Figure 4-11: a) & b) Phase voltage waveform a) analytical result b) numerical result c) & d) Phase voltage spectra c) analytical result d) numerical result

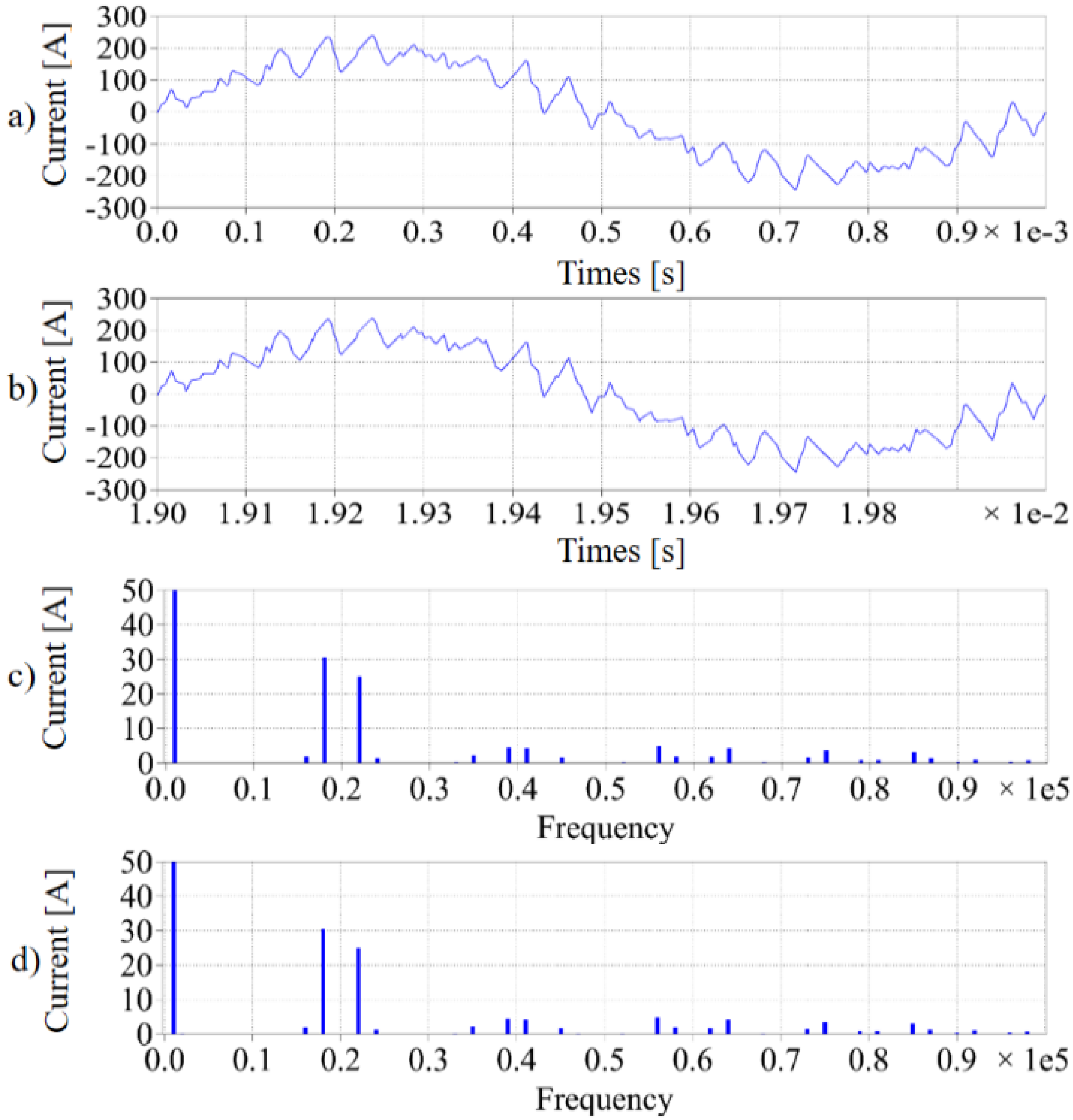

Figure 4-12: a) & b) Phase current waveform a) analytical result b) numerical result c) & d) Phase current spectra c) analytical result d) numerical result

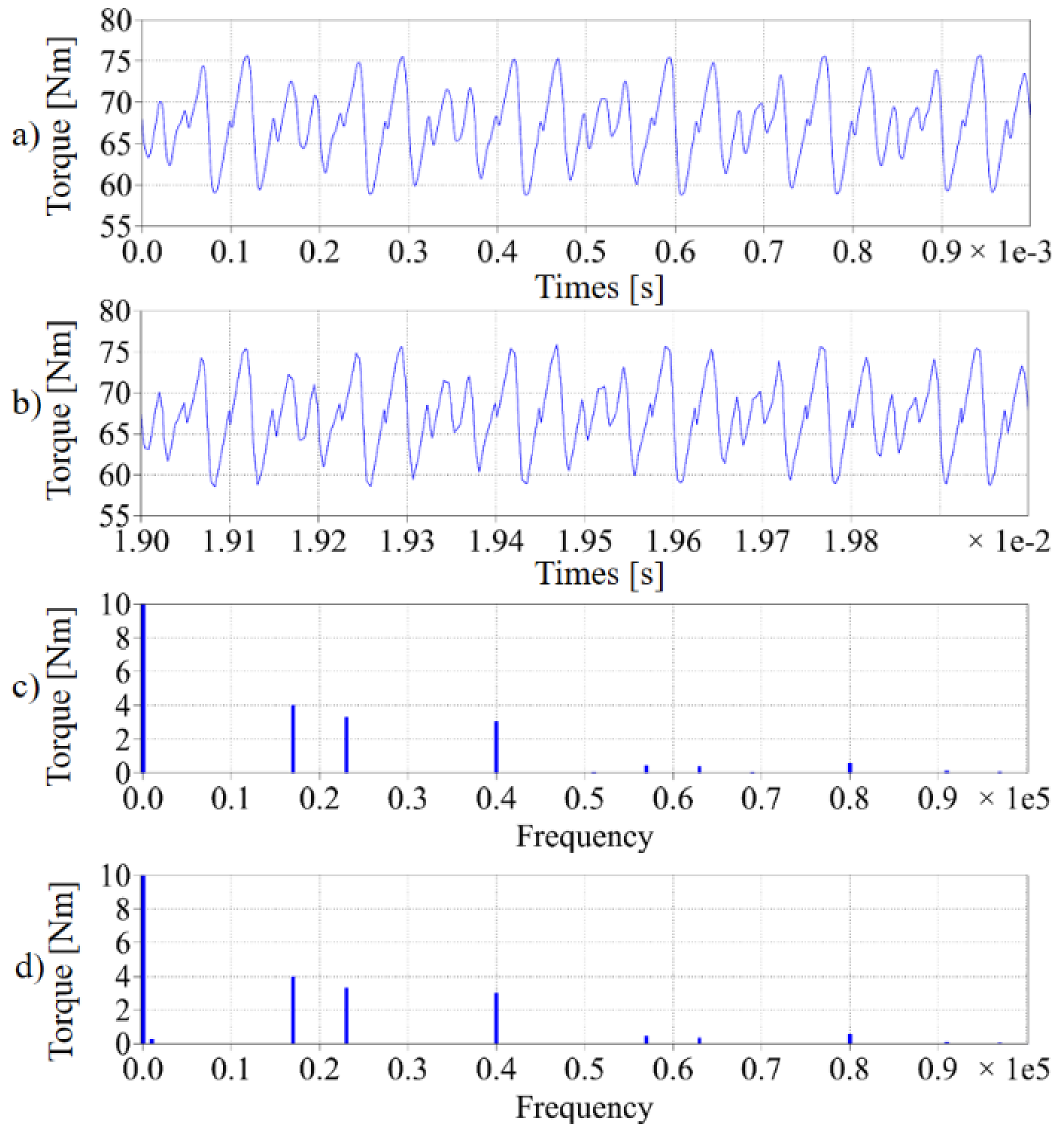

Figure 4-13: a) & b) Electromagnetic torque waveform a) analytical result b) numerical result c) & d) Electromagnetic torque spectra c) analytical result d) numerical result

B. Sectored triple three-phase drive

Analytical, numerical and FEA simulations have been carried based on a sectored triple three-phase machine drive with the converter and machine parameters shown in Table 4-4. The cross section of the triple three-phase PM machine is shown in Figure 4-6. Analytical results are obtained using the time-varying equations (4-17) and (4-21) in MATLAB, which is shown in Appendix C. The numerical results are obtained by using variable-step simulations in PLECS, which is shown in Appendix D. The operating condition concerning the numerical results is no load condition. There is no external load on the machine and the machine operating power is to overcome the mechanical (friction) power loss and the electromagnetic power loss of the machine itself. FEA results are finally realized by Magnet with the triple three-phase machine model (Figure 4-14) excited by the currents resulting from the PLECS simulation. The numerical and FEA results are used to validate the analytical model described by (4-17) and (4-21), and quantify the phase current and torque ripple with and without CPS-PWM. The proposed carrier phase angles used in this case are $\theta_{c,1} = 0$, $\theta_{c,2} = \frac{2\pi}{3}$ and $\theta_{c,3} = \frac{4\pi}{3}$ for sector 1, sector 2 and sector 3 respectively.

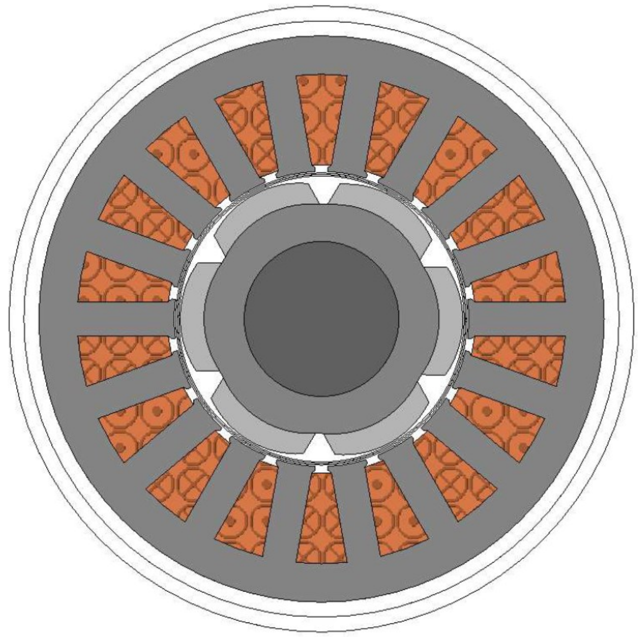

Figure 4-14: Sectored triple three-phase PM machine model in Magnet

Parameter	**Value**
DC voltage (V_{dc})	60 [V]
Switching frequency (f_c)	2 [kHz]
Modulating frequency (f_o)	50 [Hz]
Pole pair number	3
Power rating of the machine	1.5 [kW]
Rated torque of the machine	5 [Nm]
Rated current of the machine	11.5 [Apk]
Rated voltage of the machine	28.5 [Vpk]
Phase resistance (R)	0.08 [Ω]
Stator inductance matrix($\boldsymbol{L}$)	L=0.31; M_1= 0.087; M_2= 0.03; M_3= 0.029 [mH]
Mechanical speed (ω_m)	104.72 [rad/s] (1000rpm)
Back-EMF coefficient (K_E)	0.085 (phase peak back-EMF is 8.9V at 50Hz)

Table 4-4: Converter and Machine Parameters [102]

Figure 4-15 shows the block diagram for the control of the nine-phase machine fed by its three independent PWM converters. The CPS-PWM method is applied to the three three-phase systems with carrier phase shift angles $\theta_{c,1}$, $\theta_{c,2}$, and $\theta_{c,3}$ respectively. The machine in the PLECS simulations (numerical results) is controlled in speed, by a simple proportional-integral (PI) controller which provides the same current reference (iq) as input to the internal current PI regulator of each three-phase system.

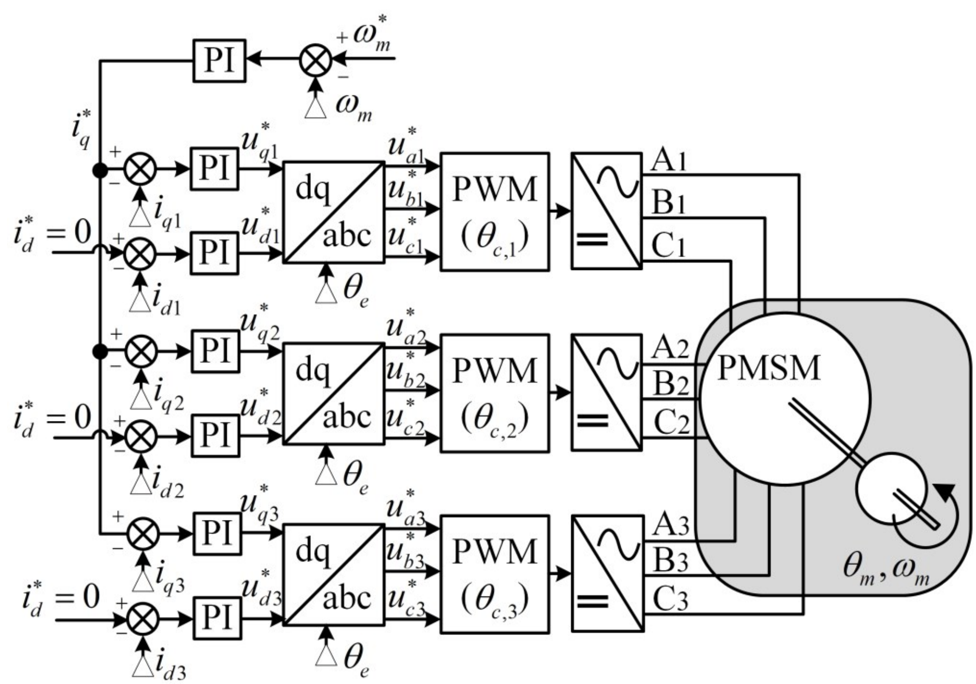

Figure 4-15: Block diagram of simulation model [102]

Figure 4-16 shows the comparison of the analytical and numerical models in terms of phase current (phase A_1 is considered). Figure 4-16a and Figure 4-16c show the analytical and numerical results without applying CPS-PWM method. Figure 4-16b and Figure 4-16d show the same while applying the CPS-PWM method. Figure 4-16d shows that there is slightly difference between the analytical and numerical results at the groups of harmonics around 2 kHz, 4 kHz, 8 kHz, 10 kHz, 14 kHz and 16 kHz. The reason is that the analytical

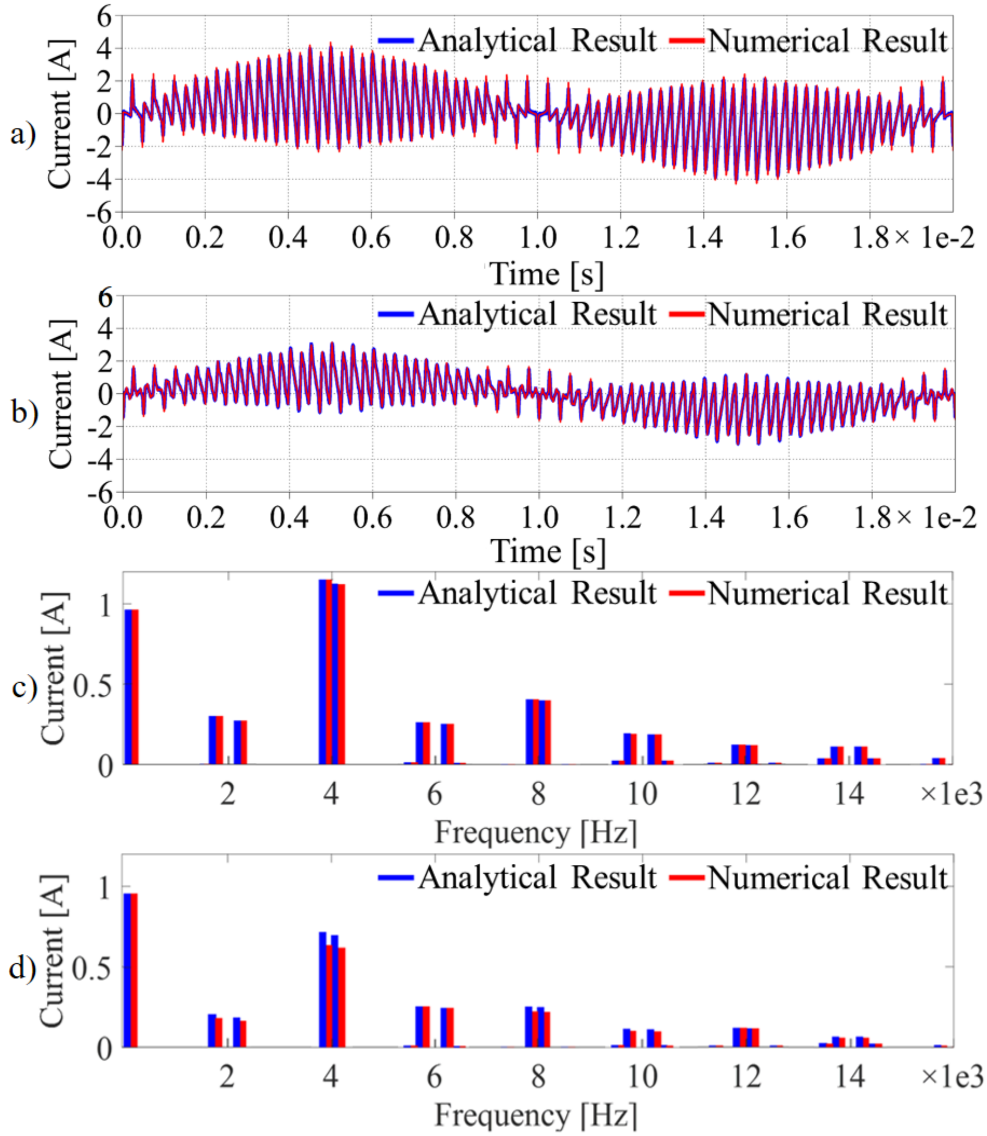

Figure 4-16 a) & b) Analytical and numerical results of phase A1 current waveform a) without CPS-PWM b) with CPS-PWM c) & d) Analytical and numerical results of phase A1 current FFT spectrum c) without CPS-PWM d) with CPS-PWM [102].

model is based on a simplification of the system considering the equations in electrical degrees for phase A_p, B_p and C_p ($p \in \{1, 2, 3\}$) independent from the sector where they are placed. In this machine, due to the sectored stator winding structure, applying CPS-PWM in numerical model will lead to small harmonic phase current difference among phase A_p, B_p and C_p in each sector, which is explained in Chapter 5.

Figure 4-17 shows the comparison of analytical, numerical and FEA models in terms of the machine electromagnetic torque. Figure 4-17(a-d) show that the analytical results match with the numerical results for both without and with applying CPS-PWM. Figure 4-17(a-b) show that the FEA results match with the analytical and numerical results with a good approximation considering for the analyzed ripple. Figure 4-17(c-d) show that there are low order harmonics (6^{th} at 300Hz， 12^{th} at 600Hz) in FEA results, which are not shown in analytical and numerical results. One reason is that only fundamental component of back-EMF is considered in analytical and numerical models, which has been mentioned in Section 4.2. In the FEA machine model, the interaction between the fundamental component of winding field and the 5^{th}, 7^{th}, 11^{th}, 13^{th}…permanent magnet harmonics results in the 6^{th}, 12^{th}…harmonics of the torque ripple. The other reason is that the machine model in Magnet is a 6 poles, 18 slots PMSM, and the interaction between the permanent magnet rotor and stator slots generate 6^{th}, 12^{th}…harmonics in the torque caused by the cogging effect. In addition, Figure 4-17 (c-d) show that the FEA result presents slightly higher amplitudes compared with analytical and numerical results, this is due to machine parameter uncertainties in the model, for example the changes of them with working operation due to saturations and non-linear effects.

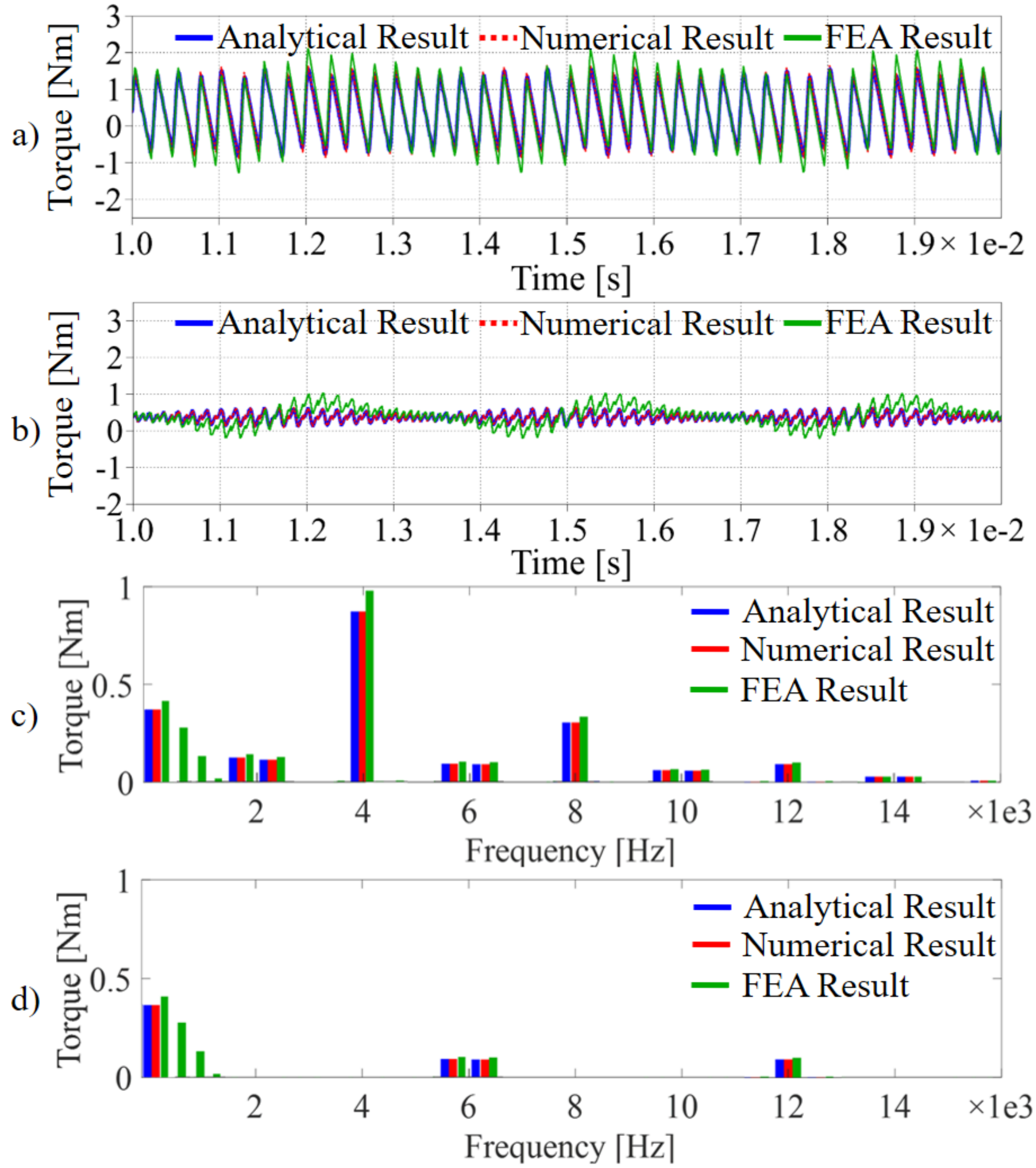

Figure 4-17: a) & b) Analytical, numerical and FEA results of torque waveform a) without CPS-PWM b) with CPS-PWM c) & d) Analytical, numerical and FEA results of torque FFT spectrum c) without CPS-PWM d) with CPS-PWM [102].

Comparing the torque waveform with and without CPS-PWM, Figure 4-17 (a-b) show that the peak-to-peak torque are reduced by 79.5%, 78.5% and 63.8% with applying CPS-PWM in analytical, numerical and FEA results respectively. Figure 4-17s (c-d) show that the harmonic components of the torque FFT spectrum around 2 kHz, 4 kHz, 8 kHz, 10 kHz, 14 kHz and 16 kHz obtained by applying CPS-PWM are effectively cancelled out in analytical, numerical and FEA results.

4.4.2 Selective torque harmonic elimination method validation by numerical results

In order to validate the effect of applying different carrier phase shift angles to the dual three-phase drives to eliminate the selective torque harmonics, simulation models of the PM machine with two different stator winding configurations ($\alpha = 0$ and $\alpha = \frac{\pi}{6}$) are established in PLECS. The machine stator winding configuration is changed by the external connection box shown in Figure 4-26. The stator winding layout of the dual three-phase PMSM is shown in Appendix E. The connection circuits of $\alpha = 0$ and $\alpha = \frac{\pi}{6}$ are shown in Figure 4-18a and Figure 4-18b respectively. The machine parameters under the two different winding configurations ($\alpha = 0$ and $= \frac{\pi}{6}$) are shown in Table 4-5.

a)
b)

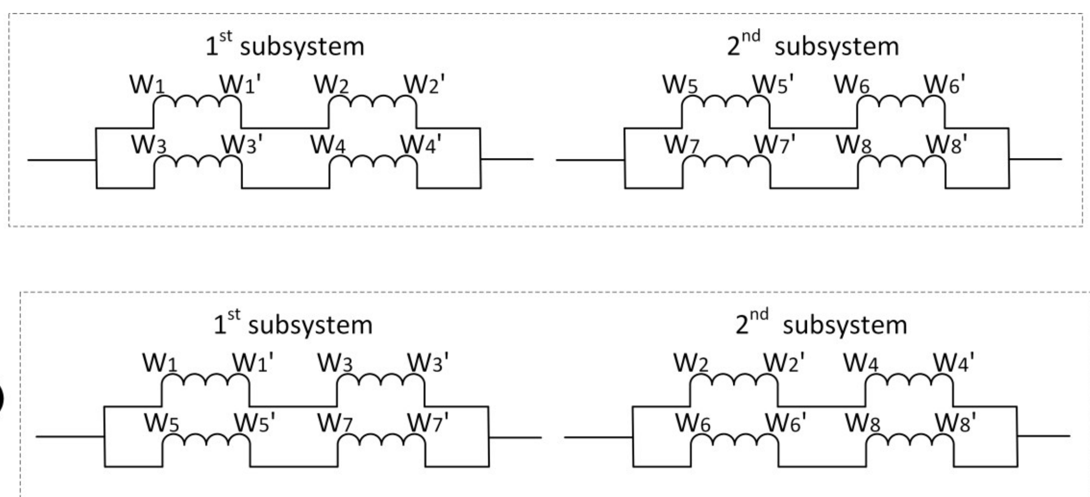

Figure 4-18: Connection circuits of dual three-phase PM machines

Parameter	Value
Rated power (α=0 and $\alpha=\frac{\pi}{6}$)	18 [kw]
Rated current (α=0 and $\alpha=\frac{\pi}{6}$)	71 [Apk]
Rated voltage (α=0 and $\alpha=\frac{\pi}{6}$)	312 [Vpk]
Rated speed (α=0 and $\alpha=\frac{\pi}{6}$)	3000 [rpm]
Pole pair number (α=0 and $\alpha=\frac{\pi}{6}$)	4
Phase resistance (α=0 and $\alpha=\frac{\pi}{6}$)	8.5 [mΩ]
Back-EMF coefficient K_E (α=0)	0.2506 (phase peak back-EMF is 9.84V at 25Hz)
Back-EMF coefficient K_E ($\alpha=\frac{\pi}{6}$)	0.1846 (phase peak back-EMF is 7.25V at 25Hz)
Stator inductance matrix $\boldsymbol{L}$ (α=0)	L =0.248; M_0 = -0.099; M_1 = -0.099; M_2= 0.032; M_3= 0.032 [mH]
Stator inductance matrix $\boldsymbol{L}$ ($\alpha=\frac{\pi}{6}$)	L =0.166; M_0 = -0.066; M_1 = 0.066; M_2= -0.066; M_3= 0 [mH]

Table 4-5: Parameters of the two machines

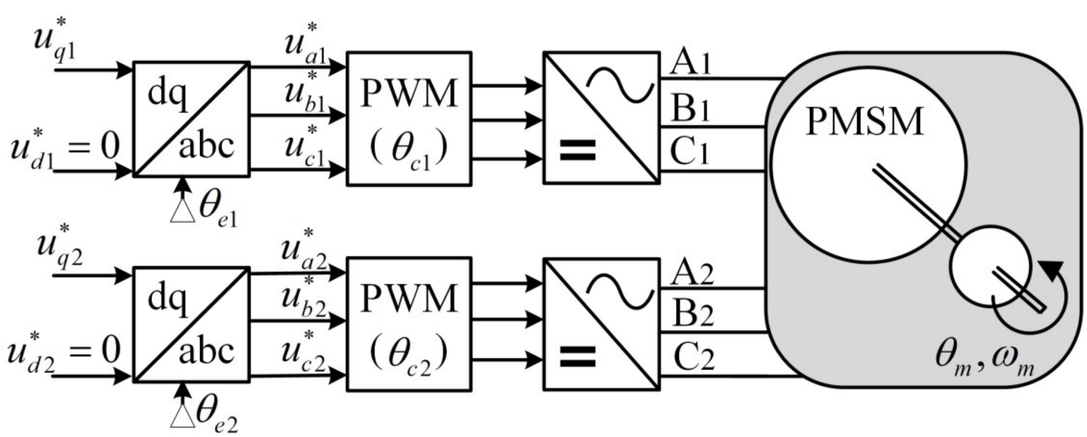

Figure 4-19: Block diagram of simulation model/experimental set-up.

The simulation model in PLECS is a voltage open loop control used for validating the proposed control technique without interfering with the use of current PI regulators, which might affect the voltage and current waveforms. The corresponding control block diagram is shown Figure 4-19. The carrier phase shift angles θ_{c1} and θ_{c2} are applied to the first and the second three-phase systems respectively. The switching frequency of each converter is f_c=1 kHz. The machine speed of the two winding configurations ($\alpha = 0$ and $= \frac{\pi}{6}$) is fixed to 375 rpm (i.e., a fundamental frequency f_o= 25 Hz) by keeping the product of the DC link voltage and the modulation index (V_{dc} and M) as a constant. The simulated condition is a low load operation of the motor at 6Nm output torque.

As it is expressed in (4-26), the modulation index (M) affects the amplitudes of PWM harmonic components, which means the improvement of torque performance with CPS-PWM varies with the modulation index. Figure 4-20 shows the peak to peak torque ripple reduction obtained with the proposed CPS-PWM under different modulation indexes of both winding configurations ($\alpha = 0$ and $\alpha = \frac{\pi}{6}$). The peak to peak torque ripple with the proposed CPS-PWM ($\theta_{\mathrm{c2}} - \theta_{\mathrm{c1}} = \pi$) is reduced by 67% under the modulation index M=1 for winding configuration 1 ($\alpha = 0$). The peak to peak torque ripple applying the proposed CPS-PWM ($\theta_{\mathrm{c2}} - \theta_{\mathrm{c1}} = \pm\frac{\pi}{2}$) is reduced by 65% under the modulation index M=0.6.

Figure 4-21 shows the torque waveforms and their corresponding FFT spectra with winding configuration $\alpha = 0$ and modulation index M=0.8. Comparing Figure 4-21c and Figure 4-21d, the torque harmonic groups around 1 kHz, 3 kHz, 5 kHz are effectively cancelled out using the CPS-PWM. Comparing Figure 4-21a and Figure 4-21b, the peak to peak torque ripple is reduced by 49% applying CPS-PWM.

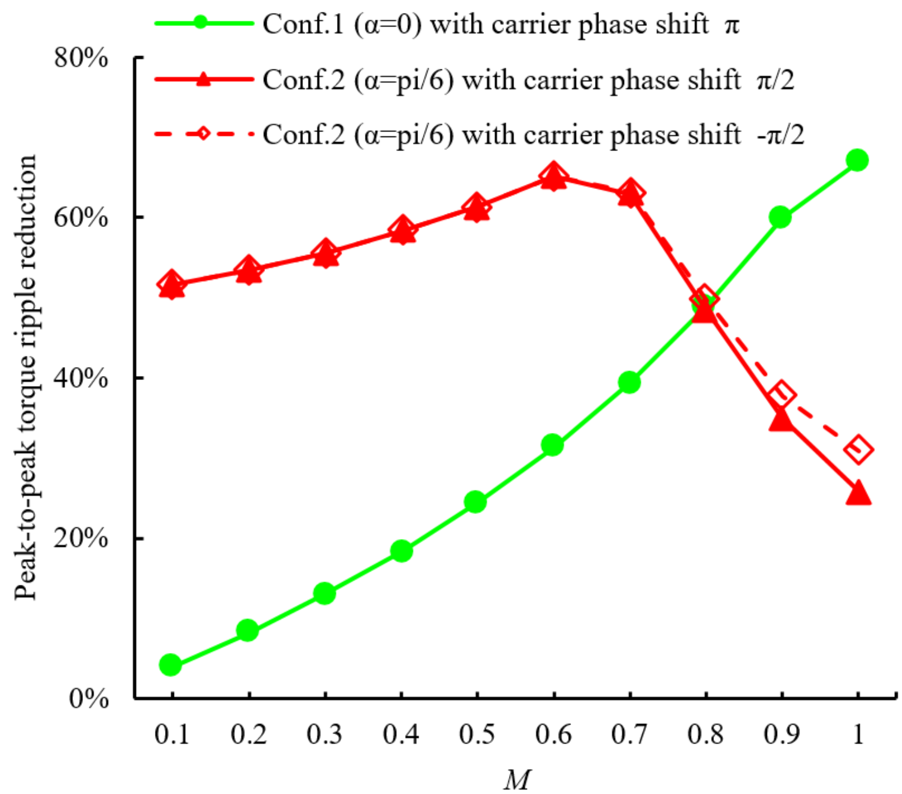

Figure 4-20: Peak to peak torque ripple reduction with applying the proposed CPS-PWM under different modulation index of winding configurations $\alpha = 0$ and $\alpha = \frac{\pi}{6}$.

Figure 4-22 shows the torque waveforms and their corresponding FFT spectra for the same simulation of with winding configuration $\alpha = \frac{\pi}{6}$ and modulation index M=0.3. Comparing Figure 4-22d and Figure 4-22e, the harmonic components at 0.925 kHz, 2 kHz, 3.075 kHz, and 4.925 kHz are effectively eliminated applying the CPS-PWM ($\theta_{c2} - \theta_{c1} = \frac{\pi}{2}$). Comparing Figure 4-22d and Figure 4-22f, the harmonic components at 1.075 kHz, 2 kHz, 2.925 kHz, and 5.075 kHz are effectively eliminated applying the CPS-PWM ($\theta_{c2} - \theta_{c1} = -\frac{\pi}{2}$). Comparing Figure 4-22a, Figure 4-22b and Figure 4-22c, the peak to peak torque ripple is reduced by 56% applying the CPS-PWM ($\theta_{c2} - \theta_{c1} = \pm\frac{\pi}{2}$).

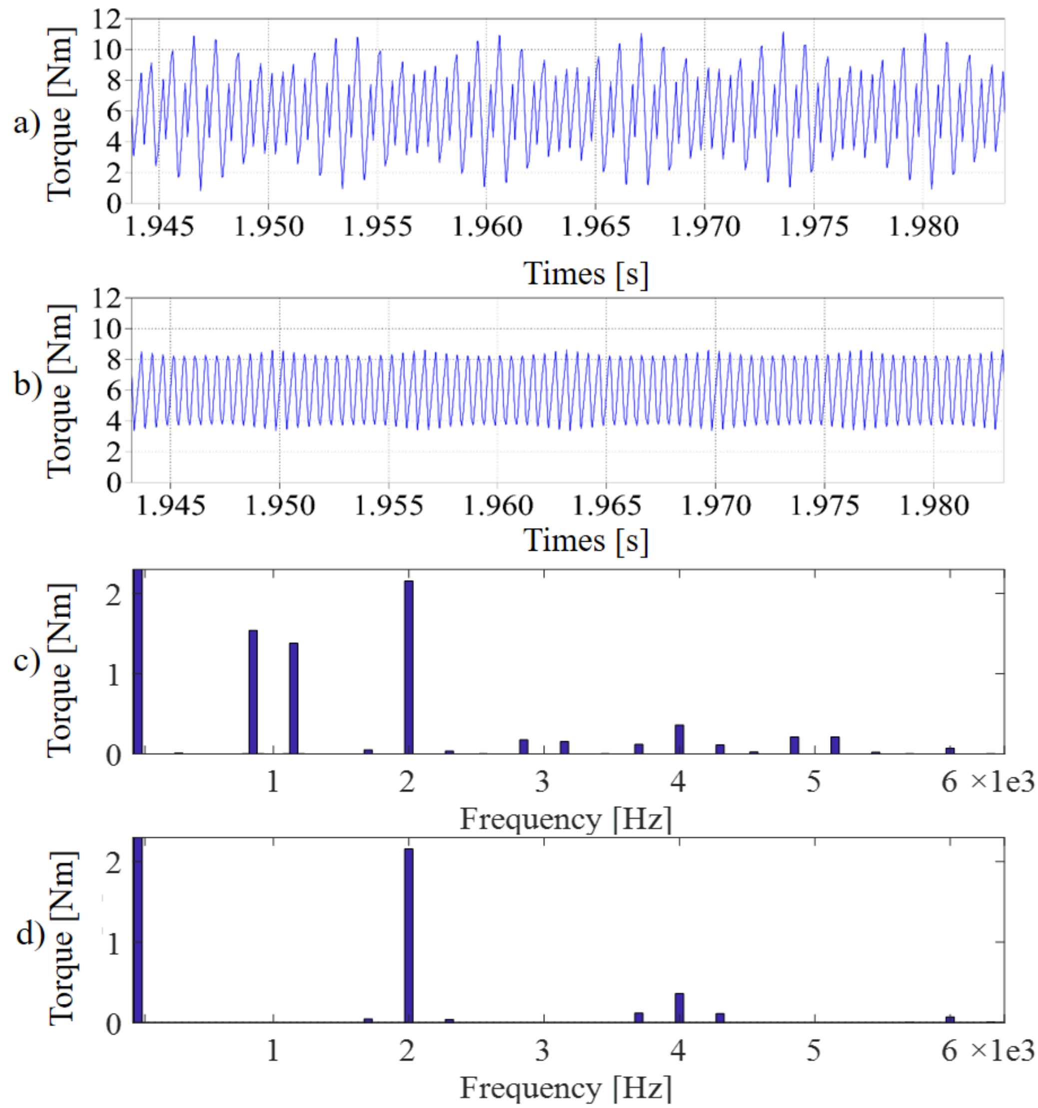

Figure 4-21: a) & b) Simulation results of torque waveforms of winding configuration $\alpha = 0$ a) without CPS-PWM, $\theta_{c2} - \theta_{c1} = 0$ b) with CPS-PWM, $\theta_{c2} - \theta_{c1} = \pi$ c) & d) Simulation results of torque FFT spectrums of winding configuration $\alpha = 0$ c) without CPS-PWM, $\theta_{c2} - \theta_{c1} = 0$ d) with CPS-PWM, $\theta_{c2} - \theta_{c1} = \pi$

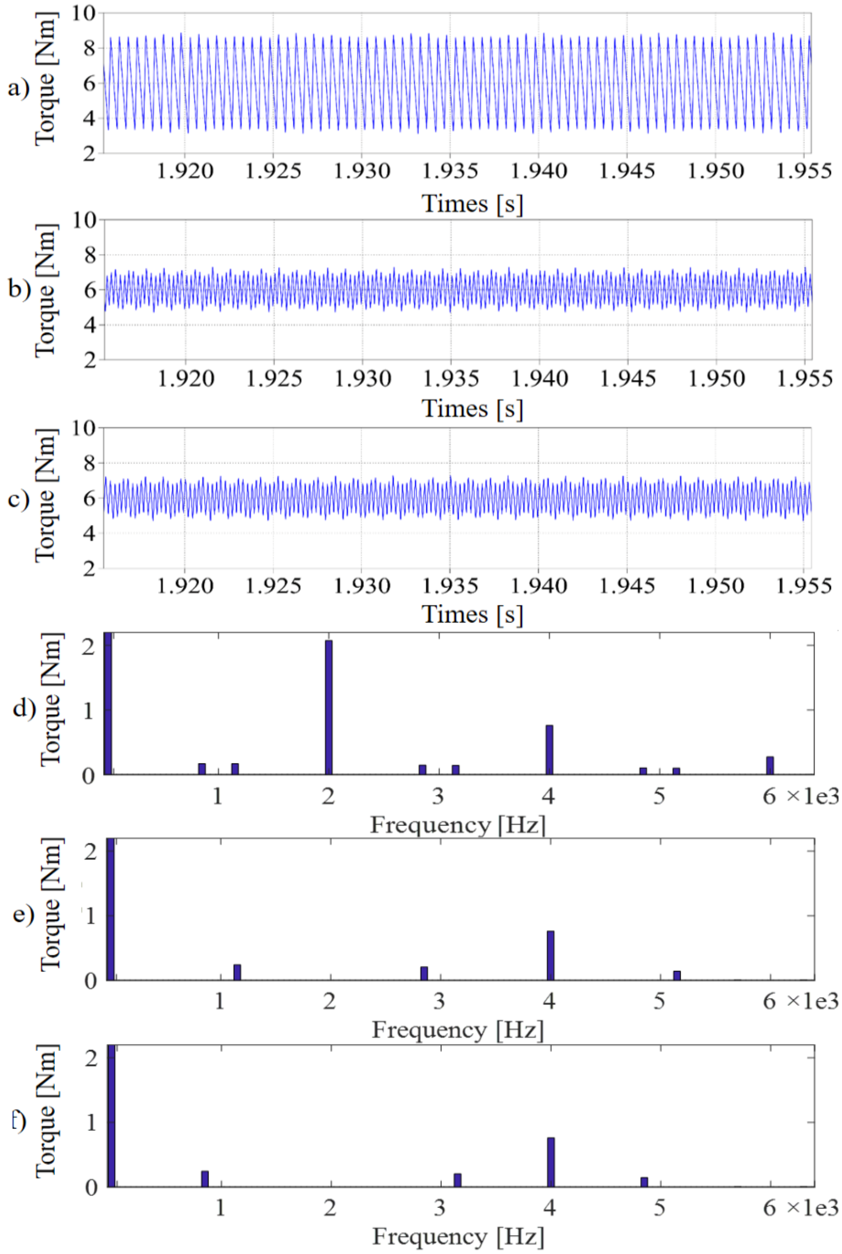

Figure 4-22: a) & b) & c) Simulation results of torque waveforms of winding configuration $\alpha = \frac{\pi}{6}$ a) without CPS-PWM, $\theta_{c2} - \theta_{c1} = 0$ b) with CPS-PWM, $\theta_{c2} - \theta_{c1} = \frac{\pi}{2}$ c) with CPS-PWM, $\theta_{c2} - \theta_{c1} = -\frac{\pi}{2}$ d) & e) & f) Simulation results of torque FFT spectrums of winding configuration $\alpha = \frac{\pi}{6}$ d) without CPS-PWM, $\theta_{c2} - \theta_{c1} = 0$ e) with CPS-PWM, $\theta_{c2} - \theta_{c1} = \frac{\pi}{2}$ f) with CPS-PWM, $\theta_{c2} - \theta_{c1} = -\frac{\pi}{2}$.

4.5 Experimental results

4.5.1 Experimental of results of the triple three-phase drive

In order to validate the analytical model and the simulation results for the sectored triple three-phase drive, experimental tests have been carried out by means of the platform shown in Figure 4-23. The parameters and the control algorithm used in the experimental platform is the one explained in Section 4.4.1. The operating condition concerning the experimental results (same as the numerical results) is no load condition. There is no external load and the machine operating power is to overcome the mechanical (friction) power loss and the electromagnetic power loss of the machine itself. The experimental setup consists of triple three-phase inverters with standard IGBT modules, a sectored triple three-phase PMSM with its cross section shown in Figure 4-6, and a centralized controller (uCube [103]). Optical fiber is used to communicate between the power module gate drives and the uCube.

Only the fundamental component of the back-EMF while calculating the equivalent electromagnetic torque through phase current is considered. The main torque ripple analyzed in this case is due to the interaction of the high order winding field harmonics with the fundamental component of the permanent magnet field. The torque ripple caused by the interaction of the high order harmonics (5^{th}, 7^{th}, 11^{th}, 13^{th} …) is neglected. In the FEA model, the back-EMF with the fundamental component and all its harmonic components are considered to obtain the electromagnetic torque. In the analytical and the numerical models, only the fundamental component of the back-EMF is considered to obtain the electromagnetic

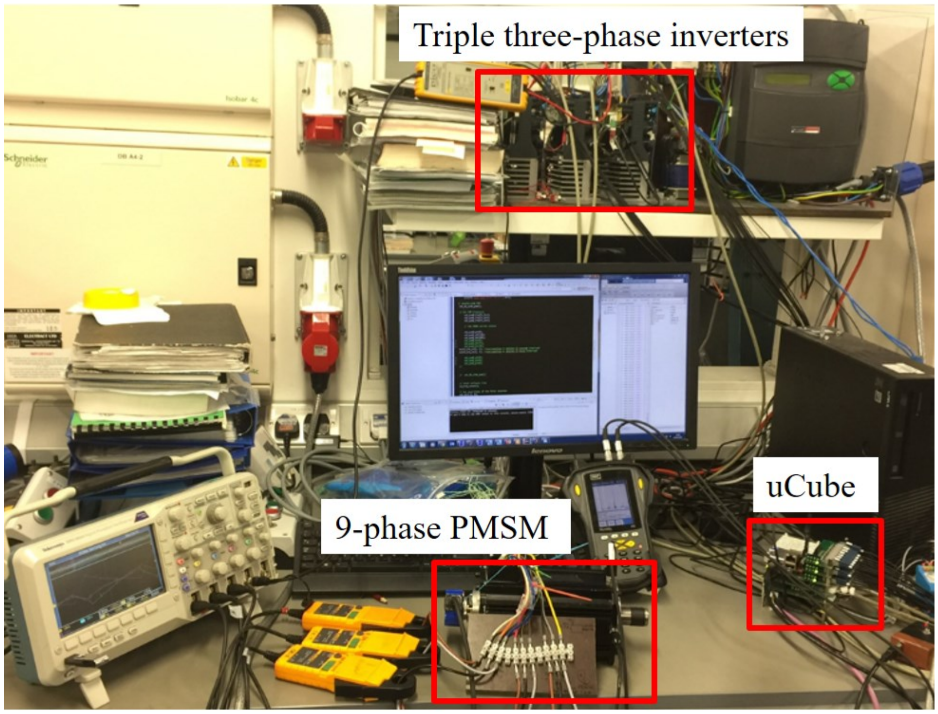

Figure 4-23: Triple three-phase machine drive system experimental set-up [102].

torque. Therefore, the effect of considering only the fundamental component can be seen by comparing the analytical results (numerical results) with the FEA results. As it is shown in Figure 4-17, the FEA results match with the analytical results (numerical results) with a good approximation. Figure 4-17(c-d) show that there are some low order harmonic components in the FEA results, and the amplitudes of the high order harmonic components in the FEA results are slightly different with the numerical results (analytical results). Further research work needs to be done with more accurate models to obtain the match of the electromagnetic torque in the analytical, numerical and experimental results.

The equivalent electromagnetic torque are calculated through measuring the phase currents from current probes. The torque waveforms are not directly measured through torque meters, due to the bandwidth limitation of commercial torque meters. In this case, the torque waveforms are analyzed with high frequencies (up to 20 kHz), which means a very high resolution torque meter with wide bandwidth is required if we want to measure the torque waveform directly. However, even wide bandwidth commercial torque meters cannot meet the bandwidth requirement of 20 kHz. Therefore, an alternative approach of measuring the phase currents using current probes is adopted. The equivalent electromagnetic torque is calculated by the experimental phase currents based on (4-17) and (4-21). The results of torque waveforms among analytical, numerical and FEA results in Figure 4-17 have validated the feasibility of using this method to obtain the equivalent electromagnetic torque waveform.

The equivalent electromagnetic torque waveforms and their corresponding FFT spectrum with and without CPS-PWM, are shown in Figure 4-24. Comparing the torque waveform with and without CPS-PWM, Figure 4-24a shows that the peak-to-peak torque is reduced by 58.3% with applying CPS-PWM. The experimental torque ripple reduction of 58.3% is smaller than the analytical (numerical, FEA) results, but it still represents a major improvement compared to the control without CPS-PWM. Figure 4-24b shows that the harmonic components of the torque FFT spectrum around 2 kHz, 4 kHz, 8 kHz, 10 kHz, 14 kHz obtained by applying CPS-PWM are effectively cancelled out.

The experimental torque reduction of 58.3% is smaller than the analytical torque ripple reduction of 79.5%, the numerical torque ripple reduction of 78.5% and the FEA torque ripple reduction of 63.8%. There are mainly six reasons for these differences:

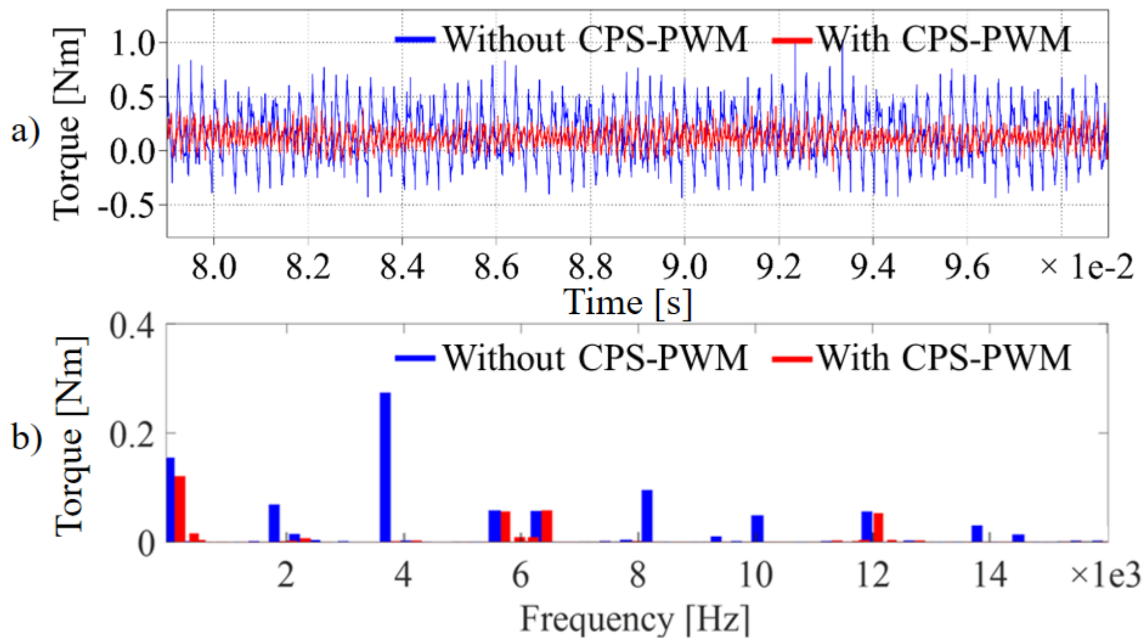

Figure 4-24: Experimental results of equivalent electromagnetic torque waveform with and without CPS-PWM b) FFT spectrum of equivalent electromagnetic torque waveform with and without CPS- PWM [102].

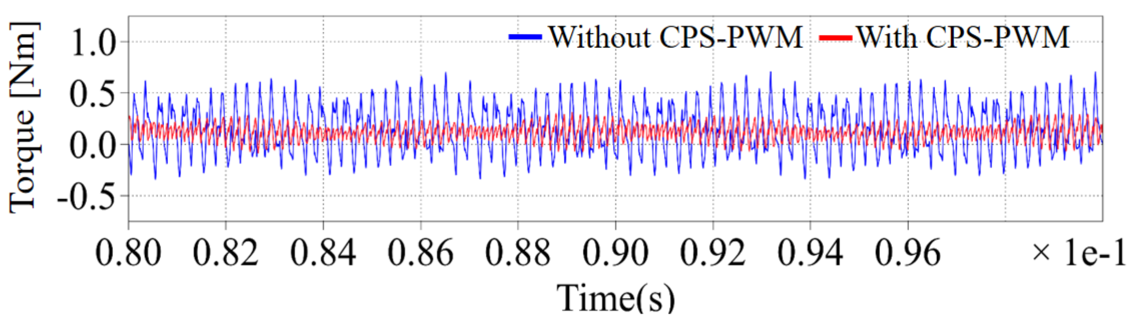

Figure 4-25: Experimental results (With low-pass filter) of equivalent electromagnetic torque waveform with and without CPS-PWM

:

- For the numerical, the analytical and the FEA results, the commutation noise of the inverters is not considered. For the experimental results, the commutation noise generates the torque peaks. This is confirmed when there is a weak low-pass filter (the cutoff frequency of the low-pass filter is 100 kHz, 50 times higher than the switching frequency, so that it only affects the switching noise but does not change the shape of the current) applied to the experimental phase currents, the situation of the corresponding electromagnetic torque ripple reduction is improved. Figure 4-24a and Figure 4-25 show the electromagnetic torque waveform without and with adding the low-pass filter respectively. Figure 4-24a shows that the peak-to-peak torque (without low-pass filter) is reduced by 58.3% with applying CPS-PWM. Figure 4-25 shows that the peak-to-peak torque (with low-pass filter) is reduced by 62.9% with applying CPS-PWM.
- For the analytical and numerical results, the main torque ripple caused by the PWM is due to the interaction of the high order winding field harmonics with the fundamental component of the permanent magnet field. For the FEA and the experimental results, besides the fundamental component of the permanent magnet field, the torque ripple is influenced by the high order harmonics (back-EMF distortion). Though the equivalent electromagnetic torque in the experimental results are the calculated with considering only the fundamental component of the back-EMF, the back-EMF distortion influence the experimental phase currents.
- For the analytical and the numerical results, the machine is modelled without considering the interaction between the permanent magnet rotor and the stator slots (cogging effect). For the FEA and the experimental results, the interaction between

the permanent magnet rotor and the stator slots (cogging effect) generate 6^{th}, 12^{th}…harmonics in the torque.

- For the analytical and the numerical results, the machine is modelled with constant machine parameters. For the FEA and the experimental results, there is machine parameter uncertainties, for example the changes of the machine parameters with working operation due to saturations and non-linear effects.
- For the analytical and numerical results, the inverters are analyzed with linear mathematical models. The FEA results are realized with the machine model excited by the currents resulting from the PLECS simulation (numerical results), therefore the inverters are analysed with linear mathematical models for the FEA results. For the experimental results, the inverters' non-linearity affects the experimental results.
- The analytical results, the numerical results and the FEA results are realized without the consideration of the dead time effect. The experimental results are effected by the dead time effect.

In summary, the experimental torque ripple reduction of 58.3% is smaller than the analytical (numerical, FEA) results due to the commutation noise, the back-EMF distortion, the cogging effect, the machine parameter uncertainties, the inverter non-linearity and the dead time effect. However, even in the worst scenario with all the effects, the experimental results with the torque ripple reduction of 58.3% has validated the significance of applying the proposed carrier phase shift PWM method.

4.5.2 Selective torque harmonic elimination method validation by experimental results

In order to validate the proposed CPS-PWM technique to eliminate selective torque harmonics for dual three-phase drives, experimental results were carried out using the test rig shown in Figure 4-26. The control algorithm, operating condition and the parameters are the same as the simulations, presented in Section 4.4.2. The experimental test rig consists of two modular three-phase inverters, a multiphase PMSM with external connection box, and a PLECS RT box operating as a controller to output the desired PWM signals to the modular converters.

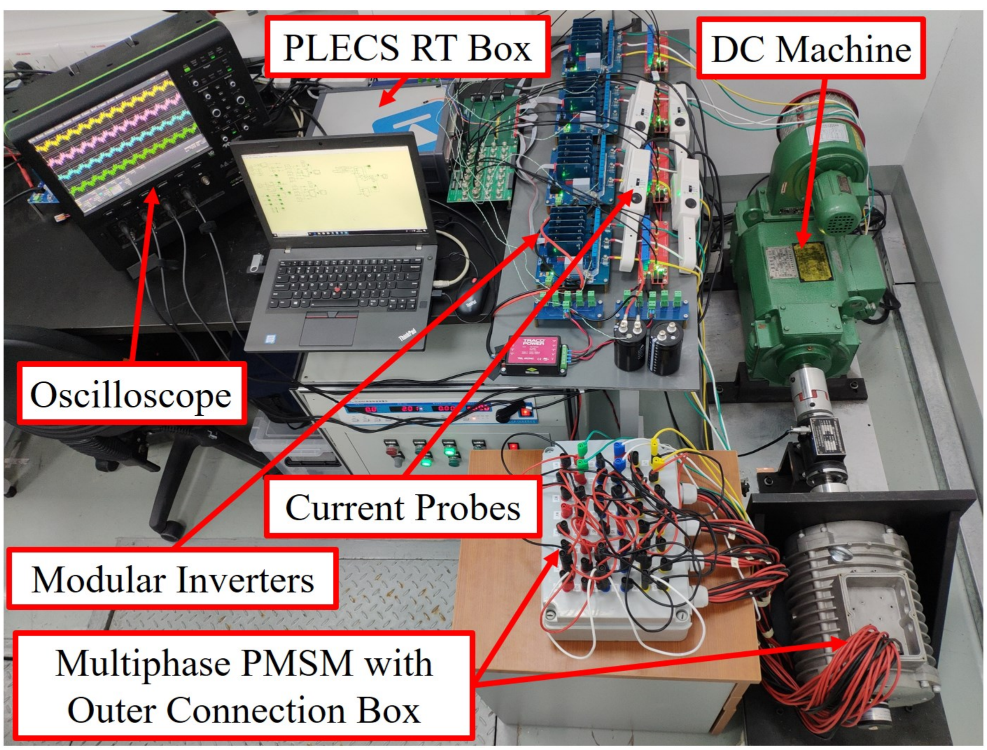

Figure 4-26: Dual three-phase drive systems (α=0 and α=$\frac{\pi}{6}$) experimental test rig.

The equivalent electromagnetic torque is calculated from the experimental phase currents referring to (4-23). Figure 4-27 shows the equivalent electromagnetic torque waveforms and their corresponding FFT spectra with winding configuration $\alpha = 0$ and modulation index M=0.8. Comparing Figure 4-27c and Figure 4-27d, the torque harmonic groups around 1 kHz, 3 kHz, 5 kHz are effectively cancelled out using the CPS-PWM. Comparing Figure 4-27a and Figure 4-27b, and peak to peak torque ripple is reduced by 36% employing CPS-PWM.

Figure 4-28 shows the equivalent electromagnetic torque waveforms and their corresponding FFT spectra with winding configuration $\alpha = \frac{\pi}{6}$ and modulation index M=0.3. Comparing Figure 4-28d and Figure 4-28e, the harmonic components at 0.925 kHz, 2 kHz, 3.075 kHz, and 4.925 kHz are effectively eliminated by the CPS-PWM ($\theta_{c2} - \theta_{c1} = \frac{\pi}{2}$). Comparing Figure 4-28d and Figure 4-28f, the harmonic components at 1.075 kHz, 2 kHz, 2.925 kHz, and 5.075 kHz are effectively eliminated applying the CPS-PWM ($\theta_{c2} - \theta_{c1} = -\frac{\pi}{2}$). Finally, from Figure 4-28a, Figure 4-28b and Figure 4-28c, it can be deduced that the peak to peak torque ripple is reduced by 35% and 48% employing the CPS-PWM of $\theta_{c2} - \theta_{c1} = \frac{\pi}{2}$ and $\theta_{c2} - \theta_{c1} = -\frac{\pi}{2}$ respectively.

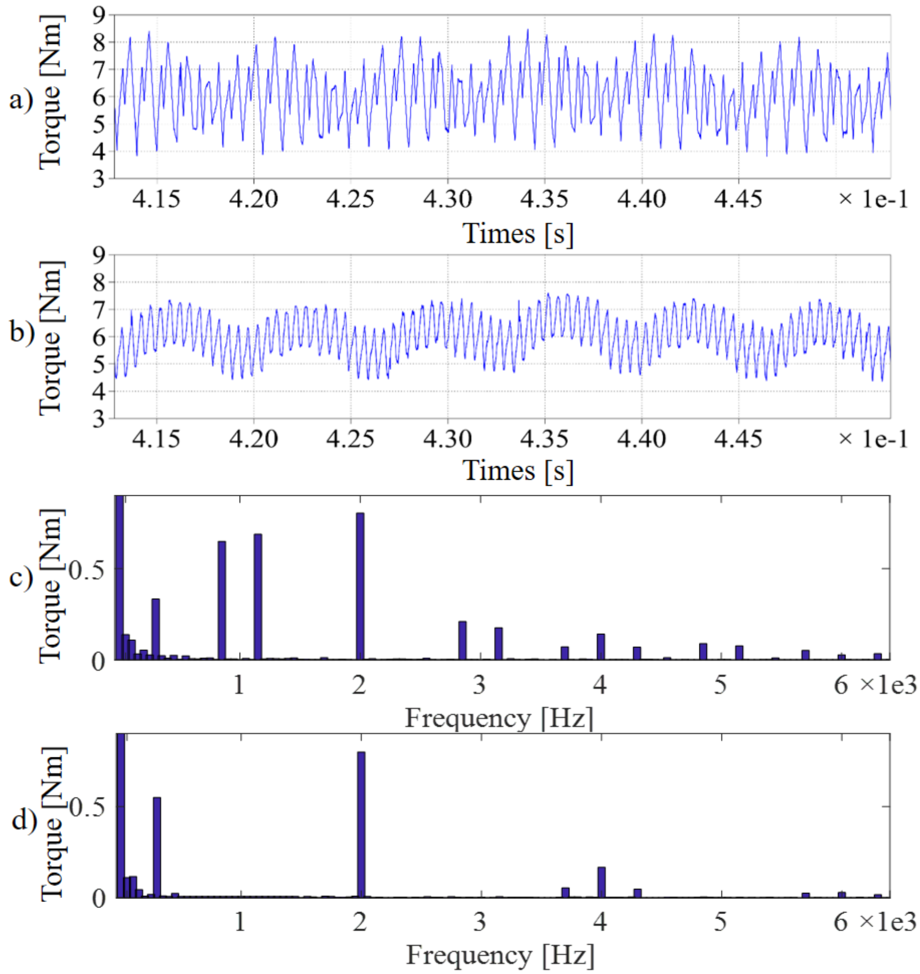

Figure 4-27: a) & b) Experimental results of equivalent electromagnetic torque waveforms of winding configuration $\alpha = 0$ a) without CPS-PWM, $\theta_{c2} - \theta_{c1} = 0$ b) with CPS-PWM, $\theta_{c2} - \theta_{c1} = \pi$ c) & d) Experimental results of equivalent electromagnetic torque FFT spectrums of winding configuration $\alpha = 0$ c) without CPS-PWM, $\theta_{c2} - \theta_{c1} = 0$ d) with CPS-PWM, $\theta_{c2} - \theta_{c1} = \pi$.

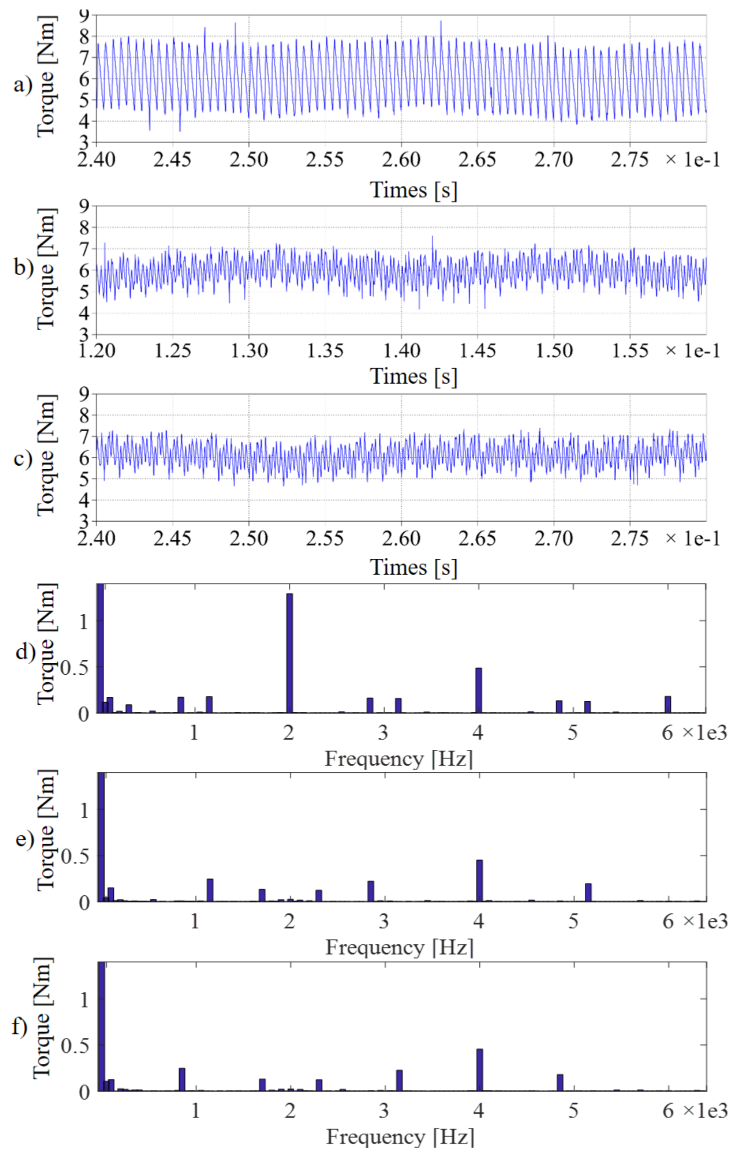

Figure 4-28: a) & b) & c) Experimental results of equivalent electromagnetic torque waveforms of winding configuration $\alpha = \frac{\pi}{6}$ a) without CPS-PWM, $\theta_{c2} - \theta_{c1} = 0$ b) with CPS-PWM, $\theta_{c2} - \theta_{c1} = \frac{\pi}{2}$ c) with CPS-PWM, $\theta_{c2} - \theta_{c1} = -\frac{\pi}{2}$ d) & e) & f) Experimental results of equivalent electromagnetic torque FFT spectrums of winding configuration $\alpha = \frac{\pi}{6}$ d) without CPS-PWM, $\theta_{c2} - \theta_{c1} = 0$ d) with CPS-PWM, $\theta_{c2} - \theta_{c1} = \frac{\pi}{2}$ f) with CPS-PWM, $\theta_{c2} - \theta_{c1} = -\frac{\pi}{2}$

4.6 Conclusion

Section 4.1 proposes a mathematical modelling of multi three-phase PWM converters. Section 4.2 presents mathematical torque equations of multi three-phase drives based on Section 4.1. Section 4.3 proposes the use of carrier phase shift approach, CPS-PWM, to mitigate the torque harmonic components in dual three-phase drives introduced by the PWM modulation. The proper carrier phase angles can be obtained by Table 4-1 for different dual three-phase drive systems. The most significant cases of dual three-phase systems, with $\alpha = 0$ and $= \frac{\pi}{6}$, are analyzed in depth.

Numerical, FEA simulations and experimental tests validate the analytical model (Section 4.2) shown in Section 4.4.1 and Section 4.5.1. The carrier phase shift angles obtained by the developed theory are applied on a case study of a sectored triple three-phase machine. The peak-to-peak values of the torque waveforms obtained by applying CPS-PWM are reduced by 79.5%, 78.5%, 63.8% and 58.3% compared with those obtained by not applying CPS-PWM in analytical, numerical, FEA and experimental results respectively. The PWM related harmonic components of the torque FFT spectrum obtained by applying CPS-PWM are effectively cancelled out.

The simulation results and experimental results to eliminate selective torque harmonic components are shown in Section 4.4.2 and 4.5.2 respectively. For $\alpha = 0$, applying the proposed carrier phase angle ($\theta_{c2} - \theta_{c1} = \pi$), the main torque harmonic components at the groups of 1 kHz, 3 kHz, and 5 kHz are effectively eliminated in both simulation and experimental results, and the peak to peak torque ripple is reduced by 49% and 36% in simulation and experimental results respectively. For $\alpha = \frac{\pi}{6}$, applying the proposed carrier phase shift angle ($\theta_{c2} - \theta_{c1} = \frac{\pi}{2}$), the main torque harmonic components at the 0.925 kHz, 2 kHz, 3.075 kHz, and 4.925 kHz are effectively eliminated in both simulation and experimental results, and the peak to peak torque ripple is reduced by 56% and 35% in simulation and experimental results respectively. For $\alpha = \frac{\pi}{6}$, using the proposed carrier phase shift angle ($\theta_{c2} - \theta_{c1} = -\frac{\pi}{2}$), the torque harmonic components at the 1.075 kHz, 2 kHz, 2.925 kHz, and 5.075 kHz are effectively eliminated in both simulation and experimental results, and the peak to peak torque ripple is reduced by 56% and 48% in simulation and experimental results respectively.

Therefore, applying CPS-PWM method to multi three-phase drives can effectively improve the torque performance of the machine, guaranteeing major benefits in terms of current and torque ripple without additional computational burden.

Chapter 5 Analysis of current ripple introduced by PWM related torque ripple reduction method

5.1 Analysis of current ripple in sectored triple three-phase drive introduced by PWM related torque ripple reduction method

As a case study, an 18 slots and 6 poles triple three-phase PMSM is shown in Figure 4-6. The machine has three sectors, sector 1, sector 2 and sector 3 respectively. Each sector has three phases (phase A, phase B, phase C) with an independent floating neutral point. The cross section of the considered machine is shown in Figure 4-6. The self-inductance of each stator phase $\mathrm{A_1}$, $\mathrm{B_1}$, $\mathrm{C_1}$, $\mathrm{A_2}$, $\mathrm{B_2}$, $\mathrm{C_2}$, $\mathrm{A_3}$, $\mathrm{B_3}$, $\mathrm{C_3}$ are represented by $L_{\mathrm{A_1}}$, $L_{\mathrm{B_1}}$, $L_{\mathrm{C_1}}$, $L_{\mathrm{A_2}}$, $L_{\mathrm{B_2}}$, $L_{\mathrm{C_2}}$, $L_{\mathrm{A_3}}$, $L_{\mathrm{B_3}}$, $L_{\mathrm{C_3}}$, respectively. The mutual inductance between the phases $\mathrm{A_1}$, $\mathrm{B_1}$, $\mathrm{C_1}$, $\mathrm{A_2}$, $\mathrm{B_2}$, $\mathrm{C_2}$, $\mathrm{A_3}$, $\mathrm{B_3}$, $\mathrm{C_3}$ are represented by $M_{\mathrm{A_1B_1}}$, $M_{\mathrm{A_1C_1}}$, …, $M_{\mathrm{C_3A_3}}$, $M_{\mathrm{C_3B_3}}$ respectively. Due to the symmetrical design of the winding configuration in Figure 4-6, the matrix inductance table $\boldsymbol{L}$ of the machine can be represented by:

$$\boldsymbol{L} = \begin{bmatrix} L & -M_1 & -M_1 & -M_3 & M_3 & M_3 & -M_3 & M_3 & M_3 \\ -M_1 & L & M_2 & M_3 & -M_3 & -M_3 & M_3 & -M_3 & -M_3 \\ -M_1 & M_2 & L & M_3 & -M_3 & -M_3 & M_3 & -M_3 & -M_3 \\ -M_3 & M_3 & M_3 & L & -M_1 & -M_1 & -M_3 & M_3 & M_3 \\ M_3 & -M_3 & -M_3 & -M_1 & L & M_2 & M_3 & -M_3 & -M_3 \\ M_3 & -M_3 & -M_3 & -M_1 & M_2 & L & M_3 & -M_3 & -M_3 \\ -M_3 & M_3 & M_3 & -M_3 & M_3 & M_3 & L & -M_1 & -M_1 \\ M_3 & -M_3 & -M_3 & M_3 & -M_3 & -M_3 & -M_1 & L & M_2 \\ M_3 & -M_3 & -M_3 & M_3 & -M_3 & -M_3 & -M_1 & M_2 & L \end{bmatrix}$$

where: $L = L_{k_p}$, $k \in \{\mathrm{A, B, C}\}$, , $p \in \{1, 2, 3\}$; $M_{\mathrm{A}_p k_p^1} = M_{k_p^1 \mathrm{A}_p} = M_1$, $k^1 \in \{\mathrm{B, C}\}$; $M_{\mathrm{B}_p \mathrm{C}_p} = M_{\mathrm{C}_p \mathrm{B}_p} = M_2$; $M_{k_p k'_{p'}} = M_3$, $k, k' \in \{\mathrm{A, B, C}\}$, $p, p' \in \{1, 2, 3\}$, $p \neq p'$.

The PWM related phase voltage harmonics and phase current harmonics of the p^{th} three-phase system can be represented by $u_{k_p,\mathrm{h}}$ and $i_{k_p,\mathrm{h}}$ ($p \in \{1, 2, 3\}$) respectively. Since the three phases in each sector are star-connected, the sum of three-phase currents is zero in any sector, leading to the following constraint:

$$i_{\mathrm{A}_p,\mathrm{h}} + i_{\mathrm{B}_p,\mathrm{h}} + i_{\mathrm{C}_p,\mathrm{h}} = 0, \tag{5-1}$$

According to the electric principle, the corresponding p^{th}phase voltage harmonic $u_{\mathrm{A}_p,\mathrm{h}}$, $u_{\mathrm{B}_p,\mathrm{h}}$, $u_{\mathrm{C}_p,\mathrm{h}}$ can be represented by (5-2), (5-3) and (5-4) respectively:

$$u_{\mathrm{A}_p,\mathrm{h}} = Ri_{\mathrm{A}_p,\mathrm{h}} + (L + M_1)\frac{\mathrm{d}}{\mathrm{d}t} i_{\mathrm{A}_p,\mathrm{h}} - (2M_3)\frac{\mathrm{d}}{\mathrm{d}t}(i_{\mathrm{A}_{p'},\mathrm{h}} + i_{\mathrm{A}_{p''},\mathrm{h}}) , \tag{5-2}$$

$$\begin{aligned} u_{\mathrm{B}_p,\mathrm{h}} &= Ri_{\mathrm{B}_p,\mathrm{h}} + (L + M_1)\frac{\mathrm{d}}{\mathrm{d}t} i_{\mathrm{B}_p,\mathrm{h}} + (M_1 + M_2)\frac{\mathrm{d}}{\mathrm{d}t} i_{\mathrm{C}_p,\mathrm{h}} \\ &-(2M_3)\frac{\mathrm{d}}{\mathrm{d}t}(i_{\mathrm{B}_{p'},\mathrm{h}} + i_{\mathrm{B}_{p''},\mathrm{h}}) - (2M_3)\frac{\mathrm{d}}{\mathrm{d}t}(i_{\mathrm{C}_{p'},\mathrm{h}} + i_{\mathrm{C}_{p''},\mathrm{h}}), \end{aligned} \tag{5-3}$$

$$\begin{aligned} u_{\mathrm{C}_p,\mathrm{h}} &= Ri_{\mathrm{C}_p,\mathrm{h}} + (L + M_1)\frac{\mathrm{d}}{\mathrm{d}t} i_{\mathrm{C}_p,\mathrm{h}} + (M_1 + M_2)\frac{\mathrm{d}}{\mathrm{d}t} i_{\mathrm{B}_p,\mathrm{h}} \\ &-(2M_3)\frac{\mathrm{d}}{\mathrm{d}t}(i_{\mathrm{C}_{p'},\mathrm{h}} + i_{\mathrm{C}_{p''},\mathrm{h}}) - (2M_3)\frac{\mathrm{d}}{\mathrm{d}t}(i_{\mathrm{B}_{p'},\mathrm{h}} + i_{\mathrm{B}_{p''},\mathrm{h}}). \end{aligned} \tag{5-4}$$

where $p, p', p'' \in \{1, 2, 3\}, p \neq p' \neq p''$. The fundamental components of phase currents and phase voltages are not defined by (5-2), (5-3) and (5-4) as the back-EMFs are not included. As it is mentioned above, for this case study, the electrical phase shift among the various three-phase systems is zero.($\alpha_p = 0, p \in \{1, 2, 3\}$). Therefore, without CPS-PWM method ($\theta_{\mathrm{c},1} = \theta_{\mathrm{c},2} = \theta_{\mathrm{c},3} = 0$), the phase current harmonics of each sector are the same

($i_{k_p,\mathrm{h}} = i_{k_{p'},\mathrm{h}} = i_{k_{p''},\mathrm{h}}$, $k \in \{\mathrm{A, B, C}\}$). By properly manipulating (5-2), (5-3) and (5-4), the corresponding p^{th} phase voltage harmonic $u_{\mathrm{A}_p,\mathrm{h}}$, $u_{\mathrm{B}_p,\mathrm{h}}$, $u_{\mathrm{C}_p,\mathrm{h}}$ without applying CPS-PWM can be respectively rewritten as:

$$u_{\mathrm{A}_p,\mathrm{h}} = Ri_{\mathrm{A}_p,\mathrm{h}} + (L+M_1 - 4M_3)\frac{\mathrm{d}}{\mathrm{d}t} i_{\mathrm{A}_p,\mathrm{h}}, \tag{5-5}$$

$$u_{\mathrm{B}_p,\mathrm{h}} = Ri_{\mathrm{B}_p,\mathrm{h}} + (L+M_1 - 4M_3)\frac{\mathrm{d}}{\mathrm{d}t} i_{\mathrm{B}_p,\mathrm{h}} + (M_1 + M_2 - 4M_3)\frac{\mathrm{d}}{\mathrm{d}t} i_{\mathrm{C}_p,\mathrm{h}}, \tag{5-6}$$

$$u_{\mathrm{C}_p,\mathrm{h}} = Ri_{\mathrm{C}_p,\mathrm{h}} + (L+M_1 - 4M_3)\frac{\mathrm{d}}{\mathrm{d}t} i_{\mathrm{C}_p,\mathrm{h}} + (M_1 + M_2 - 4M_3)\frac{\mathrm{d}}{\mathrm{d}t} i_{\mathrm{B}_p,\mathrm{h}}. \tag{5-7}$$

Whereas, by applying the proposed CPS-PWM method ($\theta_{\mathrm{c},1} = 0$, $\theta_{\mathrm{c},2} = \frac{2\pi}{3}$, $\theta_{\mathrm{c},3} = \frac{4\pi}{3}$), there are two conditions of phase current harmonics according to (4-17). First, for the harmonic components of the total current space vector which cannot be cancelled out by the CPS-PWM method (around the frequency of $3zf_\mathrm{c}$, $\mathrm{z} \in \{1, 2, \ldots, \infty\}$), the relevant phase current harmonics of each sector are the same ($i_{k_1,\mathrm{h}} = i_{k_2,\mathrm{h}} = i_{k_3,\mathrm{h}}$, $k \in \{\mathrm{A, B, C}\}$). Therefore, the corresponding p^{th} phase voltage harmonics $u_{\mathrm{A}_p,\mathrm{h}}$, $u_{\mathrm{B}_p,\mathrm{h}}$, $u_{\mathrm{C}_p,\mathrm{h}}$ with applying CPS-PWM can be represented by (5-5), (5-6) and (5-7) respectively. Secondly, for the harmonic components of the total current space vector which can be cancelled out by the CPS-PWM method (around the frequency of zf_c and $2zf_\mathrm{c}$, $\mathrm{z} \in \{1, 2, \ldots, \infty\}$), the sum of phase current harmonics from different sectors is equal to 0, which can be represented by (5-8):

$$i_{k,\mathrm{h}} = \sum_{p=1}^{N} i_{k_p,\mathrm{h}} = i_{k_1,\mathrm{h}} + i_{k_2,\mathrm{h}} + i_{k_3,\mathrm{h}} = 0, \tag{5-8}$$

where $k \in \{\mathrm{A, B, C}\}$. It results that the corresponding p^{th} phase voltage harmonic $u_{\mathrm{A}_p,\mathrm{h}}$, $u_{\mathrm{B}_p,\mathrm{h}}$, $u_{\mathrm{C}_p,\mathrm{h}}$ with applying CPS-PWM can be represented by (5-9), (5-10) and (5-11) respectively:

$$u_{\mathrm{A}_p,\mathrm{h}} = Ri_{\mathrm{A}_p,\mathrm{h}} + (L + M_1 + 2M_3)\frac{\mathrm{d}}{\mathrm{d}t} i_{\mathrm{A}_p,\mathrm{h}}, \tag{5-9}$$

$$u_{\mathrm{B}_p,\mathrm{h}} = Ri_{\mathrm{B}_p,\mathrm{h}} + (L + M_1 + 2M_3)\frac{\mathrm{d}}{\mathrm{d}t} i_{\mathrm{B}_p,\mathrm{h}} + (M_1 + M_2 + 2M_3)\frac{\mathrm{d}}{\mathrm{d}t} i_{\mathrm{C}_p,\mathrm{h}}, \tag{5-10}$$

$$u_{\mathrm{C}_p,\mathrm{h}} = Ri_{\mathrm{C}_p,\mathrm{h}} + (L + M_1 + 2M_3)\frac{\mathrm{d}}{\mathrm{d}t} i_{\mathrm{C}_p,\mathrm{h}} + (M_1 + M_2 + 2M_3)\frac{\mathrm{d}}{\mathrm{d}t} i_{\mathrm{B}_p,\mathrm{h}}. \tag{5-11}$$

For phase A in each sector, the effective inductance $(L + M_1 - 4M_3)$ in (5-5) is smaller than the effective inductance $(L + M_1 + 2M_3)$ in (5-9). For phase B and C in each sector, the effective self-inductance $(L + M_1 - 4M_3)$ in (5-6) and (5-7) is smaller than the effective self-inductance $(L + M_1 + 2M_3)$ in (5-10) and (5-11); the effective mutual inductance between phase B and C $(M_1 + M_2 - 4M_3)$ in (5-6) and (5-7) is smaller than the effective mutual inductance $(M_1 + M_2 + 2M_3)$ in (5-10) and (5-11). Overall, for the considered sectored machine, the effective inductance without applying CPS-PWM method is smaller than the effective inductance with applying CPS-PWM. The amplitudes of phase voltage harmonics with and without CPS-PWM are the same [84]. Therefore, the amplitudes of phase current harmonics with applying CPS-PWM method are smaller than the ones obtained without the CPS-PWM method. The numerical results obtained in PLECS of the normalized phase current FFT spectrum with and without CPS-PWM under different modulation index ($M = 0.3$, $M = 0.6$ and $M = 0.9$) is shown in Figure 5-1.

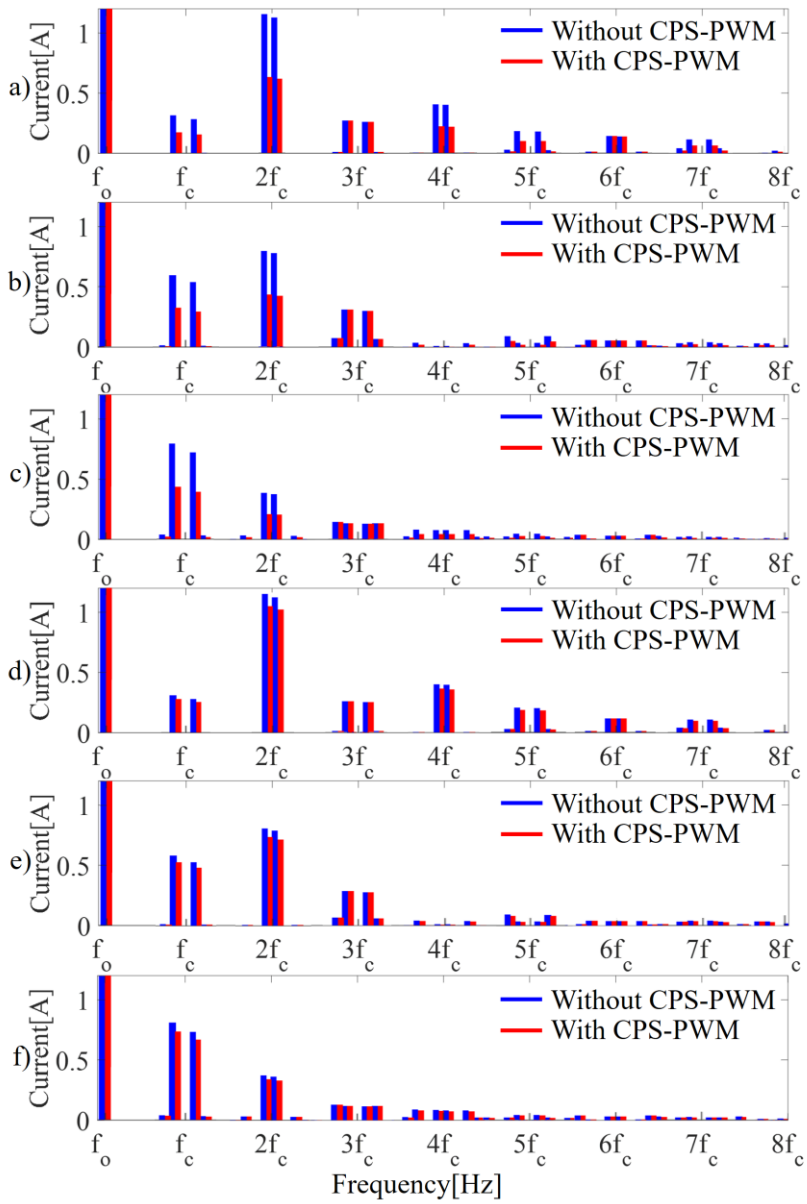

Figure 5-1: Numerical result of phase current FFT spectrum without and with CPS-PWM a) current phase A with $M = 0.3$ b) current phase A with $M = 0.6$ c) current phase A with $M = 0.9$ d) current phase B&C with $M = 0.3$ e) current phase B&C with $M = 0.6$ f) current phase B&C with $M = 0.9$ [102].

5.2 Analysis of current ripple in distributed dual three-phase drives introduced by PWM related torque ripple reduction method

According to the symmetrical design principle of distributed winding machines, the inductance matrix of a dual three-phase PMSM machine can be represented by $\boldsymbol{L}$:

$$\boldsymbol{L} = \begin{bmatrix} L & M_0 & M_0 & M_1 & M_2 & M_3 \\ M_0 & L & M_0 & M_3 & M_1 & M_2 \\ M_0 & M_0 & L & M_2 & M_3 & M_1 \\ M_1 & M_3 & M_2 & L & M_0 & M_0 \\ M_2 & M_1 & M_3 & M_0 & L & M_0 \\ M_3 & M_2 & M_1 & M_0 & M_0 & L \end{bmatrix}$$

where L is the self-inductance of each phase. $|M_0|$ is the mutual inductance between phase A_p, B_p and C_p for $p \in \{1, 2\}$. $|M_1|$ is the mutual inductance between phase k_p and $k_{p'}$, for $k \in \{\mathrm{A}, \mathrm{B}, \mathrm{C}\}$, $p, p' \in \{1, 2\}$ and $p \neq p'$. $|M_2|$ is the mutual inductance between phase A_p and $B_{p'}$, or phase B_p and $C_{p'}$. $|M_3|$ is the mutual inductance between phase A_p and $C_{p'}$. M, M_1, M_2 and M_3 can be positive or negative values depending on the position and the current direction between the corresponding two phases. In addition, due to the symmetrical design of the dual three-phase machine, the relationship between M_1, M_2, M_3 and α (the phase shift angle in electrical radians between the two three-phase subsystems) can be represented by (5-12):

$$M_1 + M_2 e^{-j\frac{2}{3}\pi} + M_3 e^{j\frac{2}{3}\pi} = M' e^{j\alpha}, \tag{5-12}$$

where M' is a real value.

For the dual three-phase drive system in Figure 4-9, the voltage differences between terminals $\mathrm{a_1}$, $\mathrm{b_1}$, $\mathrm{c_1}$, $\mathrm{a_2}$, $\mathrm{b_2}$, $\mathrm{c_2}$ and terminals $\mathrm{o_1}$, $\mathrm{o_2}$ are considered as phase voltages, which are represented by $u_{\mathrm{a_1}}$, $u_{\mathrm{b_1}}$, $u_{\mathrm{c_1}}$, $u_{\mathrm{a_2}}$, $u_{\mathrm{b_2}}$, $u_{\mathrm{c_2}}$ respectively. Similarly, the phase currents are represented by $i_{\mathrm{a_1}}$, $i_{\mathrm{b_1}}$, $i_{\mathrm{c_1}}$, $i_{\mathrm{a_2}}$, $i_{\mathrm{b_2}}$, $i_{\mathrm{c_2}}$, and the back-EMFs generated on each phase by the rotor flux (permanent magnets) can be defined as $e_{\mathrm{a_1}}$, $e_{\mathrm{b_1}}$, $e_{\mathrm{c_1}}$, $e_{\mathrm{a_2}}$, $e_{\mathrm{b_2}}$, $e_{\mathrm{c_2}}$ respectively. According to the electric principle, the phase voltage matrix is represented by:

$$\begin{bmatrix} v_{a1} \\ v_{b1} \\ v_{c1} \\ v_{a2} \\ v_{b2} \\ v_{c2} \end{bmatrix} = \begin{bmatrix} L & M & M & M_1 & M_2 & M_3 \\ M & L & M & M_3 & M_1 & M_2 \\ M & M & L & M_2 & M_3 & M_1 \\ M_1 & M_3 & M_2 & L & M & M \\ M_2 & M_1 & M_3 & M & L & M \\ M_3 & M_1 & M_2 & M & M & L \end{bmatrix} \frac{d}{dt} \begin{bmatrix} i_{a1} \\ i_{b1} \\ i_{c1} \\ i_{a2} \\ i_{b2} \\ i_{c2} \end{bmatrix} + R \begin{bmatrix} i_{a1} \\ i_{b1} \\ i_{c1} \\ i_{a2} \\ i_{b2} \\ i_{c2} \end{bmatrix} + \begin{bmatrix} e_{a1} \\ e_{b1} \\ e_{c1} \\ e_{a2} \\ e_{b2} \\ e_{c2} \end{bmatrix} \tag{5-13}$$

According to (5-13), the phase voltages of the first three-phase subsystem V_{a1}, V_{b1} and V_{c1} can be represented by (5-14), (5-15) and (5-16) respectively:

$$V_{a1} = Li_{a1} + Mi_{b1} + Mi_{c1} + M_1 i_{a2} + M_2 i_{b2} + M_3 i_{c2} \tag{5-14}$$

$$V_{b1} = Mi_{a1} + Li_{b1} + Mi_{c1} + M_3 i_{a2} + M_1 i_{b2} + M_2 i_{c2} \tag{5-15}$$

$$V_{c1} = Mi_{a1} + Mi_{b1} + Li_{c1} + M_2 i_{a2} + M_3 i_{b2} + M_1 i_{c2} \tag{5-16}$$

The voltage space vector and the current space vector of the first three-phase subsystem $\vec{V}_1$ and $\vec{\imath}_1$ can be represented as:

$$\vec{V}_1 = V_{a1} + V_{b1} e^{j\frac{2}{3}\pi} + V_{c1} e^{-j\frac{2}{3}\pi}, \tag{5-17}$$

$$\vec{\imath}_1 = i_{a1} + i_{b1} e^{j\frac{2}{3}\pi} + i_{c1} e^{-j\frac{2}{3}\pi} \tag{5-18}$$

Since each subsystem is star connected, thus:

$$i_{a1} + i_{b1} + i_{c1} = 0 \tag{5-19}$$

Substituting (5-14) (5-15) (5-16) and (5-19)into (5-17), $\vec{V}_1$ can be represented as:

$$\vec{V}_1 = (L - M)\frac{\mathrm{d}}{\mathrm{d}t}\vec{i}_1(t) + \left(M_1 + M_2 e^{-j\frac{2}{3}\pi} + M_3 e^{j\frac{2}{3}\pi}\right)\frac{\mathrm{d}}{\mathrm{d}t}\vec{i}_2(t) + R\vec{i}_1(t) + \vec{e}_1, \tag{5-20}$$

Similarly, $\vec{V}_2$ can be represented as:

$$\vec{V}_2 = (L - M)\frac{\mathrm{d}}{\mathrm{d}t}\vec{i}_2(t) + \left(M_1 + M_2 e^{-j\frac{2}{3}\pi} + M_3 e^{j\frac{2}{3}\pi}\right)\frac{\mathrm{d}}{\mathrm{d}t}\vec{i}_1(t) + R\vec{i}_2(t) + \vec{e}_2, \tag{5-21}$$

While considering the relationship between the PWM harmonic voltage and the related PWM harmonic current (it is implicit that they are high frequency components), the effect of the voltage drop on the phase resistance and the back-EMF distortion at the same frequency are neglected. Substituting the (5-12) into (5-20) and (5-21), the relationship between the PWM harmonic phase voltage space vector $\vec{u}_{p,\mathrm{PWM}}$ and the PWM harmonic phase current space vector $\vec{i}_{p,\mathrm{PWM}}$ of each three-phase subsystem can be represented by (5-22):

$$\vec{u}_{p,\mathrm{PWM}} = (L - M_0)\frac{d}{dt}\vec{i}_{p,\mathrm{PWM}} + M' e^{j\alpha}\frac{d}{dt}\vec{i}_{p',\mathrm{PWM}}, \tag{5-22}$$

where $p, p' \in \{1, 2\}$ and $p \neq p'$.

As in Section III, the analysis proceeds taking into consideration the two winding layouts with $\alpha = 0$ and $\alpha = \frac{\pi}{6}$, as examples. According to Table 4-2, there are four significant values of the voltage space vector phase angle differences between the two three-phase subsystems, which are 0, π, $\frac{\pi}{2}$ and $-\frac{\pi}{2}$. While the phase angle difference is 0 ($\vec{u}_{1,\mathrm{PWM}} = \vec{u}'_{2,\mathrm{PWM}}$), the relationship between $\vec{u}_{p,\mathrm{PWM}}$ and $\vec{i}_{p,\mathrm{PWM}}$ can be represented by (5-23):

$$\vec{u}_{p,\mathrm{PWM}} = (L - M_0 + M')\vec{i}_{p,\mathrm{PWM}}. \tag{5-23}$$

While the angle difference is π ($\vec{u}_{1,\text{PWM}} = -\vec{u}'_{2,\text{PWM}}$), the relationship between the $\vec{u}_{p,\text{PWM}}$ and $\vec{\imath}_{p,\text{PWM}}$ can be represented by (5-24):

$$\vec{u}_{p,\text{PWM}} = (L - M_0 - M')\vec{\imath}_{p,\text{PWM}}. \tag{5-24}$$

While the angle difference is $\pm\frac{\pi}{2}$ ($\vec{u}_{1,\text{PWM}} = \vec{u}'_{2,\text{PWM}} e^{\pm j\frac{\pi}{2}t}$), the relationship between the $\vec{u}_{p,\text{PWM}}$ and $\vec{\imath}_{p,\text{PWM}}$ can be represented by (5-25):

$$\vec{u}_{p,\text{PWM}} = (L - M_0)\vec{\imath}_{p,\text{PWM}}. \tag{5-25}$$

If M' is a positive value, the effective impedances Z in (5-23), (5-24) and (5-25) are Z(5-23)> Z(5-25) > Z(5-24). According to (4-24) and (4-25), the amplitudes of the PWM voltage space vector are the same despite the values of α, θ_{c1}, and θ_{c2}, so the amplitudes of the PWM current space vector I in (5-23), (5-24) and (5-25) are I(5-24)> I(5-25) > I(5-23). If M' is a negative value, the effective impedances in (5-23), (5-24) and (5-25) are Z(5-23)< Z(5-25) < Z(5-24), and the amplitudes of the PWM current space vector in (5-23), (5-24) and (5-25) are I(5-24)< I(5-25) < I(5-23). Therefore, whether the amplitude of each phase current harmonic component with CPS-PWM changes or not (increases, decreases, maintains the same value) can be addressed by referring to the voltage space vector phase angle differences in Table 4-2.

It is important to observe that, as a result of this study, if a time harmonic of the total current vector is selectively eliminated, imposing a defined shift of the carriers, the current ripple at the selected frequency can either increase or decrease according to the change in the equivalent impedance of each three-phase subsystem. For example, it is possible that the CPS-PWM makes the two windings increase their current distortion at the selected frequency, even if the related torque ripple is eliminated, because the torque ripple is produced by the sum of the current contributions of the two three-phase windings which are out of phase (eliminating each other).

5.3 Simulation results

5.3.1 Simulation results of phase currents in the sectored triple three-phase drive

The simulation model and parameters used in this Section are the same with the one in Section 4.4.1. The simulation results of phase currents based on a sectored triple three-phase machine drive with the converter and machine paratermeters shown in Table 4-4 are carried out in this PLECS. The cross section of the triple three-phase PM machine is shown in Figure 4-6. The operating condition concerning the numerical results is no load condition. There is no external load on the machine and the machine operating power is to overcome the mechanical (friction) power loss and the electromagnetic power loss of the machine itself. The block diagram for the control of the nine-phase machine fed by its three independent PWM converters is shown in Figure 4-15. The CPS-PWM method is applied to the three three-phase systems with carrier phase shift angles $\theta_{c,1}$, $\theta_{c,2}$, and $\theta_{c,3}$ respectively. The simulation results of phase currents with and without CPS-PWM are shown in this section. The proposed carrier phase angles used in this case are $\theta_{c,1} = 0$, $\theta_{c,2} = \frac{2\pi}{3}$ and $\theta_{c,3} = \frac{4\pi}{3}$ for sector 1, sector 2 and sector 3 respectively.

Figure 5-2 shows the numerical current results of phase A_1, A_2 and A_3 with and without applying CPS-PWM. Figure 5-2b and Figure 5-2d are the zoom of the waveform in between the cursor ranges of Figure 5-2a and Figure 5-2c respectively. Comparing Figure 5-2b and Figure 5-2d, the phase current harmonics in different sectors are effectively shifted with applying the CPS-PWM method. Comparing Figure 5-2a and Figure 5-2c, the amplitudes of phase current harmonics obtained by applying CPS-PWM are reduced compared with those obtained by not applying the CPS-PWM. The corresponding FFT spectrum of Figure 5-2a and Figure 5-2c are shown in Figure 4-16c and Figure 4-16d respectively. For all of the harmonic components except the harmonics around 6 kHz and 12 kHz in Figure 4-16c and Figure 4-16d (numerical result), their amplitudes in Figure 4-16d are reduced by 45.18% compared with the ones in Figure 4-16c.

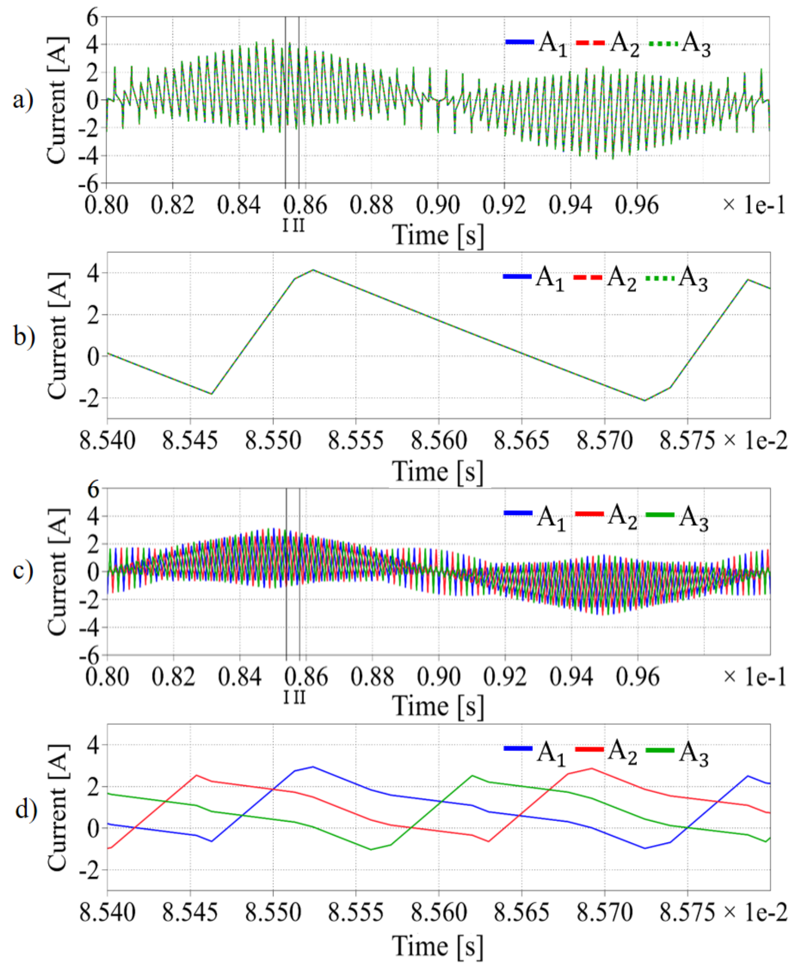

Figure 5-2: a) & b) Numerical results of current waveform of phase A1 A2 & A3 without CPS-PWM a) One period range of fundamental signal b) Two periods range of carrier signal c) & d) Numerical results of current waveform of phase A1 A2 & A3 with CPS-PWM c) One period range of fundamental signal d) Two periods range of carrier signal [102].

5.3.2 Simulation results of phase currents in the distributed dual three-phase drive

The simulation model and parameters used in this Section are the same with the one in Section 4.4.2. In order to validate the effect on phase currents while different carrier phase shift angles are applied to the dual three-phase drives to eliminate the selective torque harmonics, simulation models of the PM machine with two different stator winding configurations ($\alpha = 0$ and $\alpha = \frac{\pi}{6}$) are established in PLECS. The machine stator winding configuration is changed by the external connection box shown in Figure 4-26. The stator winding layout of the dual three-phase PMSM is shown in Appendix E. The connection circuits of $\alpha = 0$ and $\alpha = \frac{\pi}{6}$ are shown in Figure 4-18a and Figure 4-18b respectively. The machine parameters under the two different winding configurations ($\alpha = 0$ and $= \frac{\pi}{6}$) are shown in Table 4-5.

The simulation model in PLECS is a voltage open loop control used for validating the proposed control technique without interfering with the use of current PI regulators, which might affect the voltage and current waveforms. The corresponding control block diagram is shown Figure 4-19. The carrier phase shift angles θ_{c1} and θ_{c2} are applied to the first and the second three-phase systems respectively. The switching frequency of each converter is f_c=1 kHz. The machine speed of the two winding configurations ($\alpha = 0$ and $= \frac{\pi}{6}$) is fixed to 375 rpm (i.e., a fundamental frequency f_o= 25 Hz) by keeping the product of the DC link voltage and the modulation index (V_{dc} and M) as a constant. The simulated condition is a low load operation of the motor at 6Nm output torque.

For the winding configuration $\alpha = 0$, according to (5-12) and the inductance values of M_1, M_2 and M_3 in Table 4-5, M' is a negative value: M'= -0.131mH. According to Table 4-2, if $\alpha = 0$ the voltage phase angle difference between the two three-phase subsystems of the harmonic groups around 1 kHz, 3 kHz, 5 kHz changes from 0 to π with the CPS-PWM, while it remains zero for the other frequencies in the analyzed range. Therefore, conforming to (5-23) and (5-24), for harmonic groups around 1 kHz, 3 kHz and 5 kHz, the effective impedances are increased and the amplitudes of the related current harmonic components are decreased employing the CPS-PWM. Figure 5-3 shows the phase current waveforms and their corresponding FFT spectra with and without CPS-PWM of winding configuration $\alpha = 0$ under the modulation index M=0.8. Comparing Figure 5-3c and Figure 5-3d, the amplitudes of current harmonic groups around 1 kHz, 3 kHz and 5 kHz are reduced by 55% applying the CPS-PWM technique.

For the winding configuration of $\alpha = \frac{\pi}{6}$, according to (5-12) and the inductance values of M_1, M_2 and M_3 in Table 4-5, M' is a positive value: M'= 0.114 mH. Figure 5-4 shows that the phase current waveforms and their corresponding FFT spectra with and without CPS-PWM of winding configuration $\alpha = \frac{\pi}{6}$ under the modulation index M=0.3. Comparing Figure 5-4d, Figure 5-4f and Figure 5-4e, the amplitudes of current harmonic reduction/increase percentage with applying $\theta_{c2} - \theta_{c1} = \pm\frac{\pi}{2}$ can be analyzed. Comparing Figure 5-4d and Figure 5-4f, with apply CPS-PWM ($\theta_{c2} - \theta_{c1} = \frac{\pi}{2}$), the amplitudes of current harmonics at 0.95 kHz, 3.05 kHz and 4.95 kHz are increased by 39%; The amplitudes of current harmonics at 1.975 kHz, 2.025 kHz, 5.975 kHz and 6.025 kHz are increased by 430% ; The amplitudes of current harmonics at 1.05 kHz, 2.95 kHz, 5.05

kHz are decreased by 74%. Comparing Figure 5-4e and Figure 5-4f, applying CPS-PWM ($\theta_{c2} - \theta_{c1} = -\frac{\pi}{2}$) the amplitudes of current harmonics at 1.05 kHz, 1.975 kHz, 2.025 kHz are increased by 39%; the amplitudes of current harmonics at 1.975 kHz, 2.025 kHz, 5.975 kHz and 6.025 kHz are increased by 430%; the amplitudes of current harmonics at 0.95 kHz, 3.05 kHz and 4.95 kHz are decreased by 74%. The comparison of the results is summarized in Table 5-1. Referring to Table 4-2, the reduction or increase trend of the current harmonic amplitudes shown in Table 5-1 conforms to (5-23), (5-24) and (5-25) in Section 5.3.2.

Carrier Phase Shift Angle	Frequency [kHz]			
	0.95	1.05	1.975	2.025
$\frac{\pi}{2}$	↑39%	↓74%	↑430%	↑430%
$-\frac{\pi}{2}$	↓74%	↑39%	↑430%	↑430%
	2.95	3.05	3.975	4.025
$\frac{\pi}{2}$	↓74%	↑39%	0%	0%
$-\frac{\pi}{2}$	↑39%	↓74%	0%	0%
	4.95	5.05	5.975	6.025
$\frac{\pi}{2}$	↑39%	↓74%	↑430%	↑430%
$-\frac{\pi}{2}$	↓74%	↑39%	↑430%	↑430%

Table 5-1: Amplitudes of phase current harmonic reduction/increase with CPS-PWM of winding configuration $\alpha=\frac{\pi}{6}$ (simulation results)

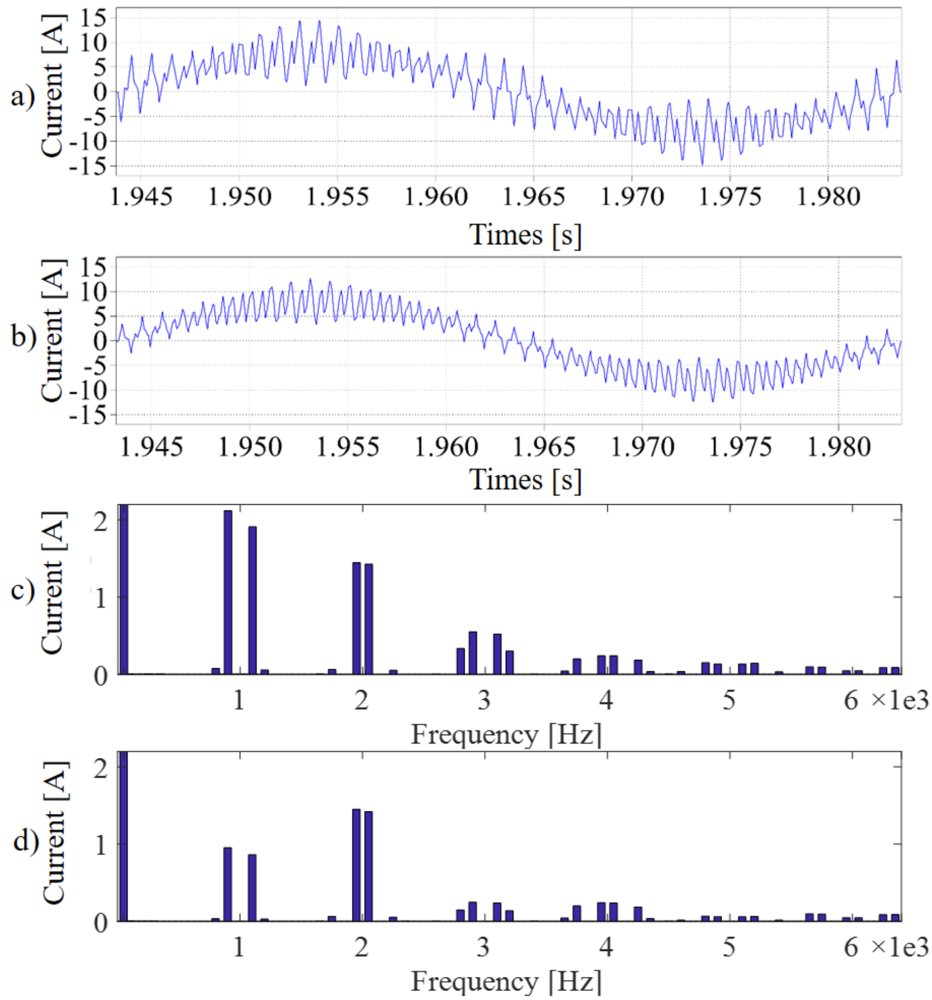

Figure 5-3: a) & b) Simulation results of phase current waveforms of winding configuration $\alpha = 0$ a) without CPS-PWM, $\theta_{c2} - \theta_{c1} = 0$ b) with CPS-PWM, $\theta_{c2} - \theta_{c1} = \pi$ c) & d) Simulation results of phase current FFT spectrums of winding configuration $\alpha = 0$ c) without CPS-PWM, $\theta_{c2} - \theta_{c1} = 0$ d) with CPS-PWM, $\theta_{c2} - \theta_{c1} = \pi$

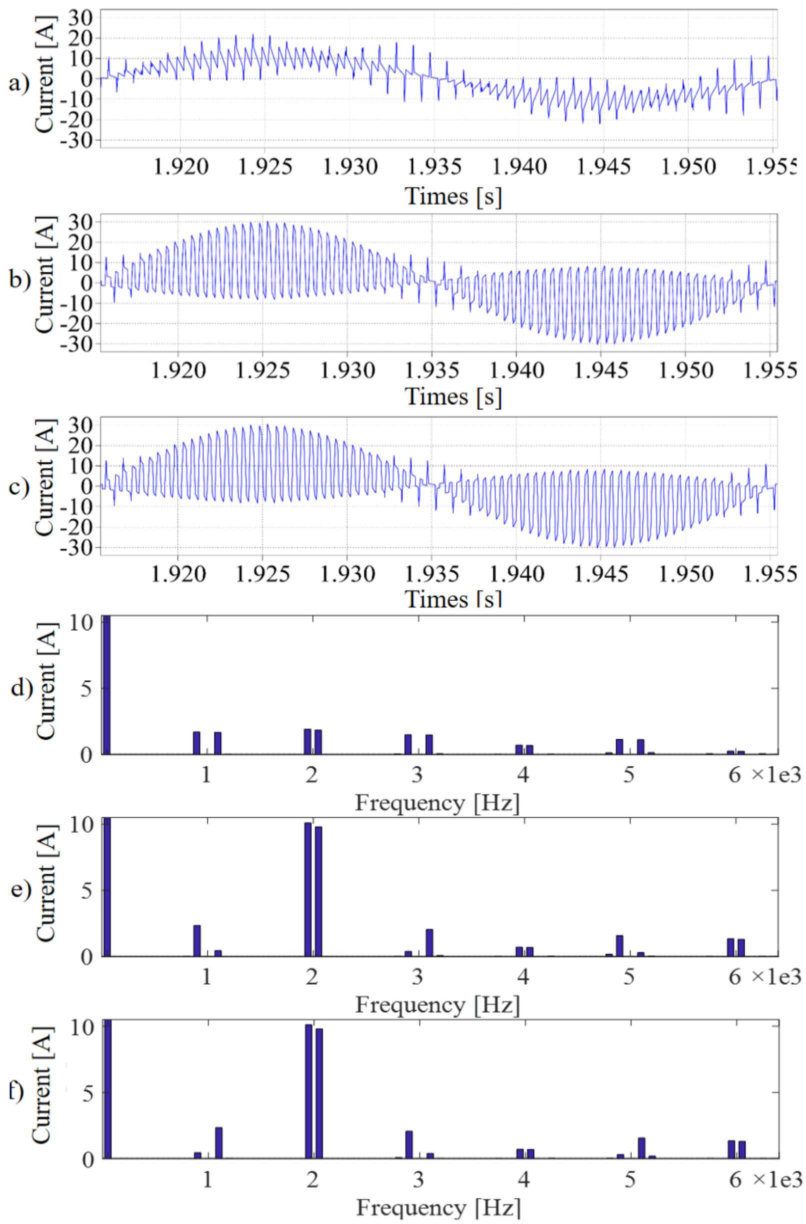

Figure 5-4: a) & b) & c) Simulation results of phase current waveforms of winding configuration $\alpha = \frac{\pi}{6}$ a) without CPS-PWM, $\theta_{c2} - \theta_{c1} = 0$ b) with CPS-PWM, $\theta_{c2} - \theta_{c1} = \frac{\pi}{2}$ c) with CPS-PWM, $\theta_{c2} - \theta_{c1} = -\frac{\pi}{2}$ d) & e) & f) Simulation results of phase current FFT spectrums of winding configuration $\alpha = \frac{\pi}{6}$ d) without CPS-PWM, $\theta_{c2} - \theta_{c1} = 0$ e) with CPS-PWM, $\theta_{c2} - \theta_{c1} = \frac{\pi}{2}$ f) with CPS-PWM, $\theta_{c2} - \theta_{c1} = -\frac{\pi}{2}$

5.4 Experimental results

5.4.1 Experimental results of phase currents in the sectored triple three-phase drive

The parameters used in this Section are the same with the one in Section 4.5.1. In order to validate the simulation results of the phase currents in the sectored triple three-phase drive, experimental tests have been carried out by means of the platform shown in Figure 4-23. The parameters and the control algorithm used in the experimental platform is the one explained in Section 5.3.1 (Section 4.4.1). The operating condition concerning the experimental results (same as the numerical result) is no load condition. There is no external load and the machine operating power is to overcome the mechanical (friction) power loss and the electromagnetic power loss of the machine itself. The experimental setup consists of triple three-phase inverters with standard IGBT modules, a sectored triple three-phase PMSM with its cross section shown in Figure 4-6, and a centralized controller (uCube [103]). Optical fiber is used to communicate between the power module gate drives and the uCube.

Figure 5-5 shows the experimental current results of phase A_1, A_2 and A_3 with and without applying CPS-PWM. Figure 5-5b and Figure 5-5d are the zoom of the waveform in between the cursor ranges of Figure 5-5a and Figure 5-5c respectively. Comparing Figure 5-5b and Figure 5-5d, the phase current harmonics in different sectors are effectively shifted with applying the CPS-PWM method. Comparing Figure 5-5a and Figure 5-5c, the amplitudes of the phase current harmonics obtained by applying CPS-PWM are reduced compared with those obtained by not applying CPS-PWM. The corresponding FFT spectrum of Figure 5-5a and Figure 5-5c are shown in Figure 5-5e, which shows that the amplitudes of harmonic components around 2 kHz, 4 kHz, 8 kHz, 10 kHz, 14 kHz and 16 kHz obtained by applying CPS-PWM are reduced by about 36.1% 38.4%, 36.1%, 34.7%, 34.1%, 29.5% respectively compared with those obtained by not applying CPS-PWM. The improvement achieved with CPS-PWM in the experimental results is reduced compared with the improvement in the numerical results, due to the back-EMF distortion, the machine parameter uncertainties, the inverter non-linearity and the dead time effect. Another effect is the switching noise that causes current spikes during the commutations, as visible in Figure 5-5b and Figure 5-5d, that accounts for 4.6% of torque ripple increase (evaluated by numerically removing the switching noise).

The improvement achieved with CPS-PWM is sensibly reduced in the experimental results compared with the simulation results. According to Figure 4-16c and Figure 4-16d (numerical results), for all of the harmonic components except the harmonics around 6 kHz and 12 kHz, their amplitudes in Figure 4-16d (with CPS-PWM) are reduced by 45.18% compared with the ones in Figure 4-16c (without CPS-PWM). According to Figure 5-5e (experimental result), the amplitudes of harmonic components around 2 kHz, 4 kHz, 8 kHz, 10 kHz, 14 kHz and 16 kHz (all of the harmonics except the harmonics around 6 kHz and 12 kHz) obtained by applying CPS-PWM are reduced by about 36.1% 38.4%, 36.1%, 34.7%, 34.1%, 29.5% respectively compared with those obtained by not applying CPS-PWM. As can been seen, the improvement achieved with CPS-PWM is sensibly reduced in the experiment result, and there is more reduction for the higher frequencies. There are mainly four reasons for this point:

- For the numerical results, the phase currents are analyzed with only the fundamental component of the back-EMF considered. For the experimental results, the phase currents are effected by the back-EMF harmonics.
- For the numerical results, the machine is modelled with constant machine parameters. For the experimental results, there is machine parameter uncertainties, for example the changes of the machine parameters with working operation due to saturations and non-linear effects.
- For the numerical results, the inverters are analyzed with linear mathematical models. For the experimental results, the inverters' non-linearity affects the experimental results.
- The numerical results are realized without the consideration of the dead time effect. The experimental results are effected by the dead time effect.

In summary, the improvement achieved with CPS-PWM is reduced in the experimental results due to the back-EMF distortion, the machine parameter uncertainties, the inverter non-linearity, the dead time effect. Therefore, further research work needs to be done with more accurate mathematical model to improve the consistency between the numerical results and the experimental results.

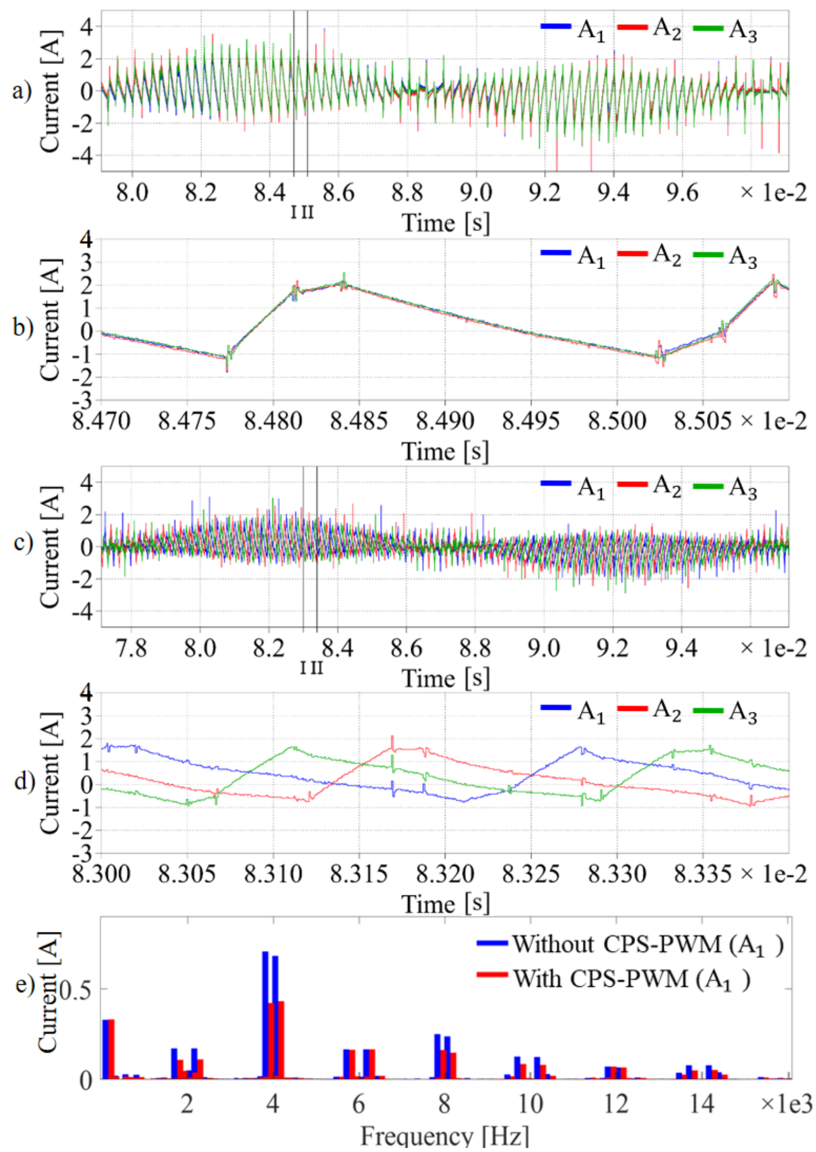

Figure 5-5: a) & b) Experimental result of current waveform of phase A1 A2 & A3 without CPS-PWM a) One period range of fundamental signal b) Two periods range of carrier signal c) & d) Experimental results of current waveform of phase A1 A2 & A3 with CPS-PWM c) One period range of fundamental signal d) Two periods range of carrier signal e) Experimental result of phase A1 current FFT spectrum without and with CPS-PWM [102].

5.4.2 Experimental results of phase currents in the distributed dual three-phase drive

The parameters used in this Section are the same with the one in Section 4.5.2. In order to validate effect on phase currents while the proposed CPS-PWM technique is applied to eliminate selective torque harmonics for dual three-phase drives, experimental results were carried out using the test rig shown in Figure 4-26. The control algorithm, operating condition and the parameters are the same as the simulations, presented in Section 5.3.2 (Section 4.4.2). The experimental test rig consists of two modular three-phase inverters, a multiphase PMSM with external connection box, and a PLECS RT box operating as a controller to output the desired PWM signals to the modular converters.

Figure 5-6 shows the phase current waveforms and their corresponding FFT spectra with and without applying CPS-PWM for the six phase machine winding in configuration $\alpha = 0$ under the modulation index M=0.8. Comparing Figure 5-6c and Figure 5-6d, the amplitudes of current harmonic components at 0.95 kHz, 1.05 kHz, 2.95 kHz and 3.05 kHz are reduced by 42%, 43%, 57% and 58% respectively employing CPS-PWM, matching with the simulation result of 55%. The current harmonic at 0.9 kHz, 1.1 kHz, 2.9 kHz and 3.1 kHz are reduced by 92%, 97%, 75% and 71% respectively applying CPS-PWM, which are larger than the simulation results. This is mainly due to interaction between the stator winding field and the higher order harmonic components of the rotor winding field, and the presence of converter nonlinear behaviors, which are neglected in the simulation models. The inductance mismatch between the simulation models and the test machine is another factor that leads to these differences.

Figure 5-7 shows that the phase current waveforms and their corresponding FFT spectra with and without CPS-PWM of winding configuration $\alpha = \frac{\pi}{6}$ under the modulation index M=0.3. Comparing Figure 5-7d and Figure 5-7f, applying CPS-PWM ($\theta_{c2} - \theta_{c1} = \frac{\pi}{2}$), the amplitudes of current harmonics at 0.95 kHz, 3.05 kHz and 4.95 kHz are increased by 22%, 31%, and 30% respectively; the amplitudes of current harmonics at 1.975 kHz, 2.025 kHz, 5.975 kHz and 6.025 kHz are increased by 630%, 655%, 649% and 623% respectively; the amplitudes of current harmonics at 1.05 kHz, 2.95 kHz, 5.05 kHz are decreased by 64%, 71% and 65% respectively. Comparing Figure 5-7e and Figure 5-7f, the CPS-PWM ($\theta_{c2} - \theta_{c1} = -\frac{\pi}{2}$) allows increasing the amplitudes of current harmonics at 1.05 kHz, 1.975 kHz, 2.025 kHz by 38%, 30% and 28% respectively; the amplitudes of current harmonics at 1.975 kHz, 2.025 kHz, 5.975 kHz and 6.025 kHz are increased by 631%, 657%, 647% and 625% respectively; the amplitudes of current harmonics at 0.95 kHz, 3.05 kHz and 4.95 kHz are decreased by 71%, 68% and 69%. Comparing Figure 5-7d, Figure 5-7f and Figure 5-7e, applying CPS-PWM ($\theta_{c2} - \theta_{c1} = \pm\frac{\pi}{2}$), the amplitudes of current harmonics reduction/increase percentage are shown in Table 5-2.

Carrier Phase Shift Angle	Frequency [kHz]			
	0.95	1.05	1.975	2.025
$\frac{\pi}{2}$	↑22%	↓64%	↑630%	↑655%
$-\frac{\pi}{2}$	↓71%	↑38%	↑631%	↑657%
	2.95	3.05	3.975	4.025
$\frac{\pi}{2}$	↓71%	↑31%	↑9%	↓24%
$-\frac{\pi}{2}$	↑30%	↓68%	↑8%	↓25%
	4.95	5.05	5.975	6.025
$\frac{\pi}{2}$	↑30%	↓65%	↑649%	↑623%
$-\frac{\pi}{2}$	↓69%	↑28%	↑647%	↑625%

Table 5-2: Amplitudes of phase current harmonic reduction/increase with CPS-PWM of winding configuration $\alpha=\frac{\pi}{6}$ (experimental results)

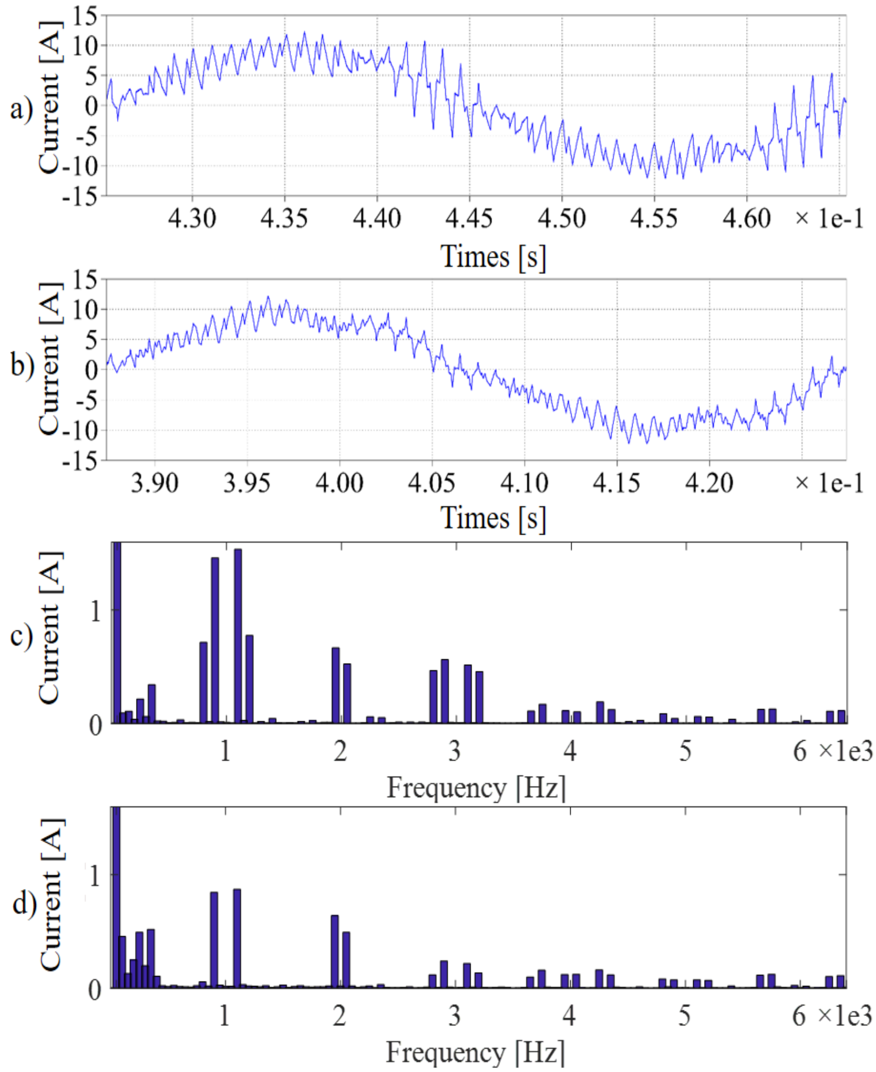

Figure 5-6: a) & b) Experimental results of phase current waveforms of winding configuration $\alpha = 0$ a) without CPS-PWM, $\theta_{c2} - \theta_{c1} = 0$ b) with CPS-PWM, $\theta_{c2} - \theta_{c1} = \pi$ c) & d) Experimental results of phase current FFT spectrums of winding configuration $\alpha = 0$ c) without CPS-PWM, $\theta_{c2} - \theta_{c1} = 0$ d) with CPS-PWM, $\theta_{c2} - \theta_{c1} = \pi$

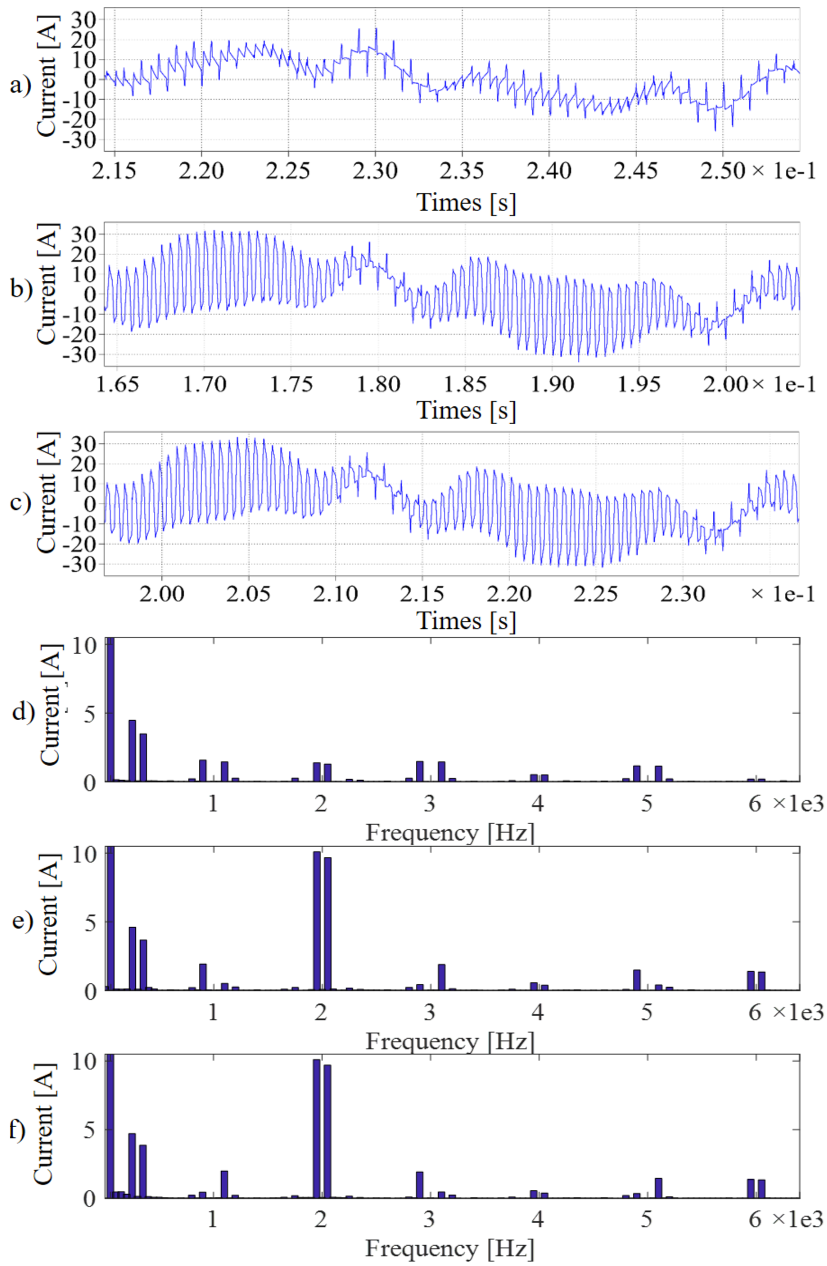

Figure 5-7: a) & b) & c) Experimental results of phase current waveforms of winding configuration $\alpha = \frac{\pi}{6}$ a) without CPS-PWM, $\theta_{c2} - \theta_{c1} = 0$ b) with CPS-PWM, $\theta_{c2} - \theta_{c1} = \frac{\pi}{2}$ c) with CPS-PWM, $\theta_{c2} - \theta_{c1} = -\frac{\pi}{2}$ d) & e) & f) Experimental results of phase current FFT spectrums of winding configuration $\alpha = \frac{\pi}{6}$ d) without CPS-PWM, $\theta_{c2} - \theta_{c1} = 0$ e) with CPS-PWM, $\theta_{c2} - \theta_{c1} = \frac{\pi}{2}$ f) with CPS-PWM, $\theta_{c2} - \theta_{c1} = -\frac{\pi}{2}$

5.5 Conclusion

This chapter analyzes the effect on phase currents applying the proposed carrier phase shift angles on multi three-phase drives with sectored and distributed machine cases. In Section 5.1, the effect on phase currents are analyzed with applying the proposed carrier phase shift angles on a sectored triple three-phase drive to eliminate the torque ripple. In Section 5.2, the phase current in the most significant cases of distributed dual three-phase drive, with $\alpha = 0$ and $= \frac{\pi}{6}$, are analyzed, while the proposed carrier phase shift angles are applied to eliminate the torque ripple.

For the case study on the sectored triple three-phase machine, while the CPS-PWM method is applied, the amplitudes of PWM related harmonic components of the phase current FFT spectrum (except the components around 6 kHz and 12 kHz) are reduced by 45.18% and about 35% in simulation results in Section 5.3.1 and experimental results in 5.3.2 respectively. Therefore, applying CPS-PWM method to the sectored three-phase drives can effectively improve the torque performance of the machine, guaranteeing major benefits in terms of torque ripple and current.

For the case study on distributed dual three-phase machine, the amplitudes of the corresponding phase current harmonic components are decreased for $\alpha = 0$ in simulation results, while the amplitudes of the corresponding current harmonic components are increased for $\alpha = \frac{\pi}{6}$ when the CPS-PWM techniques is implemented in simulation results (Section 5.3.2), which are validated in experimental results in Section 5.4.2. This is due to the different mutual coupling effect of the two three-phase winding layouts. Therefore, applying proper CPS-PWM can effectively eliminate selected torque harmonic components and improve the torque performance of distributed dual three-phase machine, and it has either negative or positive effect on phase currents due to different mutual coupling effect between the two subsystems.

Chapter 6 : Conclusions

6.1 Conclusion of the work

This work proposes a novel mathematical modelling of multi three-phase PWM drives. Numerical, FEA simulations and experimental tests have been validated the analytical mathematical models. The carrier phase shift angles obtained by the developed theory are applied on a case study of a sectored triple three-phase machine. The peak-to-peak value of the torque waveform obtained by applying CPS-PWM are reduced by 58.3% compared with the one without applying CPS-PWM in the experimental result. The PWM related harmonic components of the torque FFT spectrum obtained by applying CPS-PWM are effectively cancelled out. Selective torque harmonics elimination methods are analyzed on a case study of dual three-phase drives under the two most significant phase displacement angles with $\alpha = 0$ and $\alpha = \frac{\pi}{6}$. Both simulation and experimental results have validated the selective torque harmonics elimination method. The distortion of the phase currents can either be increased or decreased with applying the proposed CPS-PWM depending on the different mutual coupling effect between the subsystems in the multi three-phase drive.

6.2 Future work

A few points on future work are derived:

- All mathematical models of the multi three-phase drives are derived neglecting the Back-EMF distortion. More accurate analytical models can be obtained in the future work with the consideration of the Back-EMF distortion.

- The analytical models are targeted on the multi three-phase drive in this thesis. Further work can be done to establish mathematical models on multi n-phase drive (n is an arbitrary phase number) with the similar methods in this thesis.
- The look up table to find the proper carrier phase shift angles for eliminating the selective torque harmonic components in dual three-phase drive is shown in this thesis. There is potential work to give more look up tables for eliminating the selective torque harmonics in multi n-phase drives.
- The torque ripple is derived from the positive and the negative sequence harmonics of the voltage space vectors in the analytical models. The torque ripple is reduced by using the degrees of the freedom to change the carrier phase angles among different subsystems. Similarly, the common mode voltage is derived from the zero sequence harmonics of the voltage space vector. The common voltage can be potentially reduced by using the degrees of the freedom to change the carrier phase angles.
- This thesis is focused on the torque ripple reduction method by applying proper carrier phase shift angles, which means that the flexibility of the PWM control algorithm in multi three-phase is used to improve the load performance. It is also worthwhile to use the flexibility of the PWM control algorithm to improve the dc supply performance (e.g. decrease the dc capacitor voltage ripple) in the future work.

Reference

[1] J. F. Hansen and F. Wendt, “History and State of the Art in Commercial Electric Ship Propulsion, Integrated Power Systems, and Future Trends,” *Proc. IEEE*, vol. 103, no. 12, pp. 2229–2242, 2015.

[2] V. I. Patel, J. Wang, D. T. Nugraha, R. Vuletić, and J. Tousen, “Enhanced availability of drivetrain through novel multiphase permanent-magnet machine drive,” *IEEE Trans. Ind. Electron.*, vol. 63, no. 1, pp. 469–480, 2016.

[3] E. Levi, “Advances in converter control and innovative exploitation of additional degrees of freedom for multiphase machines,” *IEEE Trans. Ind. Electron.*, vol. 63, no. 1, pp. 433–448, 2016.

[4] I. Zoric, M. Jones, and E. Levi, “Arbitrary Power Sharing Among Three-Phase Winding Sets of Multiphase Machines,” *IEEE Trans. Ind. Electron.*, vol. 65, no. 2, pp. 1128–1139, 2017.

[5] D. Gerada, A. Mebarki, N. L. Brown, C. Gerada, A. Cavagnino, and A. Boglietti, “High-speed electrical machines: Technologies, trends, and developments,” *IEEE Trans. Ind. Electron.*, vol. 61, no. 6, pp. 2946–2959, 2014.

[6] K. Basu, J. S. S. Prasad, and G. Narayanan, “Minimization of torque ripple in PWM AC drives,” *IEEE Trans. Ind. Electron.*, vol. 56, no. 2, pp. 553–558, 2009.

[7] G. Valente, L. Papini, A. Formentini, and C. Gerada, “Radial Force Control of Multi-Sector Permanent Magnet Machines for Vibration Suppression,” *IEEE Trans. Ind. Electron.*, vol. 65, no. 7, pp. 5395–5405, 2018.

[8] E. Levi, R. Bojoi, F. Profumo, H. A. Toliyat, and S. Williamson, “Multiphase induction motor drives – a technology status review,” *IET Electr. Power Appl.*, vol. 1, no. 4, pp. 485–516, 2007.

[9] Y. Miyama, M. Ishizuka, H. Kometani, and K. Akatsu, “Vibration Reduction by Applying Carrier Phase-Shift PWM on Dual Three-Phase Winding Permanent-Magnet Synchronous Motor,” *IEEE Trans. Ind. Appl.*, 2018.

[10] Y. Huang, Y. Xu, W. Zhang, and J. Zou, “PWM Frequency Noise Cancellation in Two-Segment Three-Phase Motor Using Parallel Interleaved Inverters,” *IEEE Trans. Power Electron.*, vol. 34, no. 3, pp. 2515–2525, 2019.

[11] W. Zhang, Y. Xu, H. Huang, J. Zou, and S. Member, “Vibration Reduction for Dual-Branch Three-Phase Permanent Magnet Synchronous Motor with Carrier Phase-Shift Technique,” *IEEE Trans. Power Electron.*, vol. PP, no. c, p. 1, 2019.

[12] S. Rahmstorf, “Currents of Change,” no. June, 2000.

[13] S. Castellan, R. Menis, A. Tessarolo, and G. Sulligoi, “Power electronics for all-electric ships with MVDC power distribution system: An overview,” *2014 9th Int. Conf. Ecol. Veh. Renew. Energies, EVER 2014*, pp. 1–7, 2014.

[14] T. Ericsen, N. Hingorani, and Y. Khersonsky, “Power electronics and future marine electrical systems,” *IEEE Trans. Ind. Appl.*, vol. 42, no. 1, pp. 155–163, 2006.

[15] “STADT Electrically-Powered Ship Propulsion System.” [Online]. Available: http://www.nauticexpo.com/prod/stadt/product-32120-200622.html.

[16] A. K. Ådnanes, “Maritime Electrical Installations And Diesel Electric Propulsion,”

ABB, 2003.

[17] G. Carrasco and C. A. Silva, “Space vector PWM method for five-phase two-level VSI with minimum harmonic injection in the overmodulation region,” *IEEE Trans. Ind. Electron.*, vol. 60, no. 5, pp. 2042–2053, 2013.

[18] F. Barrero and M. J. Duran, “Recent advances in the design, modeling, and control of multiphase machines - Part I,” *IEEE Trans. Ind. Electron.*, vol. 63, no. 1, pp. 449–458, 2016.

[19] M. Brenna, F. Foiadelli, and D. Zaninelli, “DC Motor Drives,” in *Electrical Railway Transportation Systems*, IEEE, 2018, p. 1.

[20] A. E. Fitzgerald *et al.*, *Electric Machinery Sixth Edition MC- Graw Hill*. 2003.

[21] J. Gao, L. Zhang, and X. Wang, “AC machine systems,” *Math. Model Parameters, Anal. Syst. Performance, Tsinghua Univ. Press. Beijing*, 2009.

[22] S. D. Umans, “Total-Flux Representation of Synchronous Machines,” *IEEE J. Emerg. Sel. Top. Power Electron.*, vol. 2, no. 2, pp. 341–347, 2014.

[23] D. Bücherl, R. Nuscheler, W. Meyer, and H. G. Herzog, “Comparison of electrical machine types in hybrid drive trains: Induction machine vs. permanent magnet synchronous machine,” *Proc. 2008 Int. Conf. Electr. Mach. ICEM’08*, 2008.

[24] F. Baneira, J. Doval-Gandoy, A. G. Yepes, Ó. Ĺopez, and D. Pérez-Estévez, “Control Strategy for Multiphase Drives with Minimum Losses in the Full Torque Operation Range under Single Open-Phase Fault,” *IEEE Trans. Power Electron.*, vol. 32, no. 8, pp. 6275–6285, 2017.

[25] F. Baneira, A. G. Yepes, O. Lopez, and J. Doval-Gandoy, "Estimation Method of Stator Winding Temperature for Dual Three-Phase Machines Based on DC-Signal Injection," *IEEE Trans. Power Electron.*, vol. 31, no. 7, pp. 5141–5148, 2016.

[26] A. S. Abdel-Khalik, M. I. Masoud, and B. W. Williams, "Improved flux pattern with third harmonic injection for multiphase induction machines," *IEEE Trans. Power Electron.*, vol. 27, no. 3, pp. 1563–1578, 2012.

[27] I. Subotic, N. Bodo, and E. Levi, "Single-phase on-board integrated battery chargers for EVs based on multiphase machines," *IEEE Trans. Power Electron.*, vol. 31, no. 9, pp. 6511–6523, 2016.

[28] G. Valente, A. Formentini, L. Papini, C. Gerada, and P. Zanchetta, "Performance Improvement of Bearingless Multisector PMSM With Optimal Robust Position Control," *IEEE Trans. Power Electron.*, vol. 34, no. 4, pp. 3575–3585, 2019.

[29] J. Dai, S. W. Nam, M. Pande, and G. Esmaeili, "Medium-voltage current-source converter drives for marine propulsion system using a dual-winding synchronous machine," *IEEE Trans. Ind. Appl.*, vol. 50, no. 6, pp. 3971–3976, 2014.

[30] C. Bassi, A. Tessarolo, R. Menis, and G. Sulligoi, "Analysis of different system design solutions for a high-power ship propulsion synchronous motor drive with multiple PWM cnverters," *Int. Conf. Electr. Syst. Aircraft, Railw. Sh. Propulsion, ESARS 2010*, pp. 1–6, 2010.

[31] N. Doerry, J. Amy, and C. Krolick, "History and the Status of Electric Ship Propulsion, Integrated Power Systems, and Future Trends in the U.S. Navy," *Proc. IEEE*, vol. 103, no. 12, pp. 2243–2251, 2015.

[32] U. Javaid, D. Dujic, and W. Van Der Merwe, “MVDC marine electrical distribution: Are we ready?,” *IECON 2015 - 41st Annu. Conf. IEEE Ind. Electron. Soc.*, pp. 823–828, 2015.

[33] F. Wang, Z. Zhang, T. Ericsen, R. Raju, R. Burgos, and D. Boroyevich, “Advances in Power Conversion and Drives for Shipboard Systems,” *Proc. IEEE*, vol. 103, no. 12, pp. 2285–2311, 2015.

[34] J. W. Bennett, G. J. Atkinson, B. C. Mecrow, and D. J. Atkinson, “Fault-tolerant design considerations and control strategies for aerospace drives,” *IEEE Trans. Ind. Electron.*, vol. 59, no. 5, pp. 2049–2058, 2012.

[35] F. Barrero and M. J. Duran, “Recent Advances in the Design, Modeling, and Control of Multiphase Machines - Part II,” *IEEE Trans. Ind. Electron.*, vol. 63, no. 1, pp. 459–468, 2016.

[36] O. Lopez, J. Alvarez, J. Doval-Gandoy, and F. D. Freijedo, “Multilevel Multiphase Space Vector PWM Algorithm With Switching State Redundancy,” *IEEE Trans. Ind. Electron.*, vol. 56, no. 3, pp. 792–804, 2009.

[37] E. Levi, I. N. W. Satiawan, N. Bodo, and M. Jones, “A space-vector modulation scheme for multilevel open-end winding five-phase drives,” *IEEE Trans. Energy Convers.*, vol. 27, no. 1, pp. 1–10, 2012.

[38] S. M. Ahmed, H. Abu-Rub, and Z. Salam, “Common-mode voltage elimination in a three-to-five-phase dual matrix converter feeding a five-phase open-end drive using space-vector modulation technique,” *IEEE Trans. Ind. Electron.*, vol. 62, no. 10, pp. 6051–6063, 2015.

[39] N. Bodo, E. Levi, and M. Jones, “Investigation of carrier-based PWM techniques for a five-phase open-end winding drive topology,” *IEEE Trans. Ind. Electron.*, vol. 60, no. 5, pp. 2054–2065, 2013.

[40] D. Yazdani, S. Ali Khajehoddin, A. Bakhshai, and G. Joós, “Full Utilization of the Inverter in Split-Phase Drives by Means of a Dual Three-Phase Space Vector Classification Algorithm,” *IEEE Trans. Ind. Electron.*, vol. 56, no. 1, pp. 120–129, 2009.

[41] A. S. Abdel-Khalik, A. M. Massoud, and S. Ahmed, “Effect of DC-Link Voltage Limitation on Postfault Steady-State Performance of Asymmetrical Six-Phase Induction Machines,” *IEEE Trans. Ind. Electron.*, vol. 65, no. 9, pp. 6890–6900, 2018.

[42] P. Xu *et al.*, “Analysis of Dual Three-Phase Permanent-Magnet Synchronous Machines with Different Angle Displacements,” *IEEE Trans. Ind. Electron.*, vol. 65, no. 3, pp. 1941–1954, 2018.

[43] Y. Ren and Z. Q. Zhu, “Enhancement of steady-state performance in direct-torque-controlled dual three-phase permanent-magnet synchronous machine drives with modified switching table,” *IEEE Trans. Ind. Electron.*, vol. 62, no. 6, pp. 3338–3350, 2015.

[44] M. Barcaro, N. Bianchi, and F. Magnussen, “Faulty operations of a PM fractional-slot machine with a dual three-phase winding,” *IEEE Trans. Ind. Electron.*, vol. 58, no. 9, pp. 3825–3832, 2011.

[45] V. I. Patel, J. Wang, W. Wang, and X. Chen, “Six-phase fractional-slot-per-pole-

per-phase permanent-magnet machines with low space harmonics for electric vehicle application," *IEEE Trans. Ind. Appl.*, vol. 50, no. 4, pp. 2554–2563, 2014.

[46] M. Barcaro, N. Bianchi, and F. Magnussen, "Six-phase supply feasibility using a PM fractional-slot dual winding machine," *IEEE Trans. Ind. Appl.*, vol. 47, no. 5, pp. 2042–2050, 2011.

[47] K. Wang, Z. Q. Zhu, Y. Ren, and G. Ombach, "Torque Improvement of Dual Three-Phase Permanent-Magnet Machine with Third-Harmonic Current Injection," *IEEE Trans. Ind. Electron.*, vol. 62, no. 11, pp. 6833–6844, 2015.

[48] G. Sala, P. Girardini, M. Mengoni, L. Zarri, A. Tani, and G. Serra, "Comparison of fault tolerant control techniques for quadruple three-phase induction machines under open-circuit fault," *Proc. 2017 IEEE 11th Int. Symp. Diagnostics Electr. Mach. Power Electron. Drives, SDEMPED 2017*, vol. 2017-Janua, pp. 213–219, 2017.

[49] H. S. Che, E. Levi, M. Jones, W. P. Hew, and N. A. Rahim, "Current control methods for an asymmetrical six-phase induction motor drive," *IEEE Trans. Power Electron.*, vol. 29, no. 1, pp. 407–417, 2014.

[50] Y. Luo and C. Liu, "Elimination of Harmonic Currents Using a Reference Voltage Vector Based-Model Predictive Control for a Six-Phase PMSM Motor," *IEEE Trans. Power Electron.*, vol. 34, no. 7, pp. 6960–6972, 2019.

[51] H. S. Che, M. J. Duran, E. Levi, M. Jones, W. P. Hew, and N. A. Rahim, "Postfault operation of an asymmetrical six-phase induction machine with single and two isolated neutral points," *IEEE Trans. Power Electron.*, vol. 29, no. 10, pp. 5406–5416, 2014.

[52] W. Ding, Y. Hu, and L. Wu, “Investigation and Experimental Test of Fault-Tolerant Operation of a Mutually Coupled Dual Three-Phase SRM Drive under Faulty Conditions,” *IEEE Trans. Power Electron.*, vol. 30, no. 12, pp. 6857–6872, 2015.

[53] Z. Shen, D. Jiang, T. Zou, and R. Qu, “Dual-Segment Three-Phase PMSM with Dual Inverters for Leakage Current and Common-Mode EMI Reduction,” *IEEE Trans. Power Electron.*, vol. 34, no. 6, pp. 5606–5619, 2019.

[54] X. Han, D. Jiang, T. Zou, R. Qu, and K. Yang, “Two-Segment Three-Phase PMSM Drive with Carrier Phase-Shift PWM for Torque Ripple and Vibration Reduction,” *IEEE Trans. Power Electron.*, vol. 34, no. 1, pp. 588–599, 2018.

[55] B. Wu and M. Narimani, “High-Power Converters and AC Drives,” *High-Power Convert. AC Drives*, no. Mv, 2017.

[56] Y. Shakweh, “New breed of medium voltage converters,” *Power Eng. J.*, vol. 14, pp. 12–20, Mar. 2000.

[57] J. K. Steinke, “Use of an LC filter to achieve a motor-friendly performance of the PWM voltage source inverter,” *IEEE Trans. Energy Convers.*, vol. 14, no. 3, pp. 649–654, 1999.

[58] J. K. Steinke, R. Vuolle, H. Prenner, and J. Jarvinen, “New variable speed drive with proven motor friendly performance for medium voltage motors,” *IEEE Int. Electr. Mach. Drives Conf. IEMDC 1999 - Proc.*, pp. 235–239, 1999.

[59] D. W. Feng, Bin Wu, Samnin Wei, and D. Xu, “Space vector modulation for neutral point clamped multilevel inverter with even order harmonic elimination,” pp. 1471–

1475, 2004.

[60] T. Semis, A. B. B. Semiconductors, A. B. B. Igbt, T. Semis, and A. B. B. Semiconductors, "SEMIS – ABB Semiconductors simulation tool Two and three level VSC with IGBT."

[61] Projetos, "Product Brochure," *SportRadar*, pp. 1–18, 2014.

[62] R. Katebi, J. He, and N. Weise, "An Advanced Three-Level Active Neutral-Point-Clamped Converter with Improved Fault-Tolerant Capabilities," *IEEE Trans. Power Electron.*, vol. 33, no. 8, pp. 6897–6909, 2018.

[63] P. Management, "Your Source for Silicon Carbide."

[64] S. Lee, S. Hyun, S. Hong, H. Lee, and C. Won, "Predictive thermal modeling for loss distribution method of 3-level active NPC inverter," in *2015 IEEE International Telecommunications Energy Conference (INTELEC)*, 2015, pp. 1–5.

[65] L. Ma, K. Sun, and X. Jin, "A transformation method from conventional three phases full-bridge topology to conergy NPC topology," *2011 Int. Conf. Electr. Mach. Syst. ICEMS 2011*, pp. 1–5, 2011.

[66] B. Lee, S. Hyun, H. Lee, S. Shin, C. Won, and T. Lee, "Convenient thermal modeling for loss distribution of 3-level Active NPC using newton's law," in *2014 IEEE International Conference on Industrial Technology (ICIT)*, 2014, pp. 409–413.

[67] O. V Nos and E. E. Abramushkina, "The Control Technique for Cascaded H-Bridge Multilevel Converter with Faulty Cells," in *2018 19th International Conference of Young Specialists on Micro/Nanotechnologies and Electron Devices (EDM)*, 2018,

pp. 6403–6406.

[68] A. Ali, H. Bhattacherjee, and J. Nakka, “Improved power rating of cascaded H-Bridge multilevel inverter,” in *2015 Annual IEEE India Conference (INDICON)*, 2015, pp. 1–5.

[69] P. W. Hammond, “A new approach to enhance power quality for medium voltage AC drives,” *IEEE Trans. Ind. Appl.*, vol. 33, no. 1, pp. 202–208, 1997.

[70] R. H. Osman, “A medium-voltage drive utilizing series-cell multilevel topology for outstanding power quality,” in *Conference Record of the 1999 IEEE Industry Applications Conference. Thirty-Forth IAS Annual Meeting (Cat. No.99CH36370)*, 1999, vol. 4, pp. 2662–2669 vol.4.

[71] M. F. Escalante, J.-. Vannier, and A. Arzande, “Flying capacitor multilevel inverters and DTC motor drive applications,” *IEEE Trans. Ind. Electron.*, vol. 49, no. 4, pp. 809–815, 2002.

[72] L. Xu and V. G. Agelidis, “Flying capacitor multilevel PWM converter based UPFC,” *IEE Proc. - Electr. Power Appl.*, vol. 149, no. 4, pp. 304–310, 2002.

[73] A. Yazdani and R. Iravani, *Voltage-Sourced Converters in Power Systems*. 2010.

[74] G. Lo Calzo, P. Zanchetta, C. Gerada, A. Gaeta, and F. Crescimbini, “Converter topologies comparison for more electric aircrafts high speed Starter/Generator application,” *2015 IEEE Energy Convers. Congr. Expo. ECCE 2015*, pp. 3659–3666, 2015.

[75] G. Lo Calzo *et al.*, “Performance evaluation of converter topologies for high speed

Starter/Generator in aircraft applications," *IECON Proc. (Industrial Electron. Conf.*, pp. 1707–1712, 2014.

[76] R. Bojoi, A. Cavagnino, A. Tenconi, and S. Vaschetto, "Control of shaft-line-embedded multiphase starter/generator for aero-engine," *IEEE Trans. Ind. Electron.*, vol. 63, no. 1, pp. 641–652, 2016.

[77] A. Nabae, I. Takahashi, and H. Akagi, "A New Neutral-Point-Clamped PWM Inverter," *IEEE Trans. Ind. Appl.*, vol. IA-17, no. 5, pp. 518–523, 1981.

[78] C. Attaianese, V. Nardi, and G. Tomasso, "A novel SVM strategy for VSI dead-time-effect reduction," *IEEE Trans. Ind. Appl.*, vol. 41, no. 6, pp. 1667–1674, 2005.

[79] A. M. Trzynadlowski, R. L. Kirlin, and S. F. Legowski, "Space vector PWM technique with minimum switching losses and a variable pulse rate [for VSI]," *IEEE Trans. Ind. Electron.*, vol. 44, no. 2, pp. 173–181, 1997.

[80] O. Dordevic, M. Jones, and E. Levi, "A comparison of PWM techniques for three-level five-phase voltage source inverters," in *Proceedings of the 2011 14th European Conference on Power Electronics and Applications*, 2011, pp. 1–10.

[81] O. Dordevic, M. Jones, and E. Levi, "A Comparison of Carrier-Based and Space Vector PWM Techniques for Three-Level Five-Phase Voltage Source Inverters," *IEEE Trans. Ind. Informatics*, vol. 9, no. 2, pp. 609–619, 2013.

[82] N. Bodo, M. Jones, and E. Levi, "A space vector PWM with common-mode voltage elimination for open-end winding five-phase drives with a single DC supply," *IEEE Trans. Ind. Electron.*, vol. 61, no. 5, pp. 2197–2207, 2014.

[83] O. Dordevic, E. Levi, and M. Jones, “A Vector Space Decomposition Based Space Vector PWM Algorithm for a Three-Level Seven-Phase Voltage Source Inverter,” *IEEE Trans. Power Electron.*, vol. 28, no. 2, pp. 637–649, 2013.

[84] D. G. Holmes and T. A. Lipo, *Pulse Width Modulation for Power Converters: Principles and Practice*. Hoboken, NJ, USA: Wiley, 2003.

[85] E. Levi, D. Dujic, M. Jones, and G. Grandi, “Analytical Determination of DC-Bus Utilization Limits in Multiphase VSI Supplied AC Drives,” *IEEE Trans. Energy Convers.*, vol. 23, no. 2, pp. 433–443, 2008.

[86] H.-M. Ryu, J.-H. Kim, and S.-K. Sul, “Analysis of multiphase space vector pulse-width modulation based on multiple d-q spaces concept,” *IEEE Trans. Power Electron.*, vol. 20, no. 6, pp. 1364–1371, 2005.

[87] B. Fan, K. Wang, Z. Zheng, L. Xu, and Y. Li, “A new modulation method for a five-level hybrid-clamped inverter with reduced flying capacitor size,” *2017 IEEE Energy Convers. Congr. Expo. ECCE 2017*, vol. 2017-Janua, pp. 5262–5266, 2017.

[88] B. M. Bowes, Sid R Bird, “Novel approach to the analysis and synthesis of modulation processes in power convertors,” in *IEE Proceedings*, 1975, pp. 507–513.

[89] Z. Liu, Z. Zheng, S. D. Sudhoff, C. Gu, and Y. Li, “Reduction of Common-Mode Voltage in Multiphase Two-Level Inverters Using SPWM with Phase-Shifted Carriers,” *IEEE Trans. Power Electron.*, vol. 31, no. 9, pp. 6631–6645, 2016.

[90] H.-S. Jung, C.-E. Hwang, H.-S. Kim, S.-K. Sul, H. An, and H. Yoo, “Minimum Torque Ripple Pulse Width Modulation with Reduced Switching Frequency for

Medium Voltage Motor Drive," *IEEE Trans. Ind. Appl.*, vol. 54, no. 4, pp. 3315–3325, 2018.

[91] N. K. Bajjuri and A. K. Jain, "Torque Ripple Reduction in Double-Inverter Fed Wound Rotor Induction Machine Drives Using PWM Techniques," *IEEE Trans. Ind. Electron.*, vol. 66, no. 6, pp. 4250–4261, 2019.

[92] B. S. Umesh and K. Sivakumar, "Pole-Phase Modulated Multiphase Induction Motor Drive with Reduced Torque Ripple and Improved DC Link Utilization," *IEEE Trans. Power Electron.*, vol. 32, no. 10, pp. 7862–7869, 2017.

[93] V. S. S. P. K. Hari and G. Narayanan, "Space-vector-based hybrid PWM technique to reduce peak-to-peak torque ripple in induction motor drives," *Conf. Proc. - IEEE Appl. Power Electron. Conf. Expo. - APEC*, vol. 52, no. 2, pp. 812–817, 2014.

[94] Xibo Yuan, A. Sartain, S. Reynolds, M. Al'Akayshee, Q. Al'Akayshee, and H. Neal, "An 8 MW, 3-level inverter drive based on press-pack IGBT's: design, construction and operational propulsion system," *8th IET Int. Conf. Power Electron. Mach. Drives (PEMD 2016)*, pp. 6 .-6 ., 2016.

[95] Z. Zhang, A. M. Bazzi, and J. D. Monte, "A Novel PWM-control-based Strategy for Noise Reduction in Switched Reluctance Motors," *2018 IEEE Transp. Electrif. Conf. Expo, ITEC 2018*, pp. 550–557, 2018.

[96] A. Tanabe and K. Akatsu, "Vibration reduction method in SRM with a smoothing voltage commutation by PWM," *9th Int. Conf. Power Electron. - ECCE Asia "Green World with Power Electron. ICPE 2015-ECCE Asia*, pp. 600–604, 2015.

[97] A. Peyghambari, A. Dastfan, and A. Ahmadyfard, “Selective Voltage Noise Cancellation in Three-Phase Inverter Using Random SVPWM,” *IEEE Trans. Power Electron.*, vol. 31, no. 6, pp. 4604–4610, 2016.

[98] M. Van Der Geest, H. Polinder, and J. A. Ferreira, “Influence of PWM switching frequency on the losses in PM machines,” *Proc. - 2014 Int. Conf. Electr. Mach. ICEM 2014*, pp. 1243–1247, 2014.

[99] S. Jumayev, M. Merdzan, K. O. Boynov, J. J. H. Paulides, J. Pyrhonen, and E. A. Lomonova, “The Effect of PWM on Rotor Eddy-Current Losses in High-Speed Permanent Magnet Machines,” *IEEE Trans. Magn.*, vol. 51, no. 11, pp. 0–3, 2015.

[100] Y. Huang, Y. Xu, W. Zhang, and J. Zou, “PWM Frequency Noise Cancellation in Dual Three-Phase Motor Using Parallel Interleaved Inverters,” *IEEE Trans. Power Electron.*, vol. 8993, no. c, pp. 1–1, 2018.

[101] C. Gu, Z. Zheng, L. Xu, K. Wang, and Y. Li, “Modeling and Control of a Multiport Power Electronic Transformer (PET) for Electric Traction Applications,” *IEEE Trans. Power Electron.*, vol. 31, no. 2, pp. 915–927, 2016.

[102] X. Wang *et al.*, “Torque Ripple Reduction in Sectored Multi Three-Phase Machines Based on Carrier- Based Phase Shift PWM,” *IEEE Trans. Ind. Electron.*, 2019.

[103] A. Galassini, G. Lo Calzo, A. Formentini, C. Gerada, P. Zanchetta, and A. Costabeber, “UCube: Control platform for power electronics,” *Proc. - 2017 IEEE Work. Electr. Mach. Des. Control Diagnosis, WEMDCD 2017*, pp. 216–221, 2017.

Appendix A: MATLAB Code of matrix inductance table

```
%This is the code for inductance matrix of 2MW machine for marine
propulsion
P = 4;  %pole pair number
B = 5/6;  %beta coil pitch factor
Wk = 2;  %Turns of coil
t = pi*0.137/4;  %Pole distance=pi*R/p,R=0.137
l = 0.233;  %Stator length L=0.233
lamda = 4*pi*1e-7/0.033;  %u0/airgap_length, air_gap_length=0.033
sum_L = zeros(1,24);
sum_M = zeros(24,24);
Slot_N=[1, 7,13,19,25,31,37,43,... % A1-A8
       17,23,29,35,41,47,5 ,11,... % B1-B8
       33,39,45,3, 9, 15,21,27];% C1-C8 slot position number
sign=[+1,-1,+1,-1,+1,-1,+1,-1,+1,-1,+1,-1,+1,-1,+1,-1,+1,-1,+1,-1,+1,-
1,+1,-1];% current direction of A1-A8 B1-B8 C1-C8

   for m = 1:length(Slot_N)
       for n = 1:length(Slot_N) %24*24 Matrix table
          for N = 1:1000 % accuracy determined by user
       k_yn = sin (N*pi*B/(2*P));w = (k_yn^2)/(N^2);
       w=w*2*(1+cos(N*pi/24));% each phase eg.A1 has two coils, pi/24
is the angle shift between two coils

       alpha=(Slot_N(n)-Slot_N(m))*pi/24; %Mechanical Angle Shift (rad)
       w1 = w*cos(N.*alpha);
       sum_M(m,n) = sum_M(m,n) + w1;
       M(m,n) = (4*(Wk^2)*t*l*lamda*P/(pi^2))*sum_M(m,n);%mutual
inductance
       M(m,n) = M(m,n)*sign(m)/sign(n);% + - of mutual /current
direction/ related to Slot_N array


       sum_L(n) = sum_L(n) + w; %self inductance
       L(n) =
(4*(Wk^2)*t*l*lamda*P/(pi^2))*sum_L(n)/length(Slot_N);%self inductance
          end
      end
   end
```

Appendix B: MATLAB Code of the dual three-phase drive analytical models

```
tic
%variables setup
N=2;%number of three-phase system
Vdc=500; %DC link voltage
M=1; % modulation index
f=1000;% fundamental frequency
fc=20*f;
E=248.186;% phase peak back EMF
theta_c1=0;%radian angle of carrier in phase A
theta_c2=pi/2;
theta_01=-78.6/180*pi;%radian angle of modulating signal in phase A
theta_02=-78.6/180*pi-pi/6;
phi_v1=-pi/2;% Radian angle of back_emf in phase A
phi_v2=-pi/2-pi/6;
p=3; %pole pair number
Mspeed=2*pi*f/p;% mechaniacal speed


%effective impedance
R=11.47e-3;% phase resistance
L_end=2.185e-6;
L=28e-6; % phase inductance %Phase mutual inductance L-M
M1 =7e-6;
M2=-7e-6;
M3=0;%M1 M2 M3 system1 caused by system2
Z0=R+(L+L_end)*2*pi*f*1i;% impedance at fundamental frequency
M1_2=M1*exp(1i*(0*pi))+M2*exp(1i*(4/3*pi))+M3*exp(1i*(2/3*pi));
M2_1=M1*exp(1i*(0*pi))+M2*exp(1i*(2/3*pi))+M3*exp(1i*(4/3*pi));

%time setup
period=2;%how many periods in the plot
sample=100000*period;%sample number period  times period number
T=0:sample;
t=period/f/sample*T;%time array

%x and y
x1=2*pi*fc*t+theta_c1;
x2=2*pi*fc*t+theta_c2;
y1=2*pi*f*t+theta_01;
y2=2*pi*f*t+theta_02;

%number of m and n
number_m=10;
number_n=10;

%back-EMF Space vector
Evector_a1b1c1=E*exp(1i*(2*pi*f*t+phi_v1));% back-emf vector system1
```

```
phi_vt1=angle(Evector_a1b1c1);%time varying angle of back-emf space
vector

Evector_a2b2c2=E*exp(1i*(2*pi*f*t+phi_v2));% back-emf vector system1
phi_vt2=angle(Evector_a2b2c2);%time varying angle of back-emf space
vector

%main torque
%---------------voltagevector1
vaf1=Vdc/2*M*cos(y1);
vbf1=Vdc/2*M*cos(y1-2/3*pi);
vcf1=Vdc/2*M*cos(y1+2/3*pi);
Vfvector_a1b1c1=2/3*(vaf1+vbf1*exp(1i*(2/3*pi))+vcf1*exp(1i*(-
2/3*pi)));
phi_11=angle(Evector_a1b1c1);
%----------------voltagevector2
vaf2=Vdc/2*M*cos(y2);
vbf2=Vdc/2*M*cos(y2-2/3*pi);
vcf2=Vdc/2*M*cos(y2+2/3*pi);
Vfvector_a2b2c2=2/3*(vaf2+vbf2*exp(1i*(2/3*pi))+vcf2*exp(1i*(-
2/3*pi)));
phi_22=angle(Evector_a2b2c2);
%----------------impedance
Z1_2=M1_2*2*pi*f*1i;
Z2_1=M2_1*2*pi*f*1i;
Z_mutual=[Z0 Z1_2;Z2_1 Z0];%Z1_2 means 1 caused by 2
Z_inverse=inv(Z_mutual);

%----------------currentvector
currentf=Z_inverse*[Vfvector_a1b1c1-Evector_a1b1c1; Vfvector_a2b2c2-
Evector_a2b2c2];
Ifvector_a1b1c1=currentf(1,:);
Ifvector_a2b2c2=currentf(2,:);
If1=mean(abs(Ifvector_a1b1c1));%amplitude of fundamental current space
vector
phi_it_f1=angle(Ifvector_a1b1c1);%instantaneous angle of fundamental
current space vector
If2=mean(abs(Ifvector_a2b2c2));%amplitude of fundamental current space
vector
phi_it_f2=angle(Ifvector_a2b2c2);%instantaneous angle of fundamental
current space vector
%----------------main torque
Tmain1=3/2/Mspeed*E*If1*cos(phi_it_f1-phi_vt1);%***main torque1***
Tmain2=3/2/Mspeed*E*If2*cos(phi_it_f2-phi_vt2);%***main torque2***
Tmain=Tmain1+Tmain2;

%torque ripple
Vrvector_a1b1c1=0;
Irvector_a1b1c1=0;
Tripple1=0;

Vrvector_a2b2c2=0;
Irvector_a2b2c2=0;
Tripple2=0;

Tripple=0;
```

```
% Starting_Currents_Time=toc
for  m=1:number_m %fc
for n=-number_n:1:number_n%f
b=besselj(n,m*M*pi/2);
Amn=2*Vdc/m/pi*b*sin((m+n)*pi/2);
%--------------------------------voltagevector1
va1_rmn=Amn*cos(m*x1+n*y1);
vb1_rmn=Amn*cos(m*x1+n*(y1-2/3*pi));
vc1_rmn=Amn*cos(m*x1+n*(y1+2/3*pi));
Vmnvector_a1b1c1
=2/3*(va1_rmn+vb1_rmn*exp(1i*(2/3*pi))+vc1_rmn*exp(1i*(-2/3*pi)));
Vrvector_a1b1c1=Vrvector_a1b1c1+Vmnvector_a1b1c1;%****voltage ripple
space vector1***
%--------------------------------voltagevector2
va2_rmn=Amn*cos(m*x2+n*y2);
vb2_rmn=Amn*cos(m*x2+n*(y2-2/3*pi));
vc2_rmn=Amn*cos(m*x2+n*(y2+2/3*pi));
Vmnvector_a2b2c2
=2/3*(va2_rmn+vb2_rmn*exp(1i*(2/3*pi))+vc2_rmn*exp(1i*(-2/3*pi)));
Vrvector_a2b2c2=Vrvector_a2b2c2+Vmnvector_a2b2c2;%****voltage ripple
space vector2***
%-----------------------------------Impedance
fmn=m*fc+n*f;
if mod(n-1,3)==0
Zmn=R+(L+L_end)*2*pi*fmn*1i;%Impedance for positive sequence
Zmn1_2=M1_2*2*pi*fmn*1i;
Zmn2_1=M2_1*2*pi*fmn*1i;
Zmn_mutual=[Zmn Zmn1_2;Zmn2_1 Zmn];%Z1_2 means 1 caused by 2
Zmn_inverse=inv(Zmn_mutual);
end

if mod(n+1,3)==0
Zmn=R+(L+L_end)*2*pi*fmn*(-1)*1i; %Imepance for negative sequence
Zmn1_2=M1_2*2*pi*fmn*(-1)*1i;
Zmn2_1=M2_1*2*pi*fmn*(-1)*1i;
Zmn_mutual=[Zmn Zmn1_2;Zmn2_1 Zmn];%Z1_2 means 1 caused by 2
Zmn_inverse=inv(Zmn_mutual);
end
%-----------------------------------currentvector
currentmn=Zmn_inverse*[Vmnvector_a1b1c1; Vmnvector_a2b2c2];
Imnvector_a1b1c1=currentmn(1,:);
Imnvector_a2b2c2=currentmn(2,:);
Irvector_a1b1c1=Irvector_a1b1c1+Imnvector_a1b1c1;%***current ripple
space vector1***
Irvector_a2b2c2=Irvector_a2b2c2+Imnvector_a2b2c2;%***current ripple
space vector2***
Imn1=mean(abs(Imnvector_a1b1c1));%amplitude of current ripple space
vector
phi_it_mn1=angle(Imnvector_a1b1c1);%instantaneous angle of current
ripple space vector
Imn2=mean(abs(Imnvector_a2b2c2));%amplitude of current ripple space
vector
phi_it_mn2=angle(Imnvector_a2b2c2);%instantaneous angle of current
ripple space vector

%-----------------------------------Torque ripple
```

```
Tripple1_mn=3/2/Mspeed*E*Imn1*cos(phi_vt1-phi_it_mn1);
Tripple2_mn=3/2/Mspeed*E*Imn2*cos(phi_vt2-phi_it_mn2);
Tripple1=Tripple1+Tripple1_mn;%***torque ripple***
Tripple2=Tripple2+Tripple2_mn;%***torque ripple***
Tripple=Tripple+Tripple1_mn+Tripple2_mn;
end
end

%%%%%%%see the results%%%%%%%%%%%%%
%ripple of Va(t)
var1=0;
var2=0;
for m=1:number_m
for n=-number_n:1:number_n
b=besselj(n,m*M*pi/2);
Amn=2*Vdc/m/pi*b*sin((m+n)*pi/2);
va1_rmn=Amn*cos(m*x1+n*y1);
va2_rmn=Amn*cos(m*x2+n*y2);
var1=var1+va1_rmn;
var2=var2+va2_rmn;
end
end
%
Va1=vaf1+var1;% Phase A1 voltage
Va2=vaf2+var2;% Phase A2 voltage
Va1_no_common=real(Vrvector_a1b1c1+Vfvector_a1b1c1);%real part of
voltage space vector1
Va2_no_common=real(Vrvector_a2b2c2+Vfvector_a2b2c2);%real part of
voltage space vector2
Ia1=real(Irvector_a1b1c1+Ifvector_a1b1c1);%Phase A current / real part
of curent space vector1
Ia2=real(Irvector_a2b2c2+Ifvector_a2b2c2);%Phase A current / real part
of curent space vector2
Torque1=Tmain1+Tripple1;
Torque2=Tmain2+Tripple2;
Torque=Tmain+Tripple;%torque
```

Appendix C: MATLAB Code of the triple three-phase drive analytical models

```
%variables setup
N=3;%number of three-phase system
Vdc=60; %DC link voltage
M=0.3; % modulation index
f=50;% fundamental frequency
fc=40*f;
E=8.922;% phase peak back EMF
theta_c1=-pi/2;%radian angle of carrier in phase A
theta_c2=-pi/2+2/3*pi;
theta_c3=-pi/2-2/3*pi;
theta_0=(2.109773-0.6-0.4-0.3-0.2-0.1+0.05-0.02)/180*pi-pi/2;%radian
angle of modulating signal in phase A
phi_v=-pi/2;% Radian angle of back_emf in phase A
p=3; %pole pair number
Mspeed=2*pi*f/p;% mechaniacal speed

%effective impedance
r=0.0808;% phase resistance
L=0.31e-3; % phase inductance %Phase mutual inductance L-M
M1 =0.087e-3;
M2=0.03e-3;
M3=0.029e-3;%

%time setup
period=2;%how many periods in the plot
sample=100000*period;%sample number period  times period number
T=0:sample;
t=period/f/sample*T;%time array

%x and y
x1=2*pi*fc*t+theta_c1;
x2=2*pi*fc*t+theta_c2;
x3=2*pi*fc*t+theta_c3;
y=2*pi*f*t+theta_0;

%number of m and n
number_m=10;
number_n=10;

% voltage @fundamental
vaf=Vdc/2*M*cos(y);
vbf=Vdc/2*M*cos(y-2/3*pi);
vcf=Vdc/2*M*cos(y+2/3*pi);
vf=[vaf; vbf; vcf; vaf; vbf; vcf;vaf; vbf; vcf];
%back-EMF
ea=E*cos(2*pi*f*t+phi_v);
eb=E*cos(2*pi*f*t+phi_v-2/3*pi);
ec=E*cos(2*pi*f*t+phi_v+2/3*pi);
```

```
e=[ea;eb;ec;ea;eb;ec;ea;eb;ec];

%impendance
MM= 1e-3*[0.31  -0.087  -0.087  -0.029  0.029   0.029   -0.029  0.029
0.029;
-0.087  0.31    0.03    0.029   -0.029  -0.029  0.029   -0.029  -0.029;
-0.087  0.03    0.31    0.029   -0.029  -0.029  0.029   -0.029  -0.029
-0.029  0.029   0.029   0.31    -0.087  -0.087  -0.029  0.029   0.029;
0.029   -0.029  -0.029  -0.087  0.31    0.03    0.029   -0.029  -0.029;
0.029   -0.029  -0.029  -0.087  0.03    0.31    0.029   -0.029  -0.029;
-0.029  0.029   0.029   -0.029  0.029   0.029   0.31    -0.087  -0.087;
0.029   -0.029  -0.029  0.029   -0.029  -0.029  -0.087  0.31    0.03;
0.029   -0.029  -0.029  0.029   -0.029  -0.029  -0.087  0.03    0.31];

R=[r 0 0 0 0 0 0 0 0;
   0 r 0 0 0 0 0 0 0;
   0 0 r 0 0 0 0 0 0;
   0 0 0 r 0 0 0 0 0;
   0 0 0 0 r 0 0 0 0;
   0 0 0 0 0 r 0 0 0;
   0 0 0 0 0 0 r 0 0;
   0 0 0 0 0 0 0 r 0;
   0 0 0 0 0 0 0 0 r];

% current @fundamental
Z=MM*2*pi*f*1i+R;
Z_inverse=inv(Z);
If=Z_inverse*[vf-e];

%current @ ripple
var1=0;
var2=0;
var3=0;
Ir=0;
vr=0;
for m=1:number_m
for n=-number_n:1:number_n
b=besselj(n,m*M*pi/2);
Amn=2*Vdc/m/pi*b*sin((m+n)*pi/2);

%Va_r
va1_rmn=Amn*cos(m*x1+n*y);
va2_rmn=Amn*cos(m*x2+n*y);
va3_rmn=Amn*cos(m*x3+n*y);
var1=var1+va1_rmn;
var2=var2+va2_rmn;
var3=var3+va3_rmn;

%Vb_r
vb1_rmn=Amn*cos(m*x1+n*(y-2/3*pi));
vb2_rmn=Amn*cos(m*x2+n*(y-2/3*pi));
vb3_rmn=Amn*cos(m*x3+n*(y-2/3*pi));


%Vc_r
```

```
vc1_rmn=Amn*cos(m*x1+n*(y+2/3*pi));
vc2_rmn=Amn*cos(m*x2+n*(y+2/3*pi));
vc3_rmn=Amn*cos(m*x3+n*(y+2/3*pi));

vrmn=[va1_rmn;vb1_rmn;vc1_rmn;va2_rmn;vb2_rmn;vc2_rmn;va3_rmn;vb3_rmn;v
c3_rmn];
%-----------Impedance
fmn=m*fc+n*f;
if mod(n-1,3)==0
Zmn=MM*2*pi*fmn*1i+R;
Zmn_inverse=inv(Zmn);
Irmn=Zmn_inverse*vrmn;
end

if mod(n+1,3)==0
Zmn=MM*2*pi*fmn*(-1)*1i+R;
Zmn_inverse=inv(Zmn);
Irmn=Zmn_inverse*vrmn;
end

if mod(n,3)==0
Irmn=0;
end

vr=vr+vrmn;
Ir=Ir+Irmn;
end
end
%%%current
I=If+Ir;

Ia1n=I(1,:);
Ib1n=I(2,:);
Ic1n=I(3,:);
I1=2/3*(Ia1n+Ib1n*exp(1i*(2/3*pi))+Ic1n*exp(1i*(-2/3*pi)));%I don't
understand
Ia1=real(I1);

Ia2n=I(4,:);
Ib2n=I(5,:);
Ic2n=I(6,:);
I2=2/3*(Ia2n+Ib2n*exp(1i*(2/3*pi))+Ic2n*exp(1i*(-2/3*pi)));
%Ia2=real(I2);

Ia3n=I(7,:);
Ib3n=I(8,:);
Ic3n=I(9,:);
I3=2/3*(Ia3n+Ib3n*exp(1i*(2/3*pi))+Ic3n*exp(1i*(-2/3*pi)));
%Ia3=real(I3);

II=real(I1+I2+I3);

%%%torque
Evector_a1b1c1=E*exp(1i*(2*pi*f*t+phi_v));% back-emf vector system1
phi_vt=angle(Evector_a1b1c1);
```

```
II1=abs(I1);
phi1=angle(I1);

II2=abs(I2);
phi2=angle(I2);

II3=abs(I3);
phi3=angle(I3);

T=3/2/Mspeed*E*(II1.*cos(phi_vt-phi1)+II2.*cos(phi_vt-
phi2)+II3.*cos(phi_vt-phi3));
```

Appendix D: PLECS model of the triple three-phase drive

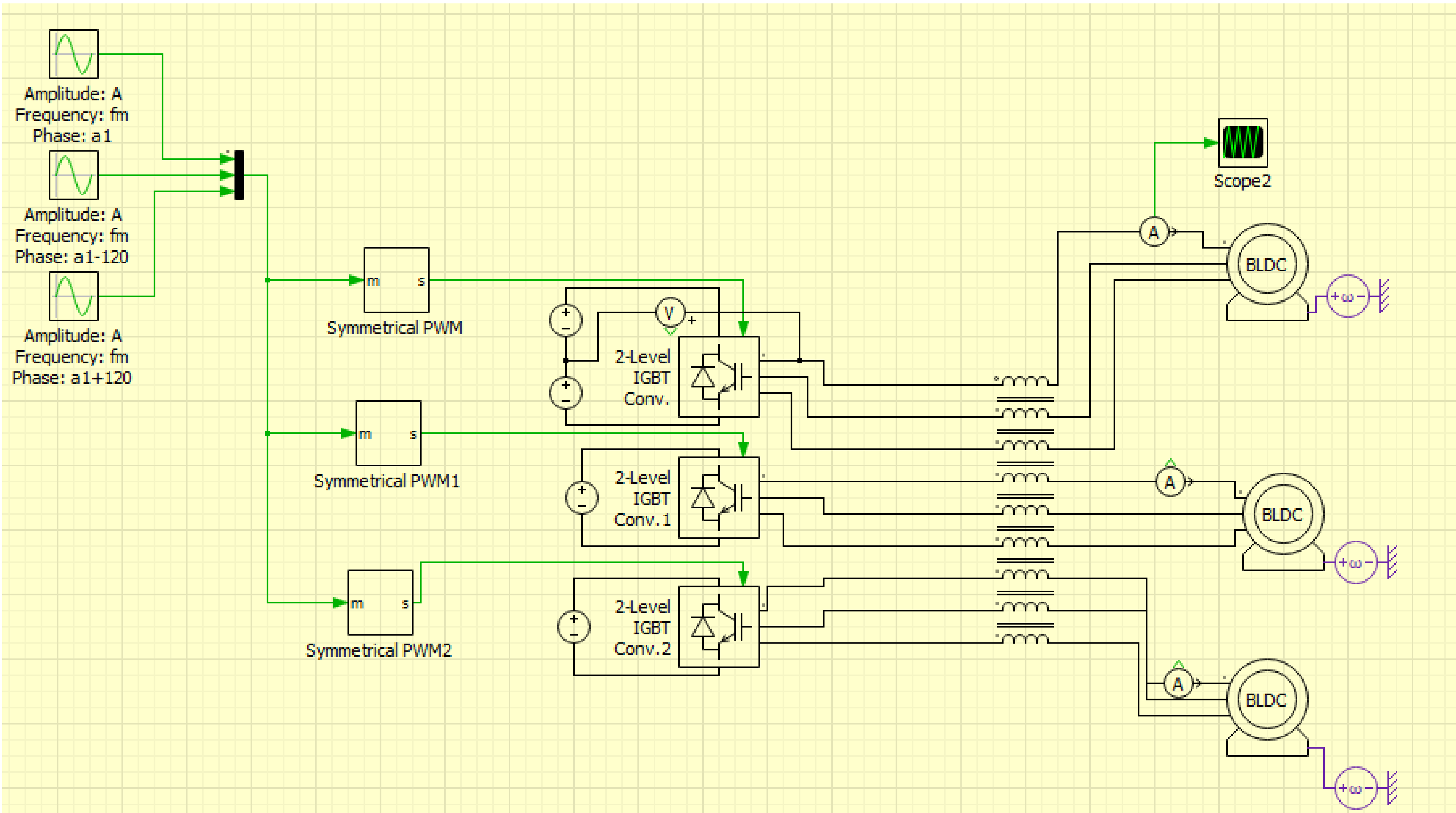

Appendix E: Winding layout of a 48-slot 8-pole distributed PM machine

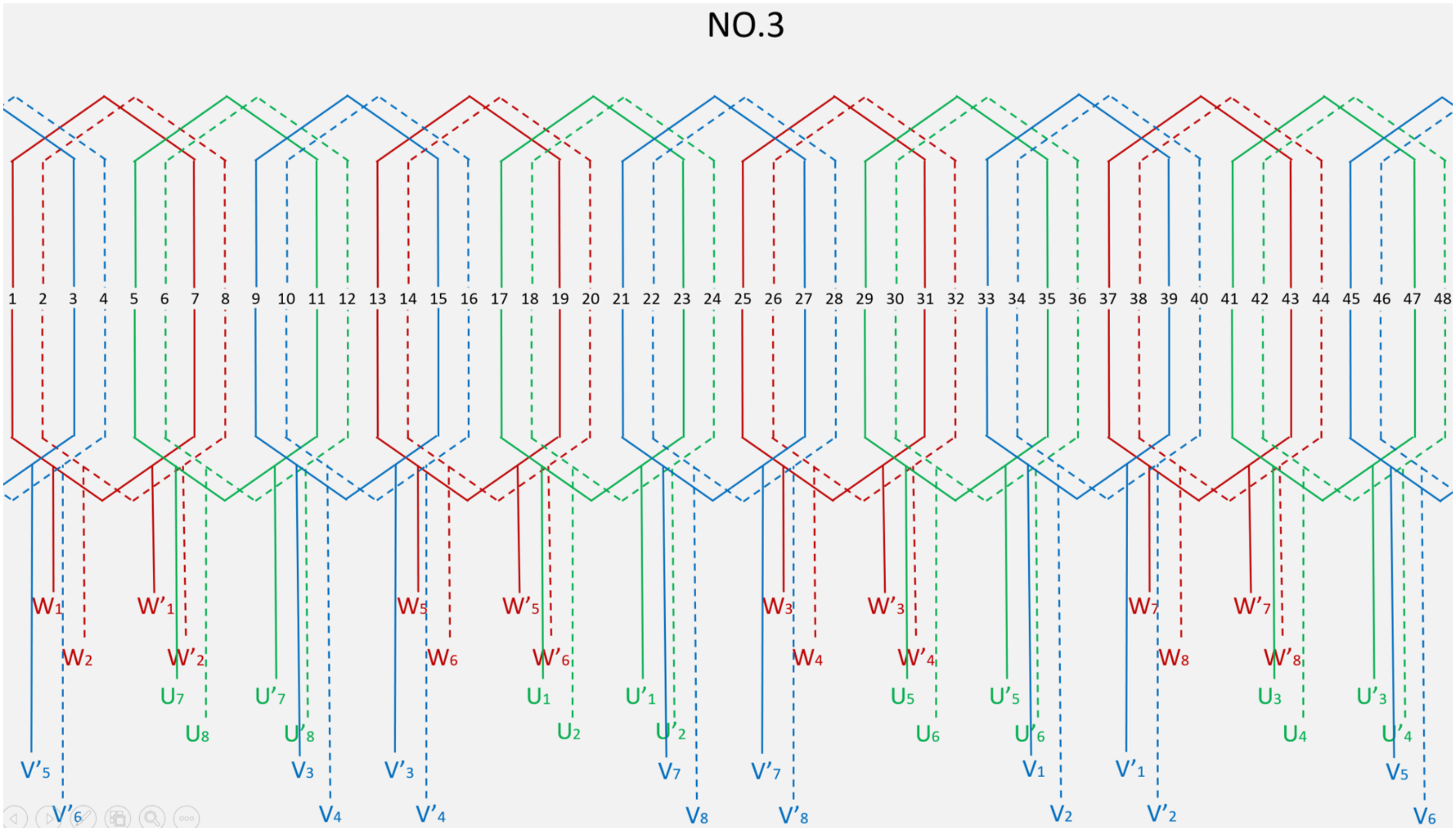

Appendix F: List of Publications

Wang *et al.*, “Torque Ripple Reduction in Sectored Multi Three-Phase Machines Based on Carrier- Based Phase Shift PWM,” *IEEE Trans. Ind. Electron.*, 2019. doi: 10.1109/TIE.2019.2931239

Wang *et al.*, “Selective Torque Harmonic Elimination on Dual Three-phase PMSM Machines Based on PWM Carrier Phase Shift,” *IEEE Trans. Power Electron.* (Submitted)

X. Wang, C. Gu, G. Buticchi, H. Zhang, and C. Gerada, “A Novel Modelling Approach of Modular Multi Three-phase Drive System for High Performance Applications,” *2019 Internatianl Conference on Electrical Machines and Systems* (*ICEMS)* (Accepted)